Photonic crystals: Analysis, design and biochemical sensing applications

A Thesis
Presented to
The Academic Faculty

by

Hamza Kurt

In Partial Fulfillment
of the Requirements for the Degree
Doctor of Philosophy in the
School of Electrical and Computer Engineering

Georgia Institute of Technology
August 2006

Photonic crystals: Analysis, design and biochemical sensing applications

Approved by:

Dr. Ali Adibi, Committee Chair
School of ECE
Georgia Institute of Technology

Dr. Paul Voss
School of ECE
Georgia Institute of Technology

Dr. David S. Citrin, Advisor
School of ECE
Georgia Institute of Technology

Dr. Christopher Summers
School of MSE
Georgia Institute of Technology

Dr. John Papapolymerou
School of ECE
Georgia Institute of Technology

Date Approved: June 22, 2006

This dissertation is dedicated to

my mother Seniye

and

my father Ali

ACKNOWLEDGEMENTS

The end of one journey means the beginning of another one. After two-year of study at the University of Southern California while exploring the west side of the US, I started my PhD program on the east side at Georgia Institute of Technology in 2002. During the last year of my study, I had a chance to move to the Georgia Tech Lorraine, France. Throughout all these years, I was lucky meeting with precious people; friends, instructors and advisors.

It is impossible to mention all of the people whom I would like to thank but first I want to express my sincere gratitude towards my advisor, Prof. David S. Citrin, for making my study at Georgia Tech stimulating and enjoyable one while giving me the full freedom to explore this research topic.

I would like to thank to my dissertation committee members Prof. Ali Adibi and Prof. John Papapolymerou for taking the time to read and comment on both my proposal and dissertation and Prof. Christopher Summers for willing to serve in my committee.

I gratefully acknowledge the financial support of the Turkish Education Foundation (TEV) for my master study at the University of Southern California.

I would like to thank all my friends in Atlanta, California, and everywhere for the joy they brought in my life.

My big gratitude goes to every member of my family for everything especially believing in me, for their never ending love, encourages and patience. Last but not least, I am grateful to my fiancée, Özlem, for her love and support.

TABLE OF CONTENTS

ACKNOWLEDGEMENTS ..... **iv**

LIST OF TABLES ..... **vii**

LIST OF FIGURES ..... **viii**

SUMMARY ..... **xi**

CHAPTER I

INTRODUCTION **1**

1.1 Photonic crystals: Past, present and future 1
1.2 Outline of the thesis 16

CHAPTER II

THE STUDY OF PHOTONIC CRYSTALS **17**

2.1 Introduction to the numerical methods 17

2.2 The plane wave expansion method 18
2.2.1 The theory of band structures 18
2.2.2 The formulation of PWM 20
2.2.3 Two-dimensional PWM 22
2.2.4 Two-dimensional photonic crystals 24
2.2.5 Three-dimensional photonic crystals 25
2.2.6 Photonic crystal parameters 30

2.3 Finite-difference time-domain method 32
2.3.1 The formulation of FDTD 32
2.3.2 One-dimensional FDTD method 33
2.3.3 Two-dimensional FDTD method 36
2.3.4 There-dimensonal FDTD method 39

2.4 Boundary conditions 43
2.4.1 Perfectly matched layer 43
2.4.2 PML loss parameters 44
2.4.3 Periodic boundary conditon 45

2.5 Finite-difference time-domain with recursive convolution 47

CHAPTER III

PHOTONIC CRYSTALS FOR BIOCHEMICAL SENSING (I) 55

3.1 Introduction 55
3.2 Photonic crystal waveguide sensors 57
3.3 Results and discussions 61
3.4 Photonic crystal waveguide sensors in the microwave regime 67
3.5 Conclusions 69

CHAPTER IV

PHOTONIC CRYSTALS FOR BIOCHEMICAL SENSING (II)..... 72

4.1 Introduction 72
4.2 Coupled-resonator optical waveguide sensors 73
4.3 Results and discussions 74
4.4 Conclusions 82

CHAPTER V

ANNULAR PHOTONIC CRYSTALS 85

5.1 Introduction 85
5.2 The structure 87
5.3 Results and discussions 88
5.4 Conclusions 105

CHAPTER VI

PHOTONIC-CRYSTAL HETEROSTRUCTURES 106

6.1 Introduction 106
6.2 Design of photonic crystal heterostructure waveguides 108
6.3 Calculation of bending efficiency 116
6.4 Results and discussions of 30^0 PCW bend 119
6.5 Conclusions 126

CHAPTER VII

CONCLUSIONS AND FUTURE RESEARCH..... 128

REFERENCES..... 134

LIST OF TABLES

Table 4.1: Design parameters of CROW. 78

Table 5.1: Comparison of square lattice PC and APC. 97

Table 5.2: Comparison of triangular lattice PC and APC. 97

LIST OF FIGURES

Figure 1.1: Energy plot of an electron. 3

Figure 1.2: One dimensional periodic layers. 4

Figure 1.3: Band diagram of 1D periodic layer. 6

Figure 1.4: Schematics of photonic crystals. 7

Figure 1.5: Defect modes of a photonic crystal. 11

Figure 1.6: 90^0 waveguide band. 12

Figure 1.7: T-junction and splitter. 13

Figure 2.1: Schematics of 2D photonic crystals. 24

Figure 2.2: Band daigram of 2D square lattice photonic crystal. 26

Figure 2.3: Band digram of 2D triangular lattice photonic crystal. 27

Figure 2.4: Lattice structure of 3D photonic crystals. 28

Figure 2.5: Band diagram of 3D photonic crystals 29

Figure 2.6: Photonic band gap variations. 31

Figure 2.7: Saptial meshes and time steps for 1D FDTD. 35

Figure 2.8: Mesh arrangements of 2D FDTD for TE polarization 38

Figure 2.9: Mesh arrangements of 2D FDTD for TM polarization. 38

Figure 2.10: Mesh arrangements of 3D FDTD. 42

Figure 2.11: PML boundary condition..... 46

Figure 2.12: Point dipole source. 46

Figure 2.13: Reflection and transmision coefficient for dispersive medium..... 53

Figure 2.14: Plot of absorption coefficent 54

Figure 3.1: Electromagnetic spectrum. 57

Figure 3.2: Schematic drawing of photonic crystal sensor. 59

Figure 3.3: Dispersion diagram of photonic crystal for TE modes..... 60

Figure 3.4: Transmission spectrum of PCW sensor..... 63

Figure 3.5: Steady-state variations of field propagation. 65

Figure 3.6: The enhancement parameter..... 67

Figure 3.7: Fabricated PC and PCW. 68

Figure 3.8: Experimental setup. 68

Figure 3.9: The transmission spectra (experimental)..... 70

Figure 3.10: The transmission spectra (numerical)..... 71

Figure 4.1: Schematic diagrams of CROW structure. 76

Figure 4.2: Steady-state field variation for CROW. 80

Figure 4.3: The enhancement factor for the CROW. 82

Figure 4.4: Resonant frequency shift of CROW. 83

Figure 5.1: Band gap map of square and triangular lattice PC. 91

Figure 5.2: Schematics of APC. 92

Figure 5.3: Complete PBG variations of APC. 93

Figure 5.4: Dispersion diagram of triangular lattice APC 94

Figure 5.5: Dispersion diagram of square lattice APC 94

Figure 5.6: Electric field of TM modes 96

Figure 5.7: APC unit cells..... 101

Figure 5.8: Dispersion diagrams of APCs in Fig. 5.7 102

Figure 5.9: PBG to midgap ratio. 103

Figure 6.1: Schematic of PC heterostructure waveguide unit cell. 110

Figure 6.2: Usual triangular lattice PC and deformed one 111

Figure 6.3: Dispersion diagram 112

Figure 6.4: Band gap map 114

Figure 6.5: PC heterostructure waveguide bend 115

Figure 6.6: Schematics of PC hetero strucuture waveguide bend 118

Figure 6.7: Steady-state field profile 120

Figure 6.8: Narrow band pulse propagation 121

Figure 6.9: Field amplitudes in time. 122

Figure 6.10: The bending efficiency 124

Figure 6.11: The steady-state field variation of 30^0 double bends. 125

Figure 6.12: PC hetero structure 90^0 bend 125

SUMMARY

The absence of appropriate media to cultivate photons efficiently at the micro or nano scale has hindered taking the full advantage of processing information with light. The proposal of such a medium for light, known as photonic crystals (PCs)--multi-dimensional artificially periodic dielectric media--brings the possibility of a revolution in communications and sensing much closer. In such media, one can manipulate light at a scale on the order of the wavelength or even shorter.

Applications of PCs other than in communication include bio-sensing because of the peculiar properties of PCs such as the capability of enhance field-matter interaction and control over the group velocity. As a result, PC waveguide (PCW) structures are of interest and it is expected that PC sensors offer the feasibility of multi-analyte and compact sensing schemes as well as the ability of the detection of small absolute analyte quantities (nanoliters) and low-concentration samples (picomoles), which may be advantages over conventional approaches such as fiber optic and slab waveguide sensors. Depending on the nature of the analyte, either dispersive (index sensor) or absorptive (absorption sensor) sensing schemes may be implemented.

Light propagation is controlled fully only with 3D PCs. One of the problems arising due to reducing the dimension to 2D is that PCs become strongly polarization sensitive. In many cases, one wants to implement polarization insensitive devices such that the PC provides a full band gap for all polarizations. To address this problem, a novel type of PC called annular PC (APC) is proposed and analyzed. The capability of tuning the TE and TM polarizations independently within the same structure provides great

flexibility to produce polarization-independent or polarization-dependent devices as desired.

PCW bends are expected to be the essential building blocks of photonic integrated circuits. Sharp corners having small radii of curvature can be obtained. To enhance the low-loss and narrow-band transmission through these bends, PC heterostructures waveguide concept is introduced. We show that in PCWs formed by joining different types of PCs in a single structure, light can flow around extremely sharp bends in ways that are not possible using conventional PCWs based on a single type of PC.

CHAPTER I

INTRODUCTION

1.1 Photonic crystals: Past, present and future

The engineering of electromagnetic (EM) modes at optical frequencies in multidimensional artificially periodic structures was first proposed by Yablonovitch and by John in 1987 [1, 2]. Yablonovitch's initial goal was to study the modification of spontaneous-emission rates—a major loss mechanism degrading the efficiency of semiconductor lasers, heterojunction bipolar transistors, and solar cells. Inspired by the one-dimensional periodic dielectric layer that gives rise to band gap for EM waves propagating perpendicular to the patterned layers, increasing the periodicity to three dimensions may provide band gap in omni-direction. The density of states (DOS) is zero within the band gap because the wave vector k is evanescent. Since the spontaneous-emission rates are proportional to the DOS, it may be possible to inhibit the spontaneous emission. Meanwhile, John argued that the localization of photons can be achieved with three-dimensional superlattices having certain disorder. As proven later both theoretically and experimentally, these periodic structures, called photonic crystals (PC), have the ability to control and manipulate the flow of light. The term *photonic* was selected because the initial aim was to study the interaction of photon with the periodic medium. Later, different but similar names have been adapted such as electromagnetic band-gap materials for the microwave region and phononic band gap structures for the acoustic waves.

A uniform, lossless and dispersion-free bulk medium slows down the speed of light proportional to the refractive index n and the band diagram is continuous. The EM wave propagation through a PC is modified and this modification can be explained using an analogy of electron motion in the crystalline solids [3, 4]. An atomic lattice creates a periodic potential to an electron propagating through a semiconductor crystal; hence, the electron propagation is modulated by the crystalline structure of the atomic lattice as shown on Fig. 1.1. The gap between the conduction and the valance bands defines forbidden states for propagating electrons and is called electronic band gap (energy gap). Similarly, the lattice of dielectric media is analogous to a potential for the EM wave. In the dispersion diagram [$\omega(k)$ vs. k], there are frequency bands in which the EM waves are allowed to propagate freely through the structure; however, for some ranges of frequencies there may be no propagating modes, and such frequency ranges are called photonic band gap (PBG). Since the wave vector there is imaginary, it decays exponentially if the frequency lies within the PBG. The physical origin of the PBG can be explained as follows. For simplicity we can assume 1D periodic lattice situation stacked of high- and low-dielectric layers n_H and n_L, alternately. The electric field is in the form of plane wave $\exp(jk \cdot r)$ modulated by the periodic function of the lattice $\varepsilon(x) = \varepsilon(x + a)$. The Bragg condition is satisfied at the edge of Brillouin zone, $k = \pm \pi / a$ for this structure. The right and left traveling waves create a standing wave of the form $\sin(\pi x / a)$ and $\cos(\pi x / a)$ as shown in Fig. 1.2. The energy is proportional to the magnitude square of the electric field.

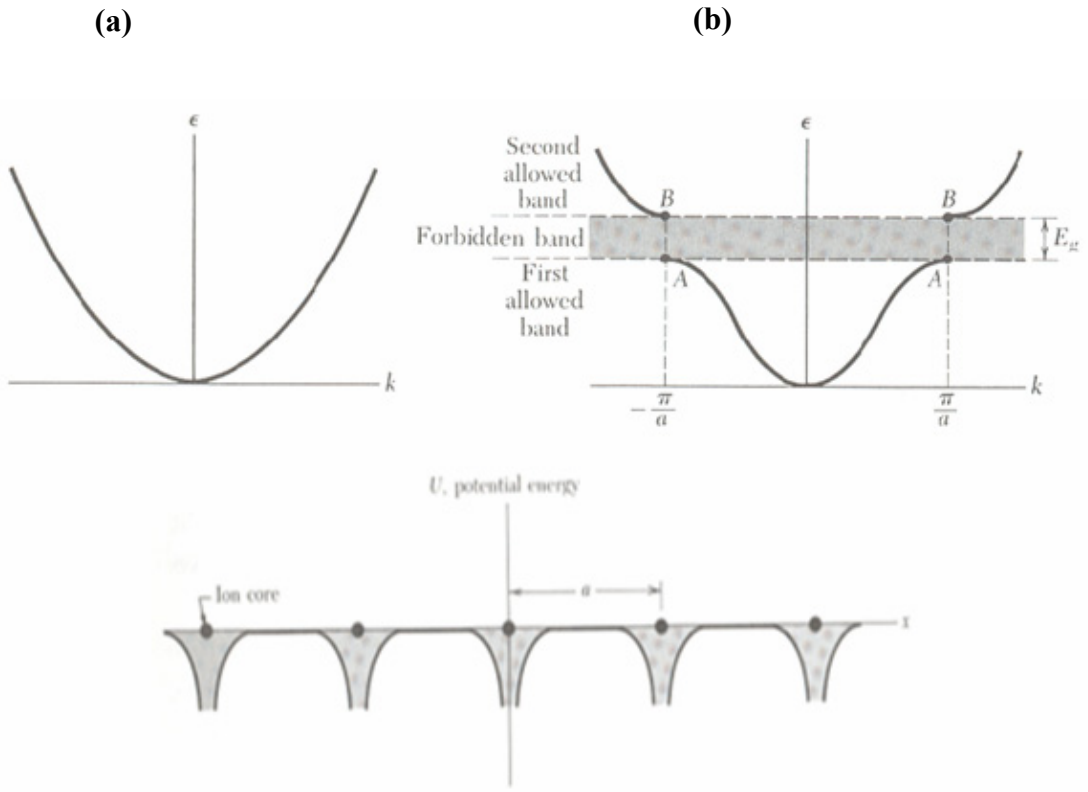

Figure 1.1: Energy diagrams (a) for a free electron, and (b) for an electron propagating through an atomic lattice [4].

The low order mode $(n=1)$ tends to confine its energy in the high dielectric region while lowering the frequency. At the same time, high order mode $(n=2)$ tends to confine its energy in the high dielectric region while increasing its frequency. The difference of energy confinement in the low and high refractive index causes the energy gap (band gap) as shown in Fig. 1.3. Inside the band gap k is imaginary so the field is exponentially decaying and outside of the band gap k is real and field is propagating. The Bragg condition is a transition state where the field is a standing wave [5].

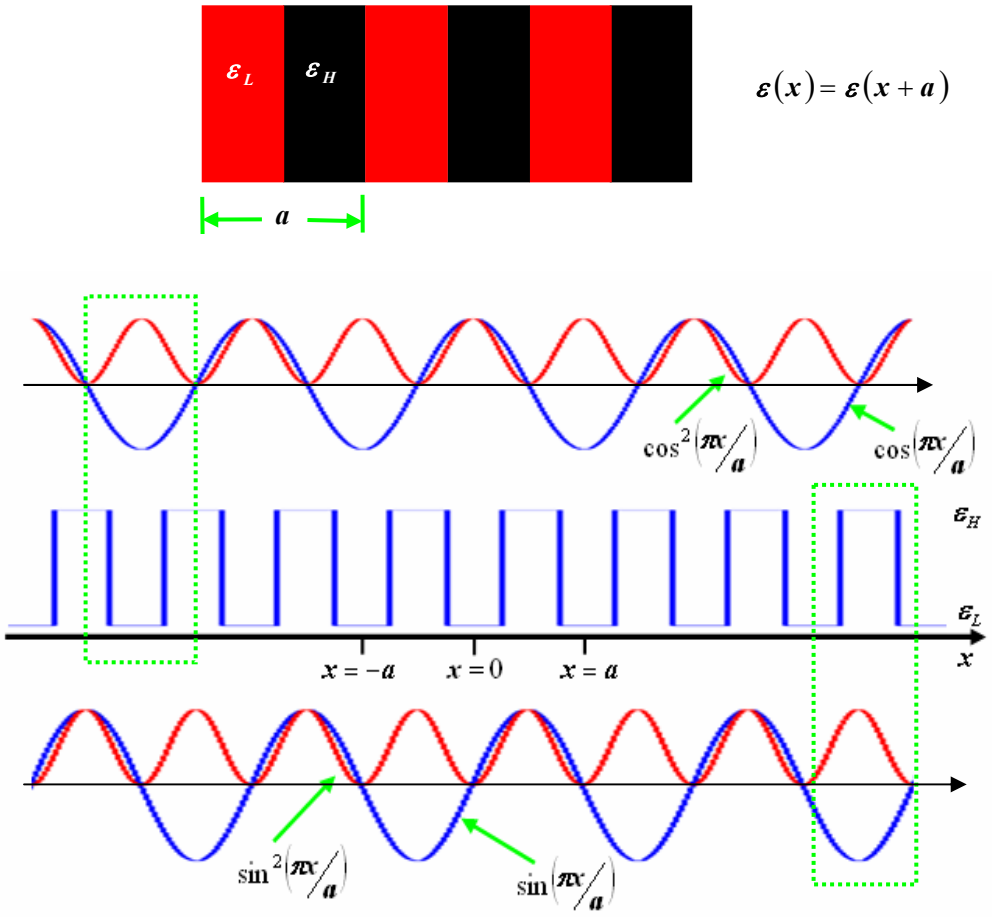

Figure 1.2: One-dimensional periodic layers. Electric field forms and energy profiles for the modes $n = 1$ and $n = 2$ are shown.

The one-dimensional counterpart of PCs was first studied by Lord Rayleigh in 1887. It was shown that light propagation is angle dependent and prohibited for a range of frequencies. Many optoelectronic devices employ 1D PC as a frequency selective or highly reflective material. A stack of dielectric layers with thicknesses of $\lambda/4$ forms a highly reflective multilayer film which is also known as distributed Bragg reflector (DBR). The distributed feedback lasers (DFB), and vertical cavity surface emitting lasers (VCSELs) employ 1D PCs. In fact, a VCSEL structure can be assumed as a 1D PC with an introduction of spatial defect in the middle section. Even though the wide deployment of 1D PCs or DBRs, two- and three-dimensional PCs were proposed 100 years later.

The idea of increasing the periodicity to more than one dimension, as shown in Fig. 1.4 may seem straightforward, but the inherent difficulty at the beginning of research in this area was that it was not known yet what type of structures provide full band gaps even though it was relatively easy to have pseudo-gaps (partial-gaps). Thus, it took three years to find correct geometries by trial and error. Later, computational methods played a large role in calculating the band diagrams and predicting if a given type of crystal has band gaps or not.

The driving force behind the PCs is the yields one may get because of the superior manipulation of light propagation. The obvious advantages of processing information with photonic devices are as follows. The bandwidth advantage of photonics over electronic circuits is tremendous, thus enabling data rates far in excess of what has been achieved with microelectronics. Moreover, while photons interact weakly (no charge), electrons interact strongly. Each electron produces heat, photons, on the other hand, hardly generate any heat in transparent media.

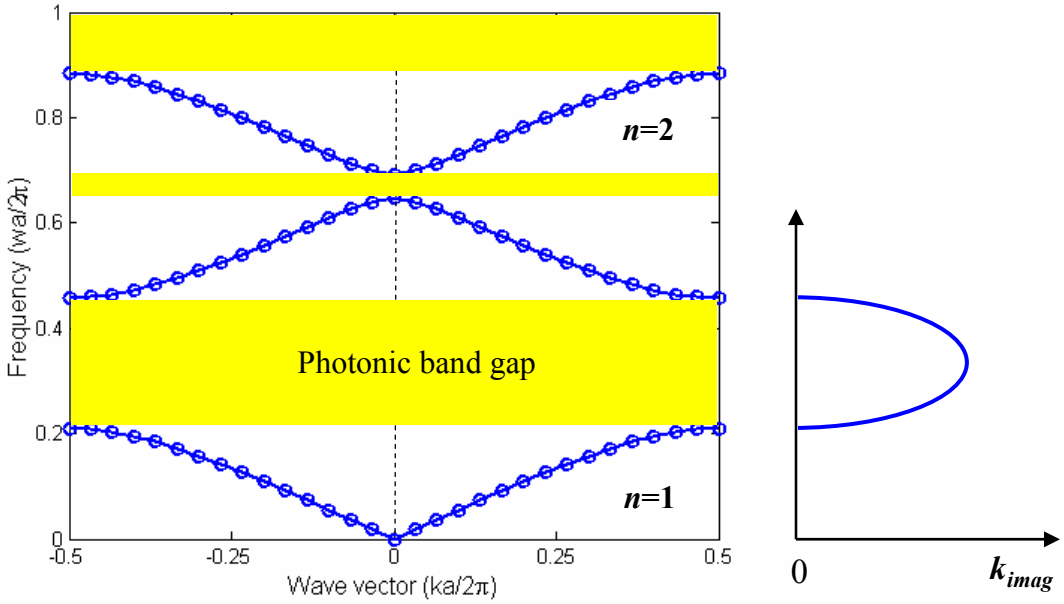

Figure 1.3: Band diagram of 1D multilayer film with lattice constant a . High dielectric $(\varepsilon = 12)$ width is $0.2a$ and low dielectric is air. The imaginary part of the wavevector is depicted around the band gap.

The electronic world, due to the impact of semiconductor materials and the mature processing and fabrication technologies that have grown up around them, has progressed tremendously compared to the photonic world. The absence of an appropriate medium to cultivate photons efficiently at the micro or nanoscale has hindered the achievements of a similar revolution in photonics compared with that which has occurred in microelectronics. The proposal of such a medium for light, known as photonic crystals (PCs) may bring the possibility of a similar revolution in many areas including communications and sensing much closer.

What makes PCs special is the appearance of PBGs and the possibility to intentionally create defects. Similar to impurity levels obtained by doping in semiconductor materials, breaking the translational symmetry in PCs may give rise to EM defect states. The periodic arrangement of the dielectric materials may provide an

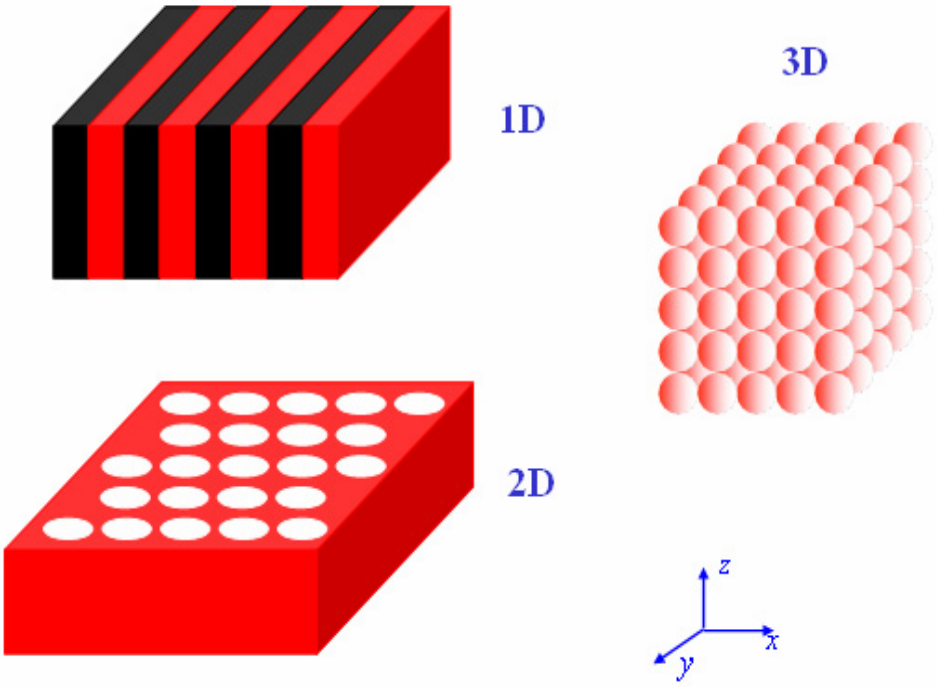

Figure 1.4: Schematic representations of one-, two- and three-dimensional photonic crystals.

effective potential for photons, i.e., photons acquire an effective mass. Constructive interference of reflected light from the dielectric material prohibits propagation when the Bragg condition is satisfied. In the dispersion diagram, there are two types of regions, called stop bands and pass bands. If the index contrast of non-absorbing dielectric materials is large enough and if scattering from a periodic structure interferes

constructively, then there are no allowed propagating modes irrespective of the propagation direction within some frequency range called the stop band or PBG. On the other hand, destructive interference will allow the light to propagate freely through the periodic material for a band of frequencies; this is called the pass band. The low-frequency and high-frequency band edge of PBG are frequently called the dielectric and air bands, analogous to the valance and conduction bands in solids. Because of the scalability of the Maxwell equations, one can design PCs operating in the optical regime with micron sizes or in the microwave region with millimeter sizes, depending on the goal. This can be inferred from the Bragg condition [$\lambda = 2a\sin(\theta)$ where a is the lattice periodicity and θ is the incidence angle]. Exploiting these features resulted in numerous proposals and studies of linear and nonlinear applications of PCs.

The first successful PC was made in 1991 [6]. The diamond-like structure obtained by drilling holes in a bulk dielectric material exhibited PBG from 13 to 16 GHz. In addition, face centered cubic (fcc) [7], woodpile [8], and self-organized structures [9] such as artificial opals and colloidal systems have been suggested and shown to produce complete PBGs. The drawback of self assembly is the dearth of high index-contrast materials required to obtain PBG's, and the means to incorporate controlled defects (point/line) in the structure is difficult. Photonic crystals face two different dilemmas toward the opposite sides of EM spectrum. In the low-frequency regime they are large (bulky) though easy to manufacture. On the other hand, the periodicity of the structure is of the order of micrometers in the high-frequency regions making their fabrication a challenging task. The most appealing prospect of the idea of PBG was in the field of optics. Even though complete control of light can be achieved in all directions for any

polarization with three-dimensional PCs, because of the fabrication difficulties of sub-micron dimensions of the structures in the optical domain, more attention has been given to two-dimensional planar PCs which are periodic in two dimensions and uniform in the third dimension.

Numerical methods to analyze and design these structures are employed because of the difficulty in analytical approaches. Therefore, various computational EM methods have been used for this purpose, including the planewave method (PWM) [10, 11], the transfer-matrix method (TMM) [12], the FDTD [13, 14] method, the Korringa-Kohn-Rostoker method (multiple-scattering theory), and tight-binding formulation [15-17]. To calculate the band structure of PCs using PWM, one has to formulate an eigenvalue problem to solve for the eigenfrequencies. The analysis is carried out for all wavevectors within the irreducible Brillouin zone

The transfer-matrix method is a layer-by-layer approach and consists of writing the Maxwell equations in *k*-space on a mesh. In FDTD, a unit cell is truncated by Bloch boundary conditions and an initial field excitation (that can be random or due to the dipole sources located in non-symmetric places within the computational domain) is propagated in time and space. Fourier transforming the temporal produces resonances in frequency corresponding to the modes of the system.

Undoped 2D PC's have been implemented as photonic band-edge lasers, highly reflective mirrors, super-prisms, and lenses [18-21]. However, far more flexibility of PCs can be realized by breaking the symmetry of an ideal PC by introducing defects. Adding or removing dielectric material from a unit cell will create defect modes inside the PBG originating from the dielectric (lower) or air (upper) band as indicated in Fig. 1.5. Using

the solid-state analogy, these modes are called as acceptor and donor modes. The straightforward application of point defects is high-Q microcavities [22-25], since the perturbed site can act like a cavity (EM resonator) surrounded by reflecting walls. The perturbation can be made by increasing or decreasing the radius of the dielectric rods in a low-index background or air holes in a high-index background. That means the effective refractive index of the defect region will be increased or lowered. The lifetime and resonant frequency of the cavity modes can be controlled by the geometry (shape and size) and the refractive index contrast of the structure. High-Q values can be obtained by increasing the number of lattice layers surrounding the cavity. Cavities with small volume and high Q may enable low-threshold lasers and highly efficient light emitting diodes with good temporal and spatial coherence [26-32].

Introducing line defects (adding or removing dielectric material within a certain row or rows of unit cells in the PC) into a PC results in a PCW [33-38]. The wave confinement is achieved by Bragg reflection in transverse directions contrary to the total internal reflection (TIR) that is responsible for the confinement in fiber optics. Since the guiding mechanism in fiber optics and slab waveguides are based on TIR, light is lost around sharp bends. On the other hand, high transmittance for the guided modes through sharp bends in PCWs has been theoretically (Fig. 1.6) and experimentally reported [39,

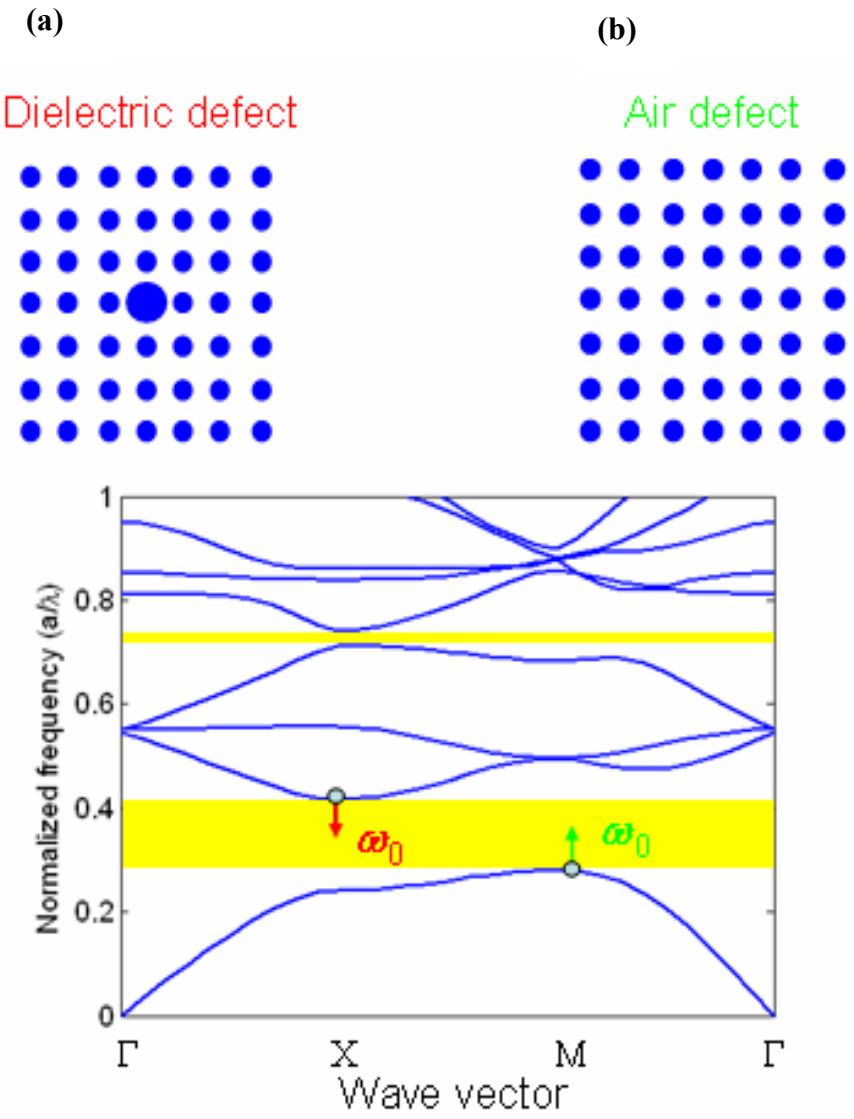

Figure 1.5: Defect modes of a PC obtained by either (a) increasing or (b) reducing the effective index of the unit lattice.

40]. Figure 1.7 shows a T-junction and a splitter where input light is divided equally. Recent experiments demonstrate that propagation loss can be as low as 24 dB/cm [41]. Even though this value is quite high, reducing the loss to an acceptable level may be achieved. Second-harmonic generation [42, 43], all-optical switches [44], optical transistors, and logic gates [45] have been implemented and made the hope of all optical signal processing a possible.

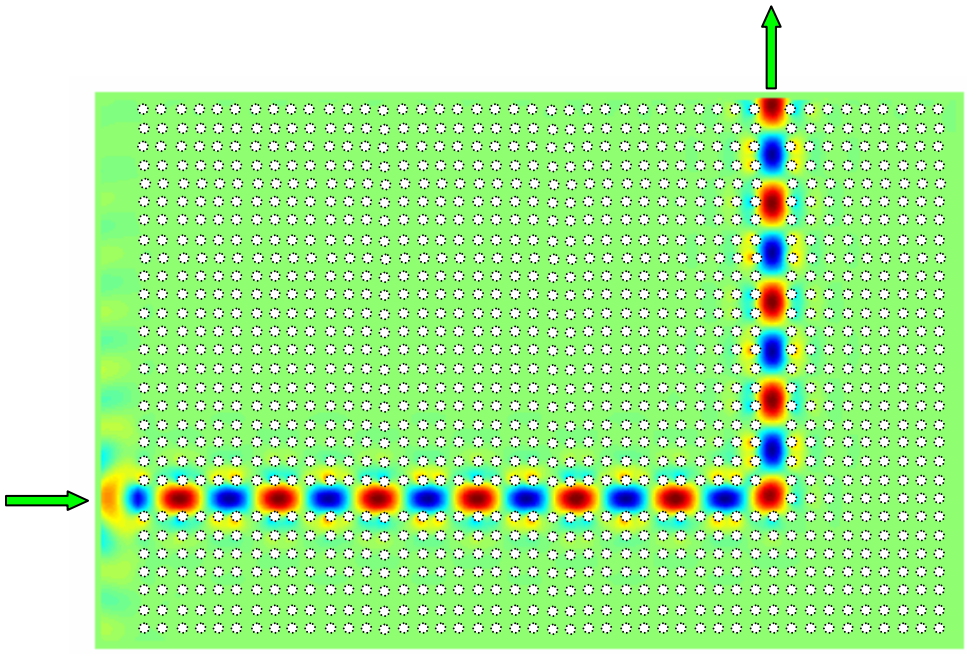

Figure 1.6: A 90^0 2D photonic crystal waveguide bend for square lattice dielectric rods $(\varepsilon = 12, r = 0.2a)$ in air. Two rows of rods are removed to obtain the bend.

In the microwave domain, metallo-dielectric material was mostly used. Metallic lattices have a forbidden band from zero frequency to a plasmon-like frequency f_p. PBGs have been used to improve the gain and far-field pattern of patch antennas in the microwave region [46]. Other applications in this region are high impedance surfaces,

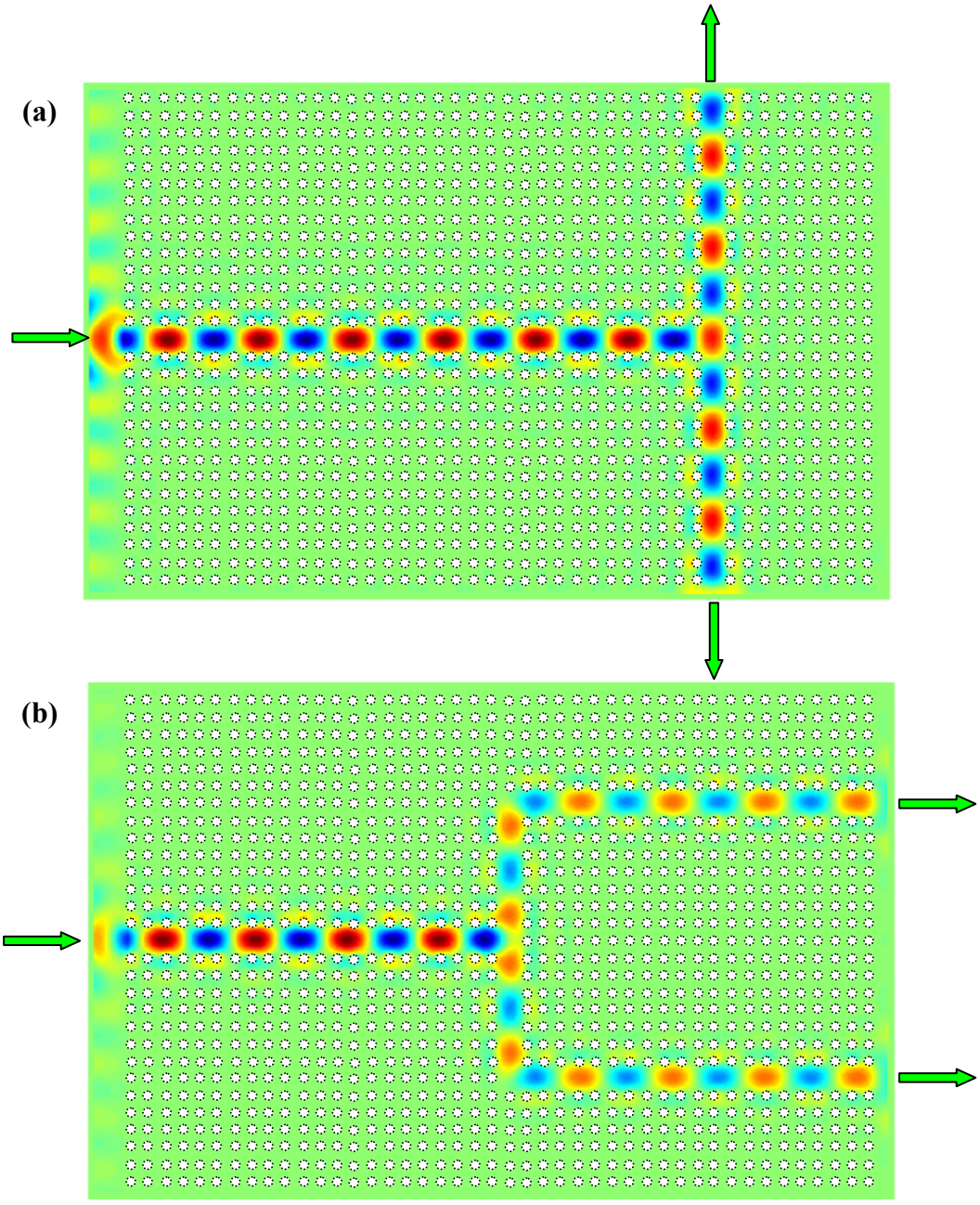

Figure 1.7: (a) T-junction and (b) splitter of 2D square lattice dielectric rods obtained by removal of rods in rows $(\varepsilon = 12, r = 0.2a)$.

compact uniplanar slow-wave lines, and broad-band filters [47, 48]. They are robust and easy to fabricate in this domain. Similar periodic structures such as frequency selective surfaces (FSS) [49] have been demonstrated using PCs. However, fully three-dimensional periodicity and doping, which makes PCs attractive, were missing in FSS.

Recently, PCs have attracted attention for chemical and biological sensing. The main attraction is the ability to tailor the material-EM interaction. It is possible to enhance light-matter interaction as a result of group-velocity engineering. The group velocity is defined as $v_g = c/n_g$ where n_g is group index. Reduction of the group velocity means an increase in the light-matter interaction ($t = 1/v_g$). References [50-52] have recently proposed the use of PCs for chemical and fluid detection. References [50] and [51] used high-Q microcavities for chemical detection. The resonant frequency of the cavity is very sensitive to changes in the refractive index and geometry. Therefore, filling the defect hole with various samples alters the resonant frequencies. In [52], multi-channel PCWs are designed such that the input is guided by a PC line defect and coupled to one of the channels if the fluid is inserted into the air holes of the same channel.

There are still some concerns related to making PCs more functional and practical to deploy in real devices. Some of these issues are how to make PCs tunable, the effects of imperfections, and reducing losses (input-output coupling, scattering) to an acceptable level.

The tunability of any optoelectronic device enhances the functionality, likewise for PC structures. Any material that is sensitive to external parameters such as electric field, temperature, or pressure by means of electro-optic or piezo-optic mechanisms can be utilized to tune the band structure of PCs [53]. Though lithographic tuning by

changing the geometry and dimensions of PC can modify the properties of PCs, it is not practical. Using semiconductor materials and controlling the temperature T and the impurity concentration N, PCs can be made tunable; however, intrinsic absorption losses resulting from the materials are a major drawback [54]. The temperature-dependent refractive index of an infiltrated liquid crystal is also a possible way of making PCs tunable.

Disorder in the refractive index as well as thickness and position variations resulting from fabrication errors have been investigated [55-58]. Their effects on PC characteristics are different. However, when considered together, the refractive index and hole-radius variability have the foremost effect on the PBG. It may not be necessary to have a perfect crystal structure for some cases.

Impedance matching is important to suppress the input coupling loss and hence to enhance the transmission [59]. Low transmission degrades the functionality of PCW-based devices. Therefore, enhanced coupling and transmission through the system are important.

Although PCs in 3D are in many instances difficult to fabricate, nature provides its own structures, such as in opals, iridescent wings of some butterflies and moths, and the dorsal arm plate of the brittlestar *Ophiocoma wendti* [60, 61].

The principles of PCs and their peculiar properties have been described while addressing the foreseen applications. We mentioned some remaining technical challenges, especially for the optics regime.

1.2 Outline of the thesis

The thesis is organized as follows. The historical progress of the PCs is introduced in the introductory section, Chapter I. In Chapter 2, the necessary numerical tools for the study of the PCs are presented along with the important parameters of the PCs that determine mainly the occurrence of the photonic band gap. The plane wave expansion method and the finite-difference time-domain technique (FDTD) are formulated in that chapter. The FDTD method is modified in a way that dispersive materials can be analyzed. The next two chapters, Chapter III and IV, deal with the application of PCs for bio-sensing. The former one studies PCWs and the latter one implements coupled-resonator optical waveguides (CROW) for the same purpose. The preliminary experimental data is provided in Chapter III. The focuses of these aforementioned chapters are the special application of PCs i.e., bio-sensing. To address some of the challenges in the field is the target of the coming sections.

A novel PC called annular PC is the topic of Chapter V for full photonic band gap control by tuning the TE and TM polarizations independently. The two-dimensional PC heterostructure waveguide concept is introduced for the purpose of enhancing poor transmission coefficient through the sharp bends and the conclusions and future research directions are the subjects of the last two sections of the thesis, Chapter VI and VII, respectively. The relevant references are listed thereafter.

CHAPTER II

The study of photonic crystals

In this chapter, two numerical techniques which provide insights and great flexibility for the design and analysis of PCs are presented.

2.1 Introduction to the numerical methods

The analysis of PCs has been performed by various numerical approaches. The plane-wave method (PWM) and finite-difference time-domain (FDTD) method are widely used techniques for the investigation of PCs. Their strengths and weaknesses compared to each other are as follows.

The full vector nature of the EM field has to be kept to accurately analyze the strongly modified dielectric materials as the scalar-wave approximation does not produce accurate results. The PWM, a frequency domain formulation, is superior in calculating the band diagrams and mode field patterns. However, the dielectric constant of the PC material should be frequency independent and loss-free. In the case where the pure periodicity of the crystal is broken, or there is a defect, the so called supercell approach has to be used, which is computationally heavy as the number of plane waves used in the expansion increases. On the other hand, FDTD provides EM field variations in space with respect to time. The transmission and reflection spectrum of finite structures can be evaluated easily and the wave propagation trough the medium can be observed in time. As a result, this method maybe more favorable to direct comparison with experiments. In addition, frequency dependence and loss can be included in this method. However, band diagram calculations are tedious with the FDTD as the selection of the initial excitation field is important to excite all possible modes. Similarly, the detection points shouldn't be

placed at a high symmetry point. Moreover, if the structure has very sharp edges then uniform meshing may not predict the characteristics well enough. It may be needed to use non-uniform meshing and as a result, the size of the computational domain increases. Hence, the complementary use of these two methods depending on the case is beneficial for the study of periodic dielectric structures. As a result, I performed the designs and analysis of PC structures employing these two methods. The following section highlights the basic formulation of the PWM and FDTD for one- two- and three-dimensional cases.

2.2 The plane wave expansion method

Before the formulation, I explain briefly some of the frequently used terminologies and basic background borrowed mostly from the solid-state physics. These analogies greatly help the elucidation of the concepts by well know field, solid state electronics.

2.2.1 The theory of band structures

Photonic band structure calculation by solving Maxwell's equations has borrowed many terms from electronic band structure, which solves the Schrödinger's equation. The aim is to determine the allowed frequencies for a given wave vector k as well as the mode functions. The equations can be used to solve the eigenvalue problem for all directions. The Brillouin zone (BZ) represents the full symmetry of the lattice in reciprocal space. The irreducible Brillouin zone (IBZ) is the smallest region within the BZ for which the dispersion characteristics of the lattice is not related by symmetry. The behavior of the entire crystal can be obtained by studying the unit lattice in the IBZ due to periodicity. One cannot obtain independent solutions if the analysis is carried out outside the IBZ

because of the connection that is satisfied by reciprocal lattice vector. $\omega_i(k) = \omega_j(k') = \omega_j(k+G)$ where G is the reciprocal lattice vector.

Bloch's theorem states that the plane wave is modulated by a function with the periodicity of the medium. The periodic dielectric function is translation invariant by any lattice vector R, so $\varepsilon(r) = \varepsilon(r+R)$. The primitive lattice vectors are the shortest distances to the nearest neighboring points on the lattice $\vec{a}_1$, $\vec{a}_2$, and $\vec{a}_3$ multiplied by any integer number pairs (m,n,l) constructing the three dimensional periodic dielectric structures in terms of basis vector $R = m\vec{a}_1 + n\vec{a}_2 + l\vec{a}_3$. The solution obtained by Fourier transforming $\varepsilon(r)$, and $\varepsilon(r+R)$ has to be equal (differs only by a multiplicative constant) since $\varepsilon(r) = \varepsilon(r+R)$. That means the lattice is invariant from one lattice point to another. The phase factor $e^{jG\cdot R}$ has to be equal to 1 basing the needed condition for the reciprocal lattice vectors G which is composed of linear combinations of the primitive lattice vectors, $G \cdot R = 2\pi N$. Given the lattice vectors, the reciprocal lattice vectors can be calculated by $\vec{b}_1 = 2\pi \frac{\vec{a}_2 \times \vec{a}_3}{\vec{a}_1 \cdot \vec{a}_2 \times \vec{a}_3}$, $\vec{b}_2 = 2\pi \frac{\vec{a}_3 \times \vec{a}_1}{\vec{a}_1 \cdot \vec{a}_2 \times \vec{a}_3}$, and $\vec{b}_3 = 2\pi \frac{\vec{a}_1 \times \vec{a}_2}{\vec{a}_1 \cdot \vec{a}_2 \times \vec{a}_3}$, satisfying the condition; $\vec{a}_i \cdot \vec{b}_j = 2\pi\delta_{ij}$.

The regular scattering shapes (circular, sphere) facilitate obtaining the Fourier transforms (FT) of dielectric function in analytical forms. Representing the FT pair of permittivity function as $\boldsymbol{\varepsilon}(\boldsymbol{r}) \leftrightarrow \boldsymbol{\varepsilon}(\boldsymbol{G})$, and using the shifting property of FT's in the following form $\sum_{r_i} \boldsymbol{\varepsilon}(\boldsymbol{r}+\boldsymbol{r}_i) \Leftrightarrow \sum_{r_i} \boldsymbol{e}^{jG\cdot r_i} \boldsymbol{\varepsilon}(\boldsymbol{G})$ help calculating the band diagrams.

2.2.2 The Formulation of PWM

We start with Maxwell's equations

$$\begin{aligned} \nabla \times E(r,t) &= -\frac{\partial}{\partial t} B(r,t) \\ \nabla \times H(r,t) &= \frac{\partial}{\partial t} D(r,t) \\ \nabla \cdot D(r,t) &= \rho \\ \nabla \cdot B(r,t) &= 0, \end{aligned} \tag{2.1}$$

where E is the electric field, H is the magnetic field, B is the magnetic induction, D is the electric displacement and ρ is the charge density. The assumptions for the formulation and analysis carried out for the PWM are non-magnetic materials ($\mu = \mu_0$), source free medium ($\rho = 0$), linear optic regime where D and E (isotropic medium) are related by $D = \varepsilon_0 E + P = \varepsilon_0 (1 + \chi_e) E = \varepsilon E$, and neglecting the higher order terms where P is the electric polarization and χ_e is the electric susceptibility function. Moreover, the permittivity is taken as frequency independent, real valued (lossless medium) and position dependent. Harmonic time dependent forms $e^{-i\omega t}$ for the fields E and H with the above assumptions help to write equation (2.1) into as follows:

$$\begin{aligned} \nabla \times E(r) &= -j\omega\mu(r) H(r) \\ \nabla \times H(r) &= j\omega\varepsilon(r) E(r) \\ \nabla \cdot E(r) &= 0 \\ \nabla \cdot H(r) &= 0. \end{aligned} \tag{2.2}$$

Eliminating E and rearranging in terms of H yields

$$\nabla \times \left[\frac{1}{\boldsymbol{\varepsilon}(\boldsymbol{r})} \nabla \times \boldsymbol{H} \right] = \frac{\boldsymbol{\omega}^2}{\boldsymbol{c}^2} \boldsymbol{H} . \tag{2.3}$$

This is the characteristic (eigenvalue) equation where $c = 1/\sqrt{\mu_0 \varepsilon_0}$ is the speed of light. Similar derivation can be obtained by eliminating H in favor of E, however, then the equation will not be Hermitian. The Hermitian operators have real eigenvalues and orthogonal eigenfunctions. Expanding H in terms of plane waves by means of Bloch's theorem we obtain

$$H(r) = \sum_{G} \sum_{\lambda=1,2} H_{G,\lambda} \hat{e}_{\lambda} e^{j(k+G)r} , \tag{2.4}$$

where $\hat{e}_1$ and $\hat{e}_2$ are unit vectors chosen such that they are perpendicular to $k+G$ due to the transverse requirement (i.e. $\nabla \cdot H = 0$). Substituting equation (2.4) into equation (2.3) the following expressions is obtained after some algebra,

$$\sum_{G'} |k+G||k+G'| \varepsilon^{-1}(G-G') \begin{pmatrix} e_G^2 \cdot e_{G'}^2 & -e_G^2 \cdot e_{G'}^1 \\ -e_G^1 \cdot e_{G'}^2 & e_G^1 \cdot e_{G'}^1 \end{pmatrix} \begin{pmatrix} h_{G'}^1 \\ h_{G'}^2 \end{pmatrix} = \left(\frac{\omega}{c} \right)^2 \begin{pmatrix} h_G^1 \\ h_G^2 \end{pmatrix}. \tag{2.5}$$

There are two ways to proceed; either expand $\varepsilon(r)$ or $\frac{1}{\varepsilon(r)}$. I selected the first way, *the Inverse Expansion Method,* in which $\varepsilon(r)$ is Fourier transformed first and then inversion is taken. [$\varepsilon(r) \leftrightarrow \varepsilon(G) \rightarrow \varepsilon(G-G') \rightarrow \varepsilon^{-1}(G-G')$]. Either way, however, has to give the same results as long as sufficient number of plane waves is used to truncate

the infinite sum. The periodic dielectric function can be expanded in a Fourier series of plane waves $\varepsilon(r)=\sum_{G}\varepsilon(G)e^{iG\cdot r}$, where G is the reciprocal lattice vector representing the allowed values of the wave vectors. Similarly, the inverse FT is in the form of $\varepsilon(G)=\frac{1}{A}\int_{A}\varepsilon(r)e^{-G\cdot r}dr$. The spatial and frequency domain lattices are formed by R and G vectors respectively.

2.2.3 Two-Dimensional PWM

The structure is assumed to be infinitely long in the third dimension. The decomposition into TE (E_x, E_y, H_z) and TM (H_x, H_y, E_z) polarizations is possible for the two-dimensional case if the structure is uniform along the z-direction. For each propagation direction the eigenvalues (frequencies) are solved and the corresponding eigenmodes are calculated. For the TE polarization (E_x, E_y, H_z):

$$\begin{aligned}\frac{\partial E_y(r)}{\partial x}-\frac{\partial E_x(r)}{\partial y}&=j\frac{\omega}{c}H_z(r)\\ \frac{\partial H_z(r)}{\partial x}&=j\frac{\omega}{c}\varepsilon(r)E_y(r)\\ \frac{\partial H_z(r)}{\partial y}&=-j\frac{\omega}{c}\varepsilon(r)E_x(r).\end{aligned}\tag{2.6}$$

After arranging the above equations by eliminating E_x and E_y in favor of H_z one can obtain

$$\frac{\partial}{\partial x}\left(\frac{1}{\varepsilon(r)}\frac{\partial}{\partial x}H_z(r)\right)+\frac{\partial}{\partial y}\left(\frac{1}{\varepsilon(r)}\frac{\partial}{\partial y}H_z(r)\right)+\left(\frac{\omega}{c}\right)^2H_z(r)=0.\tag{2.7}$$

Expanding $\varepsilon(x,y)$ and $H_z(x,y)$ in the k-space and substituting them into equation (2.7) we obtain

$$\sum_{G'}(k+G)(k+G')\varepsilon^{-1}(G-G')H_{G',2}=\frac{\omega^2}{c^2}H_{G,2}\ . \tag{2.8}$$

For the TM polarization (H_x,H_y,E_z) case;

$$\begin{aligned}\frac{\partial H_y(r)}{\partial x}-\frac{\partial H_x(r)}{\partial y}&=-j\frac{\omega}{c}\varepsilon(r)E_z(r)\\ \frac{\partial E_z(r)}{\partial x}&=-j\frac{\omega}{c}H_y(r)\\ \frac{\partial E_z(r)}{\partial y}&=j\frac{\omega}{c}H_x(r).\end{aligned} \tag{2.9}$$

Similarly eliminating H_x and H_y in favor of E_z yields

$$\frac{1}{\varepsilon(r)}\left[\frac{\partial^2}{\partial x^2}+\frac{\partial^2}{\partial y^2}\right]E_z(r)+\left(\frac{\omega}{c}\right)^2E_z(r)=0\,, \tag{2.10}$$

and finally

$$\sum_{G'}|k+G||k+G'|\varepsilon^{-1}(G-G')H_{G',1}=\frac{\omega^2}{c^2}H_{G,1}\,. \tag{2.11}$$

It should be noted that if the $\varepsilon(r)$ is constant then the equations turn into the usual wave equations commonly employed in electromagnetic.

2.2.4 Two-dimensional photonic crystals

The compact from of the permittivity function in k-space can be written as

$$\varepsilon(G)=\frac{1}{A}\int_{A}\varepsilon(r)e^{-iG\cdot r}dr \;\Rightarrow\; \varepsilon(G)=\begin{cases}\varepsilon_b+f(\varepsilon_a-\varepsilon_b) & G=0\\ (\varepsilon_a-\varepsilon_b)I(G) & G\neq 0\end{cases} \tag{2.12}$$

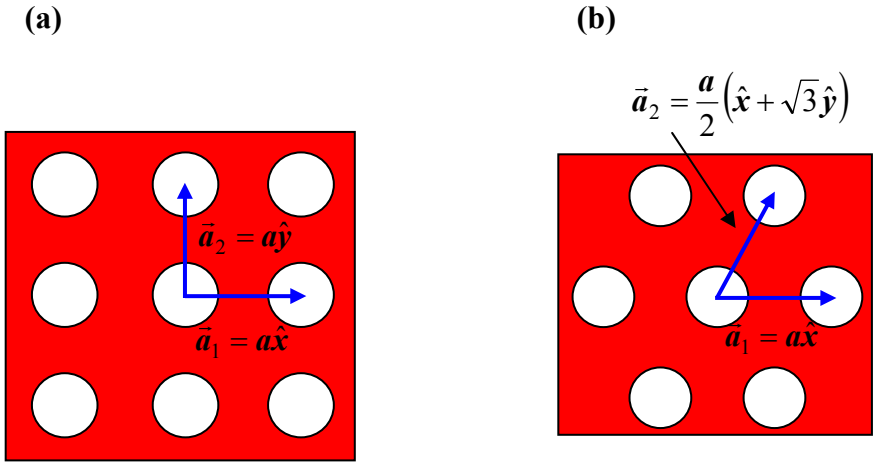

Figure 2.1 Schematics of two-dimensional photonic crystal for (a) square and (b) triangular lattice. Unit lattice vectors $\vec{a}_1$ and $\vec{a}_2$ are shown.

where ε_a and ε_b represent the dielectric constants of the inner and the background medium, respectively, f is the filling fraction and a geometric factor $I(G)$ is defined as $I(G)=\frac{1}{A}\int_{A}e^{-iG.r}dr$. One only needs to calculate the $I(G)$ with a given lattice type and filling fraction. The geometric factor is in the form of $I(G)=2f\frac{J_1(GR)}{GR}$ for square and triangular lattice where J_1 is the first-order Bessel function of the first kind. Figure 2.1 shows 2D (top view) square and triangular lattice PC and the basis vectors, $\vec{a}_1$ and

$\vec{a}_2$.The primitive lattice vectors for the square lattice are then $\vec{b}_1 = \frac{2\pi}{a}\hat{x}$, and $\vec{b}_2 = \frac{2\pi}{a}\hat{y}$, and for the triangular lattice, they are $\vec{b}_1 = \frac{4\pi}{a\sqrt{3}}\left(\frac{\sqrt{3}}{2}\hat{x} - \frac{1}{2}\hat{y}\right)$, and $\vec{b}_2 = \frac{4\pi}{a\sqrt{3}}\hat{y}$. The crystal structure, BZ and the band diagram are shown in Fig. 2.2 and 2.3 for the square and triangular lattices, respectively. As can be seen from the figures, the first one has band gap only for TM modes, whereas the second one provides band gap for the TE polarization.

2.2.5 Three-dimensional photonic crystals

The real-space primitive vectors for the fcc lattice are: $\vec{a}_1 = \frac{a}{2}(\hat{x} + \hat{y})$, $\vec{a}_2 = \frac{a}{2}(\hat{y} + \hat{z})$, and $\vec{a}_3 = \frac{a}{2}(\hat{x} + \hat{z})$. The reciprocal lattice vectors can be evaluated straightforwardly and they are: $\vec{b}_1 = \frac{2\pi}{a}(\hat{x} + \hat{y} - \hat{z})$, $\vec{b}_2 = \frac{2\pi}{a}(-\hat{x} + \hat{y} + \hat{z})$, and $\vec{b}_3 = \frac{2\pi}{a}(\hat{x} - \hat{y} + \hat{z})$. The geometric factor is $I(G) = 3f\frac{1}{(GR)^3}[\sin(GR) - GR\cos(GR)]$.

The diamond lattice has the same primitive lattice vectors as fcc lattice but there are two dielectric spheres within the unit cell and their positions are offset by $\vec{r}_0 = \frac{a}{8}(\hat{x} + \hat{y} + \hat{z})$ and $\vec{r}_0^{\,'} = -\frac{a}{8}(\hat{x} + \hat{y} + \hat{z})$. If the dielectric spheres are identical then the geometric factor is $I(G) = 3f\frac{1}{(GR)^3}[\sin(GR) - GR\cos(GR)]\cos(G \cdot r_0)$. The lattice structure, and the band structures of fcc lattice and diamond lattice of dielectric spheres are shown in Fig. 2.4 and 2.5, respectively. As can be seen, the previous one does not have a PBG but the latter one has complete PBG.

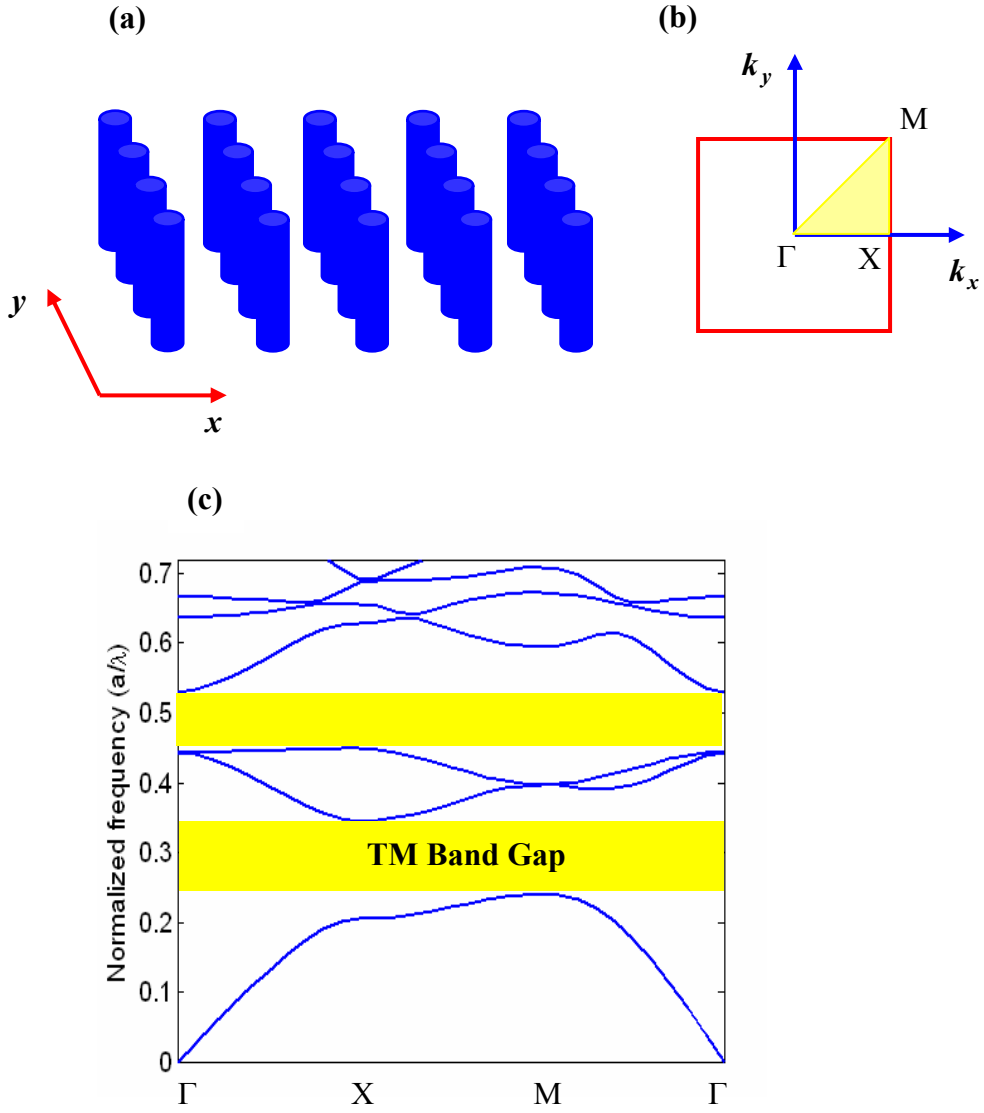

Figure 2.2: (a) Square lattice photonic crystal, rods in ir $r = 0.25a$, $\varepsilon = 13$. (b) Brillouin zone of square lattice and irreducible BZ is shaded. (c) Band diagram of the square lattice.

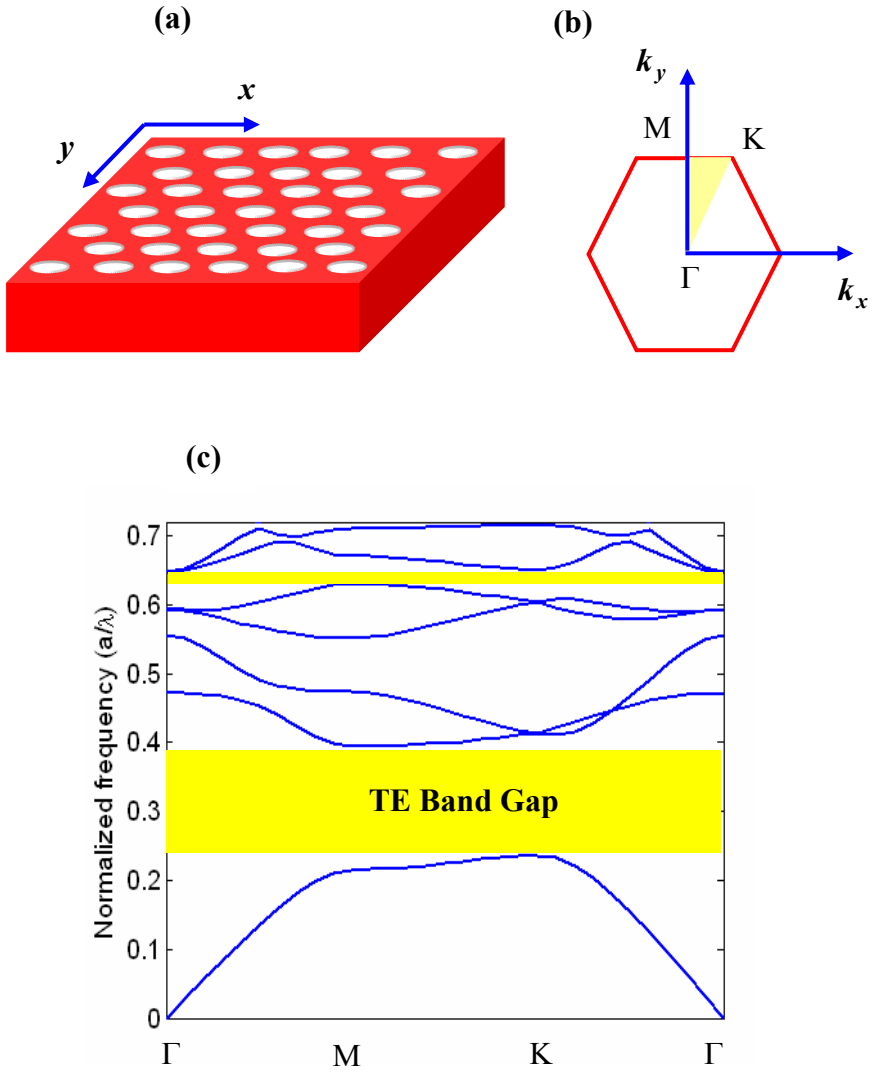

Figure 2.3: (a) Triangular lattice photonic crystal, air holes in dielectric background $r = 0.40a$, $\varepsilon = 13$. (b) Brillouin zone of the triangular lattice. (c) Dispersion diagram.

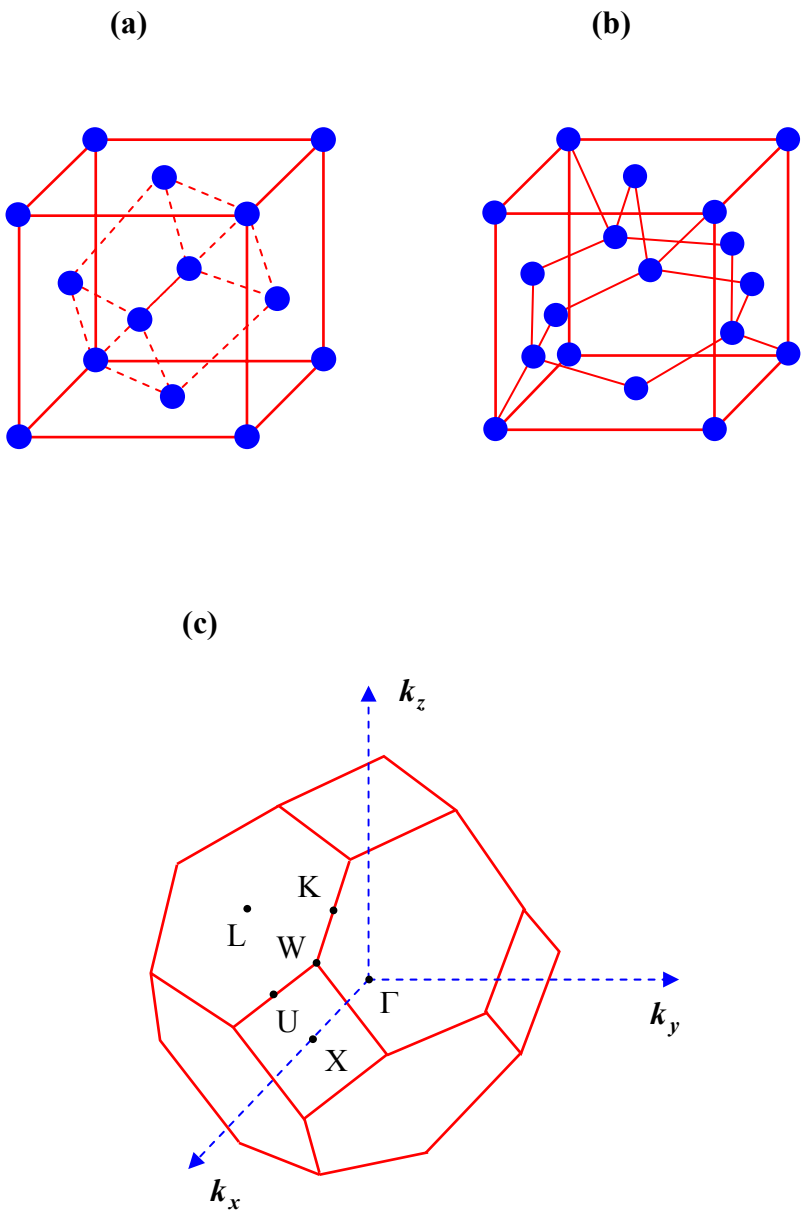

Figure 2.4: Schematics of (a) face-centered cubic lattice, and (b) diamond lattice. (c) Brillouin zone of a face-centered cubic lattice.

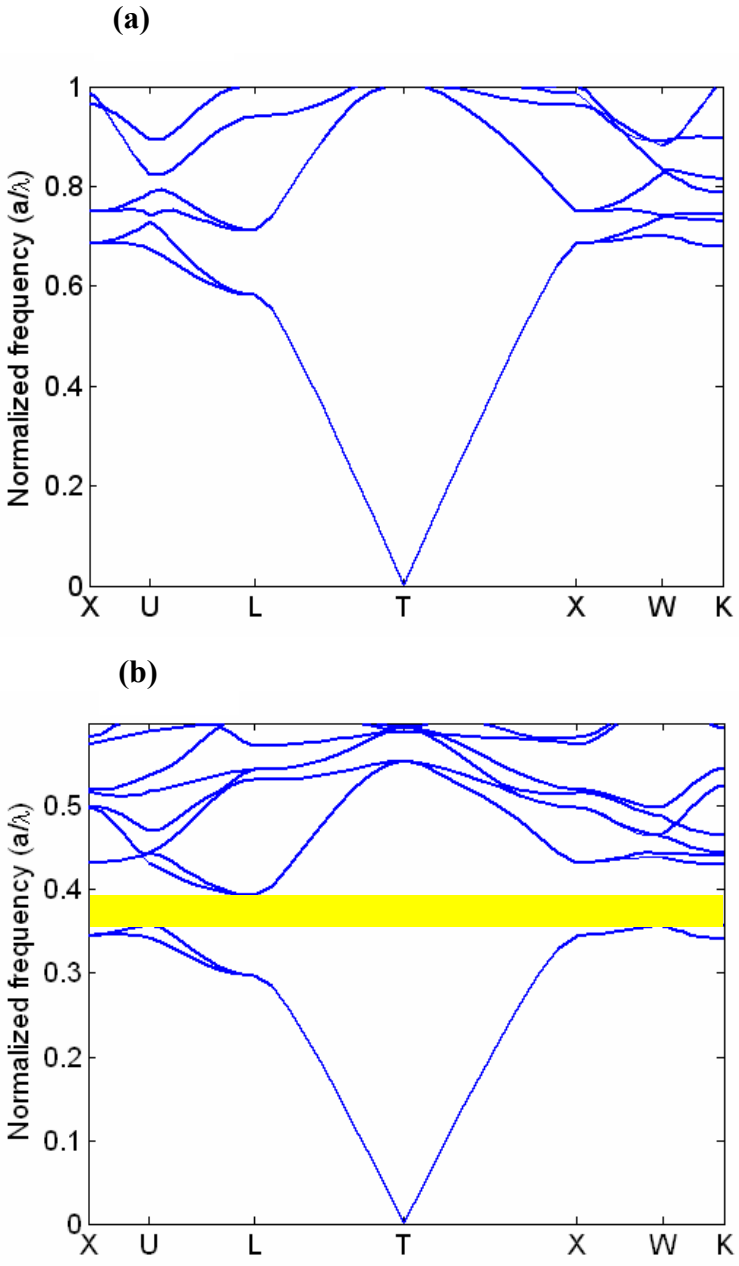

Figure 2.5: Band diagrams of (a) face-centered cubic lattice, and (b) diamond lattice with $r = 0.20a$ and $\varepsilon = 13$.

2.2.6 Photonic crystal parameters

The symmetry and the topology of the lattice are the foremost important properties that determine the overall photonic band structure. The symmetry of the lattice can be square or triangle for the 2D case, and simple cubic, body centered cubic, or face centered cubic for the 3D case. The topology of the lattice can be either in a connected form or an isolated structure. There are strict requirements that a crystal should posses to provide full band gaps in addition to the aforementioned conditions. These are high index-contrast ratio, and the filling fraction. For example, there is band gap as long as $n_1 \neq n_2$ for a 1D PC; however, in other cases (2D and 3D) the ratio has to be very large for the pseudo gaps to overlap. Two dimensional PCs are typically quite polarization sensitive, so favorable conditions for PBG are different for different polarizations. Usually, high filling fraction is required for TE modes but low filling fraction is favored for the TM modes.

The scalability of Maxwell's equations imposes that there is no fundamental length scale for photonic crystal as opposed to the fundamental length scale of semiconductor crystals (Bohr radius). Moreover, as long as the ratio of high refractive index to the low one keeps the same, the frequency is scaled accordingly. Figure 2.7 shows the variation of the lowest two bands that determine the band gap for TE modes in a triangular lattice PC. As can be seen, larger r/a and n_2/n_1 values are desirable for wide PBG.

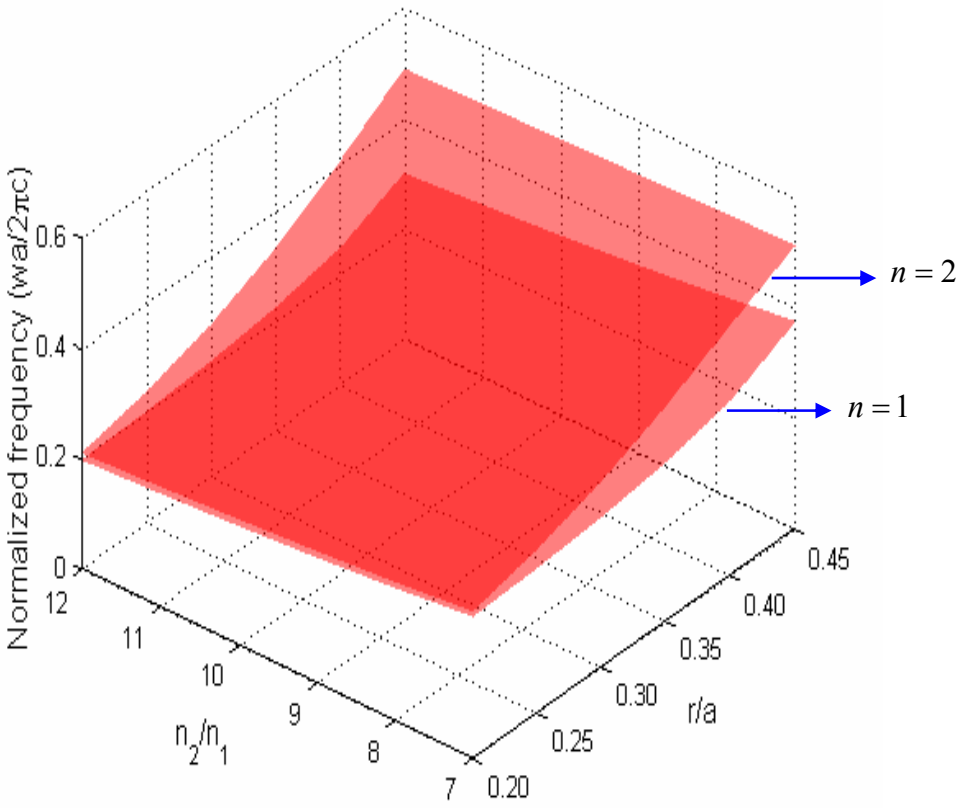

Figure 2.6: Photonic band gap variations of the triangular lattice air holes in dielectric background $(\varepsilon_b = 13)$ for TE modes. The radius of the hole and the refractive index of the background are varied.

2.3 Finite-Difference Time-Domain Method

As the name implies, the FDTD method is the formulation of Maxwell's equations in the time domain and this method was introduced by K. Yee in 1966 [62]. Maxwell's curl equations are discretized in space and time by approximating with centered two-point finite differences. The flexibility and capability of studying complex structures, easy implementation, visualizing the time-varying fields with the volume of space, handling nonlinear, frequency dependent, and conducting materials, obtaining easily broad spectral information by a single run made FDTD a powerful and versatile numerical tool. The memory requirement is linearly proportional with the volume of the simulated structure.

2.3.1 Formulation of FDTD Method

Assume f (not filling factor) is a function of space and time $f = f(x,t)$. The space and time derivatives are approximated by centered two-point finite differences with second order accuracy

$$\left.\frac{\partial f}{\partial x}\right|_{x=x_0} = \frac{f(x = x_0 + \Delta x/2, t) - f(x = x_0 - \Delta x/2, t)}{\Delta x} + O(\Delta x^2)$$
$$\left.\frac{\partial f}{\partial t}\right|_{t=t_0} = \frac{f(x, t = t_0 + \Delta t/2) - f(x, t = t_0 - \Delta t/2)}{\Delta t} + O(\Delta t^2). \quad (2.13)$$

The adapted notation to represent the space and time variations of a function f in 3D is $f(i,j,k,n) = f(i\Delta x, j\Delta y, k\Delta z, n\Delta t)$. To introduce the basic background of the method 1D FDTD is good point to start.

2.3.2 One-dimensional FDTD: TEM Mode

Assume the propagation is in x direction and field is y-polarized, then Maxwell's equations can be written as

$$\frac{\partial E_y}{\partial t} = -\frac{1}{\varepsilon}\left[\frac{\partial H_z}{\partial x} + \sigma E_y\right]$$
$$\frac{\partial H_z}{\partial t} = -\frac{1}{\mu}\left[\frac{\partial E_y}{\partial x} + \sigma^* H_z\right]. \tag{2.14}$$

The space derivatives are updated at fixed time step, and time derivatives are updated at fixed positions. The material parameters should be assigned at spatial points where each field component is defined in each cell. Figure 2.7 indicates the fields E_y and H_z assignment with respect to time and space. From Fig. 2.7,

$$\frac{\partial H_z}{\partial x} = \frac{H_z^{n+\frac{1}{2}}(i+1/2) - H_z^{n+\frac{1}{2}}(i-1/2)}{\Delta x}$$
$$\frac{\partial E_y}{\partial t} = \frac{E_y^{n+1}(i) - E_y^{n}(i)}{\Delta t}. \tag{2.15}$$

Arranging these expressions yields

$$E_y^{n+1}(i) = \frac{2\varepsilon(i) - \Delta t\sigma(i)}{2\varepsilon(i) + \Delta t\sigma(i)} E_y^n(i) - \frac{2\Delta t}{2\varepsilon(i) + \Delta t\sigma(i)} \left[\frac{H_z^{n+\frac{1}{2}}(i+1/2) - H_z^{n+\frac{1}{2}}(i-1/2)}{\Delta x} \right]$$

$$H_z^{n+\frac{1}{2}}(i-1/2) = \frac{2\mu(i-1/2) - \Delta t\sigma^*(i-1/2)}{2\mu(i-1/2) + \Delta t\sigma^*(i-1/2)} H_z^{n-\frac{1}{2}}(i-1/2) - \frac{2\Delta t}{2\mu(i-1/2) + \Delta t\sigma^*(i-1/2)} \left[\frac{E_y^n(i) - E_y^n(i-1)}{\Delta x} \right]. \quad (2.16)$$

While obtaining the above equations, the conductive loss term is approximated by a semi-implicit form using time average

$$E_y^{n+\frac{1}{2}}(i) = \frac{E_y^{n+1}(i) + E_y^n(i)}{2} \quad (2.17)$$

The two extreme cases worth in noting are $\sigma = 0$ (lossless material) case and $\sigma >> 1$ (implementation of the PEC boundary condition) case. To update E_y at the boundary, the value of the H_z field outside of the domain is needed which is not available. So the appropriate termination of the computational domain is required. I will explain later the periodic and absorbing boundary conditions.

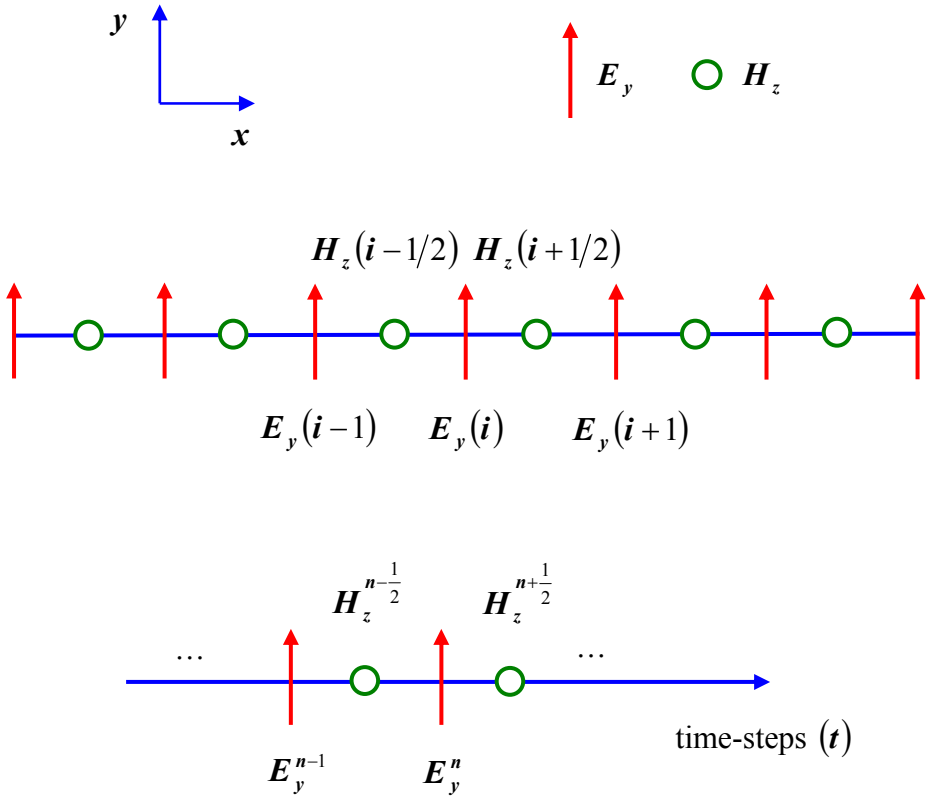

Figure 2.7: Staggered spatial meshes and leapfrog time steps.

2.3.3 Two-dimensional FDTD Method

The Maxwell's equations can be written for TE polarizations as

$$\frac{\partial E_x}{\partial t} = \frac{1}{\varepsilon}\left[\frac{\partial H_z}{\partial y} - \sigma E_x\right]$$

$$\frac{\partial E_y}{\partial t} = -\frac{1}{\varepsilon}\left[\frac{\partial H_z}{\partial x} + \sigma E_y\right] \tag{2.18}$$

$$\frac{\partial H_z}{\partial t} = \frac{1}{\mu}\left[\frac{\partial E_x}{\partial y} - \frac{\partial E_y}{\partial x} - \sigma^* H_z\right]$$

and for TM polarization as

$$\frac{\partial H_x}{\partial t} = -\frac{1}{\mu}\left[\frac{\partial E_z}{\partial y} + \sigma^* H_x\right]$$

$$\frac{\partial H_y}{\partial t} = \frac{1}{\mu}\left[\frac{\partial E_z}{\partial x} - \sigma^* H_y\right] \tag{2.19}$$

$$\frac{\partial E_z}{\partial t} = \frac{1}{\varepsilon}\left[\frac{\partial H_y}{\partial x} - \frac{\partial H_x}{\partial y} - \sigma E_z\right]$$

Figure 2.8 and 2.9 show the assignments of field variables through the computational domain. Similar to the 1D case, the final form of 2D case can be obtained in a similar way.

$$E_x^{n+1}(i+1/2,j)=\frac{2\varepsilon(i+1/2,j)-\Delta t\sigma(i+1/2,j)}{2\varepsilon(i+1/2,j)+\Delta t\sigma(i+1/2,j)}E_x^n(i+1/2,j)+$$
$$\frac{2\Delta t}{2\varepsilon(i+1/2,j)+\Delta t\sigma(i+1/2,j)}$$
$$\left[\frac{H_z^{n+\frac{1}{2}}(i+1/2,j+1/2)-H_z^{n-\frac{1}{2}}(i+1/2,j-1/2)}{\Delta y}\right]$$

$$E_y^{n+1}(i,j+1/2)=\frac{2\varepsilon(i,j+1/2)-\Delta t\sigma(i,j+1/2)}{2\varepsilon(i,j+1/2)+\Delta t\sigma(i,j+1/2)}E_y^n(i,j+1/2)-$$
$$\frac{2\Delta t}{2\varepsilon(i,j+1/2)+\Delta t\sigma(i,j+1/2)}$$
$$\left[\frac{H_z^{n+\frac{1}{2}}(i+1/2,j+1/2)-H_z^{n+\frac{1}{2}}(i-1/2,j+1/2)}{\Delta x}\right] \qquad (2.20)$$

$$H_z^{n+\frac{1}{2}}(i+1/2,j+1/2)=\frac{2\mu(i+1/2,j+1/2)-\Delta t\sigma^*(i+1/2,j+1/2)}{2\mu(i+1/2,j+1/2)+\Delta t\sigma^*(i+1/2,j+1/2)}$$
$$H_z^{n-\frac{1}{2}}(i+1/2,j+1/2)+$$
$$\frac{2\Delta t}{2\mu(i+1/2,j+1/2)+\Delta t\sigma^*(i+1/2,j+1/2)}$$
$$\left[\begin{array}{c}\dfrac{E_x^n(i+1/2,j+1)-E_x^n(i+1/2,j)}{\Delta y}\\ -\dfrac{E_y^n(i+1,j+1/2)-E_y^n(i,j+1/2)}{\Delta x}\end{array}\right].$$

The formulation for the TM case is straightforward with only modification of placing the E-field on the grid point.

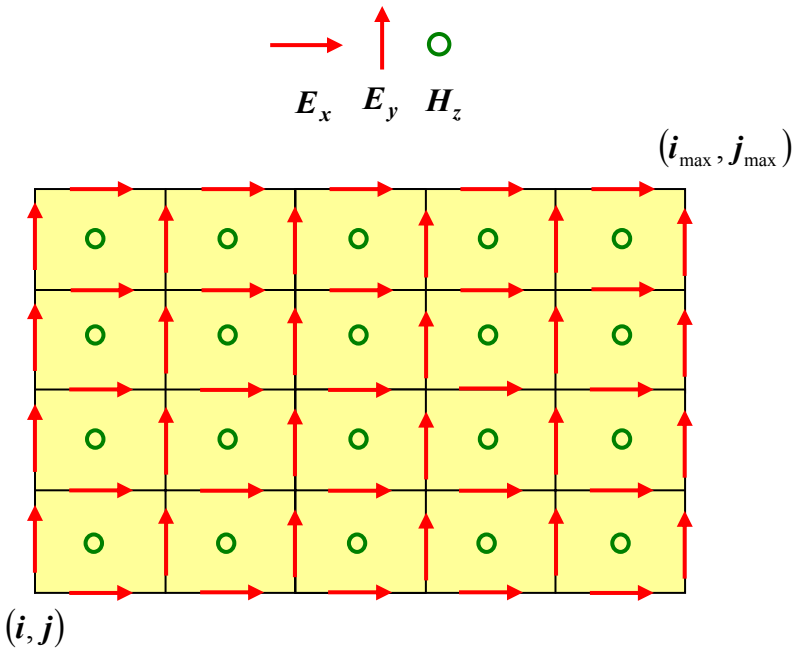

Figure 2.8: Spatial arrangements of field variables in the FDTD for two dimensional TE case.

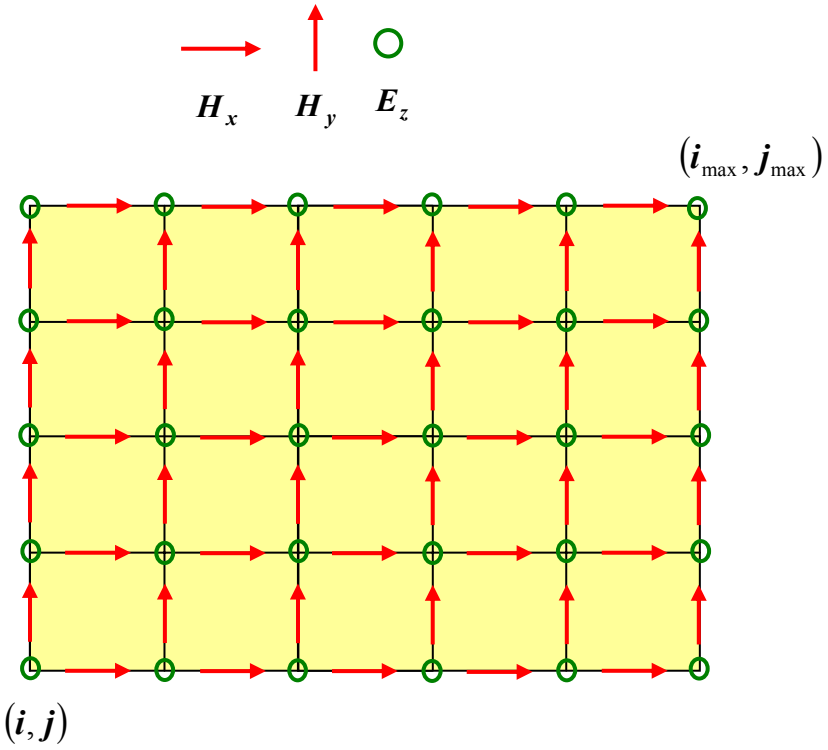

Figure 2.9: Spatial arrangements of field variables in the FDTD for two dimensional TM case.

2.3.4 Three-dimensional FDTD Method

In 3D case, all the six field components are coupled;

$$\begin{aligned}
\frac{\partial E_x}{\partial t} &= \frac{1}{\varepsilon}\left[\frac{\partial H_z}{\partial y} - \frac{\partial H_y}{\partial z} - \sigma E_x\right], \\
\frac{\partial E_y}{\partial t} &= \frac{1}{\varepsilon}\left[\frac{\partial H_x}{\partial z} - \frac{\partial H_z}{\partial x} - \sigma E_y\right], \\
\frac{\partial E_z}{\partial t} &= \frac{1}{\varepsilon}\left[\frac{\partial H_y}{\partial x} - \frac{\partial H_x}{\partial y} - \sigma E_z\right], \\
\frac{\partial H_x}{\partial t} &= \frac{1}{\mu}\left[\frac{\partial E_y}{\partial z} - \frac{\partial E_z}{\partial y} - \sigma^* H_x\right], \\
\frac{\partial H_y}{\partial t} &= \frac{1}{\mu}\left[\frac{\partial E_z}{\partial x} - \frac{\partial E_x}{\partial z} - \sigma^* H_y\right], \\
\frac{\partial H_z}{\partial t} &= \frac{1}{\mu}\left[\frac{\partial E_x}{\partial y} - \frac{\partial E_y}{\partial x} - \sigma^* H_z\right].
\end{aligned} \tag{2.21}$$

Referring to Fig. 2.10, the above differential equations can be formulated in terms of discrete forms as follows

$$E_x^{n+1}(i+1/2,j,k)=\frac{2\varepsilon(i+1/2,j,k)-\Delta t\sigma(i+1/2,j,k)}{2\varepsilon(i+1/2,j,k)+\Delta t\sigma(i+1/2,j,k)}E_x^n(i+1/2,j,k)+$$
$$\frac{2\Delta t}{2\varepsilon(i+1/2,j,k)+\Delta t\sigma(i+1/2,j,k)}$$
$$\left[\begin{array}{l}\dfrac{H_z^{n+\frac{1}{2}}(i+1/2,j+1/2,k)-H_z^{n+\frac{1}{2}}(i+1/2,j-1/2,k)}{\Delta y}\\ -\dfrac{H_y^{n+\frac{1}{2}}(i+1/2,j,k+1/2)-H_y^{n+\frac{1}{2}}(i+1/2,j,k-1/2)}{\Delta z}\end{array}\right],$$

$$E_y^{n+1}(i,j+1/2,k)=\frac{2\varepsilon(i,j+1/2,k)-\Delta t\sigma(i,j+1/2,k)}{2\varepsilon(i,j+1/2,k)+\Delta t\sigma(i,j+1/2,k)}E_y^n(i,j+1/2,k)+$$
$$\frac{2\Delta t}{2\varepsilon(i,j+1/2,k)+\Delta t\sigma(i,j+1/2,k)}$$
$$\left[\begin{array}{l}\dfrac{H_x^{n+\frac{1}{2}}(i,j+1/2,k+1/2)-H_x^{n+\frac{1}{2}}(i,j+1/2,k-1/2)}{\Delta z}\\ -\dfrac{H_z^{n+\frac{1}{2}}(i+1/2,j+1/2,k)-H_z^{n+\frac{1}{2}}(i-1/2,j+1/2,k)}{\Delta x}\end{array}\right],\qquad(2.22)$$

$$E_z^{n+1}(i,j,k+1/2)=\frac{2\varepsilon(i,j,k+1/2)-\Delta t\sigma(i,j,k+1/2)}{2\varepsilon(i,j,k+1/2)+\Delta t\sigma(i,j,k+1/2)}E_z^n(i,j,k+1/2)+$$
$$\frac{2\Delta t}{2\varepsilon(i,j,k+1/2)+\Delta t\sigma(i,j,k+1/2)}$$
$$\left[\begin{array}{l}\dfrac{H_y^{n+\frac{1}{2}}(i+1/2,j,k+1/2)-H_y^{n+\frac{1}{2}}(i-1/2,j,k+1/2)}{\Delta x}\\ -\dfrac{H_x^{n+\frac{1}{2}}(i,j+1/2,k+1/2)-H_x^{n+\frac{1}{2}}(i,j-1/2,k+1/2)}{\Delta y}\end{array}\right].$$

$$H_x^{n+\frac{1}{2}}(i,j+1/2,k+1/2)=\frac{2\mu(i,j+1/2,k+1/2)-\Delta t\sigma^*(i,j+1/2,k+1/2)}{2\mu(i,j+1/2,k+1/2)+\Delta t\sigma^*(i,j+1/2,k+1/2)}$$
$$H_x^{n-\frac{1}{2}}(i,j+1/2,k+1/2)+$$
$$\frac{2\Delta t}{2\mu(i,j+1/2,k+1/2)+\Delta t\sigma^*(i,j+1/2,k+1/2)}$$
$$\begin{bmatrix}\dfrac{E_y^n(i,j+1/2,k+1)-E_y^n(i,j+1/2,k)}{\Delta z}\\ -\dfrac{E_z^n(i,j+1,k+1/2)-E_z^n(i,j,k+1/2)}{\Delta y}\end{bmatrix},$$

$$H_y^{n+\frac{1}{2}}(i+1/2,j,k+1/2)=\frac{2\mu(i+1/2,j,k+1/2)-\Delta t\sigma^*(i+1/2,j,k+1/2)}{2\mu(i+1/2,j,k+1/2)+\Delta t\sigma^*(i+1/2,j,k+1/2)}$$
$$H_y^{n-\frac{1}{2}}(i+1/2,j,k+1/2)+$$
$$\frac{2\Delta t}{2\mu(i+1/2,j,k+1/2)+\Delta t\sigma^*(i+1/2,j,k+1/2)}$$
$$\begin{bmatrix}\dfrac{E_z^n(i+1,j,k+1/2)-E_z^n(i,j,k+1/2)}{\Delta x}\\ -\dfrac{E_x^n(i+1/2,j,k+1)-E_x^n(i+1/2,j,k)}{\Delta z}\end{bmatrix},$$

(2.23)

$$H_z^{n+\frac{1}{2}}(i+1/2,j+1/2,k)=\frac{2\mu(i+1/2,j+1/2,k)-\Delta t\sigma^*(i+1/2,j+1/2,k)}{2\mu(i+1/2,j+1/2,k)+\Delta t\sigma^*(i+1/2,j+1/2,k)}$$
$$H_z^{n-\frac{1}{2}}(i+1/2,j+1/2,k)+$$
$$\frac{2\Delta t}{2\mu(i+1/2,j+1/2,k)+\Delta t\sigma^*(i+1/2,j+1/2,k)}$$
$$\begin{bmatrix}\dfrac{E_x^n(i+1/2,j+1,k)-E_z^n(i+1/2,j,k)}{\Delta y}\\ -\dfrac{E_x^n(i+1,j+1/2,k)-E_x^n(i,j+1/2,k)}{\Delta x}\end{bmatrix}.$$

One can study PC slabs by 3D FDTD method or the incorporation of the effective index method reduces the problem into two dimensions which save the time and memory requirements.

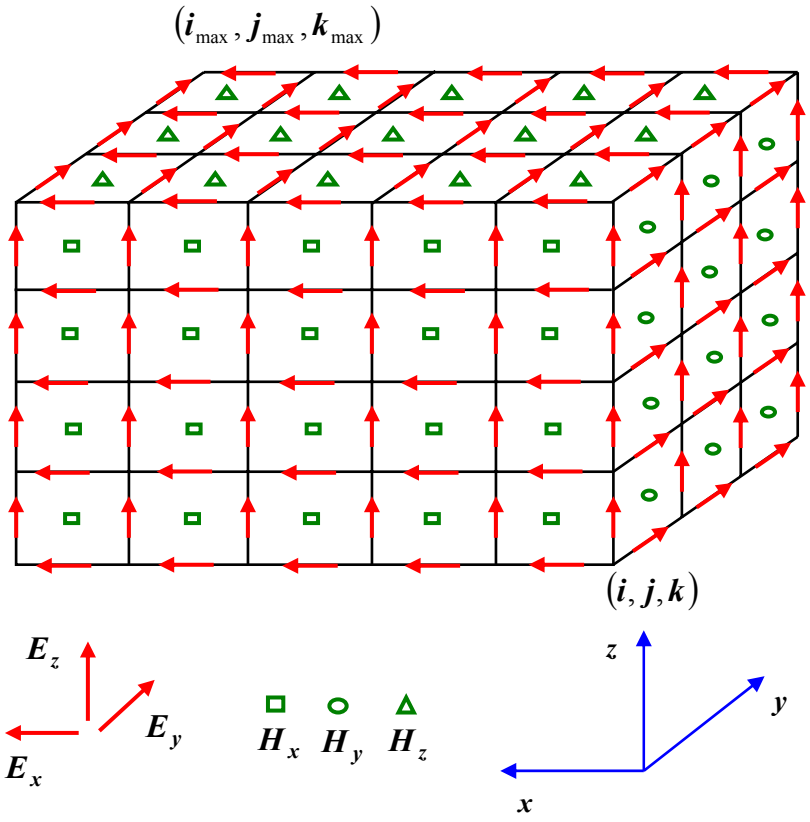

Figure 2.10: Spatial arrangements of field variables in the FDTD for three dimensional case.

The performance (stability and the accuracy) of the finite-difference approximations to Maxwell's differential equations depends on the careful selection of the mesh spacing Δx and time stepping Δt .

$$\Delta t \leq \frac{1}{c\sqrt{\Delta x^{-2} + \Delta y^{-2} + \Delta z^{-2}}}. \tag{2.24}$$

The above condition is known as Courant stability condition and it ensures the causality. This stability criterion ensures the convergence of the numerical simulation. The cell size Δx should sample adequate portion of the minimum wavelength component (worst scenario case) of the EM field. Usually $\Delta x \leq \lambda_{\min}/20$ is safe for enough accuracy but depending on the situation one may increase or reduce the sampling rate. As the pulse propagates down the FDTD mesh, the pulse becomes distorted (broadening and ringing the tail of the pulse) due to the numerical dispersion. Well resolved grid resolution also enables solution which is independent of the angle of the propagation.

2.4 Boundary Conditions

To truncate the computational region boundary conditions are required. They should absorb the out-going EM field by suppressing the spurious back reflected energy regardless of the polarization, propagation direction, and frequency. Absorbing boundary condition (ABC), perfectly matched layer (PML), or periodic boundary condition (PBC) are usually implemented with FDTD. Below I outline briefly the PML and PBC.

2.4.1 Perfectly matched layer (PML) (Split field)

This technique was introduced by J. P. Berenger in 1994 [63]. The computational domain is surrounded by a lossy material that absorbs the unwanted reflections such that the field is decaying exponentially inside the PML region. This method is just a mathematical model with no physical medium. The wave impedance is matched at the boundary

between the computational domain and absorbing layer by splitting the field $H_z = H_{zx} + H_{zy}$ for TE and $E_z = E_{zx} + E_{zy}$ for TM and assuming $\frac{\sigma}{\varepsilon} = \frac{\sigma^*}{\mu}$ where σ and σ^* are the electric and magnetic conductivity, respectively.

In the PML layer, exponential differencing has to be used because the field decays quickly so linear differencing is not adequate. Usually PML is terminated by a PEC layer. There may be a small reflection from this layer but the reflected field travels the PML region towards the computational domain and it is attenuated second time. So if the PML layer thickness is large enough the back reflected field is usually very small in amplitude. The expressions for the boundary layers around the computational domain are

$$\begin{aligned}
\varepsilon \frac{\partial E_x}{\partial t} + \sigma_y E_x &= \frac{\partial H_z}{\partial y} = \frac{\partial \left(H_{zx} + H_{zy} \right)}{\partial y}, \\
\varepsilon \frac{\partial E_y}{\partial t} + \sigma_x E_y &= -\frac{\partial H_z}{\partial x} = -\frac{\partial \left(H_{zx} + H_{zy} \right)}{\partial x}, \\
\mu \frac{\partial H_{zx}}{\partial t} + \sigma_x^* H_{zx} &= -\frac{\partial E_y}{\partial x}, \\
\mu \frac{\partial H_{zy}}{\partial t} + \sigma_y^* H_{zy} &= \frac{\partial E_x}{\partial y}.
\end{aligned} \tag{2.25}$$

The formulation for TM case is similar to the TE one.

2.4.2 PML loss parameters

The conductivity profile is important to increase the absorption performance. One can use the polynomial grading in *x* direction, given by $\sigma_x(x) = \left| \frac{x - x_{\max}}{d} \right|^m \sigma_{x,\max}$, where *m* is the

degree of the polynomial, d is the thickness of the PML, and $\sigma_{x,\max}$ is the maximum conductivity next to the PEC. This way σ is spatially scaled from small values near the PML-computational domain interface to large values near the PEC interface. The reflection coefficient of PML becomes

$$R(\theta) = \exp[-2\eta \cos\theta \int_0^d \sigma_x(x)dx] = \exp[-2\eta\sigma_{x,\max} d \cos\theta/(m+1)]. \quad (2.26)$$

Adjusting the free parameters, $R(\theta)$ can be set to a desired value. Figure 2.11 shows the assignments of the conductivity values around the computational region. The out-going waves generated by the dipole source is absorbed by PML as indicated in Fig. 2.12.

2.4.3 Periodic Boundary condition (PBC)

The Bloch's theorem requires that $E(r+R) = e^{jk\cdot R}E(r)$. The phase shift corresponds to delay in time domain;

$$E(x+X, y+Y, t) = E(x, y, t + mX/\upsilon_{px} + nY/\upsilon_{py}), \quad (2.27)$$

where X and Y are the unit cell dimensions, υ_{px} and υ_{py} are the phase velocities along the x and y axis, respectively and (m,n) are any integers. The PBC implementation in time domain is not straightforward. However, there are ways to implement PBC in FDTD such as $\sin/\cos$ method and split-field technique. The first one does not require field transformation which is direct field method but works for single frequencies. The second method is, on the other hand, requires field transformation.

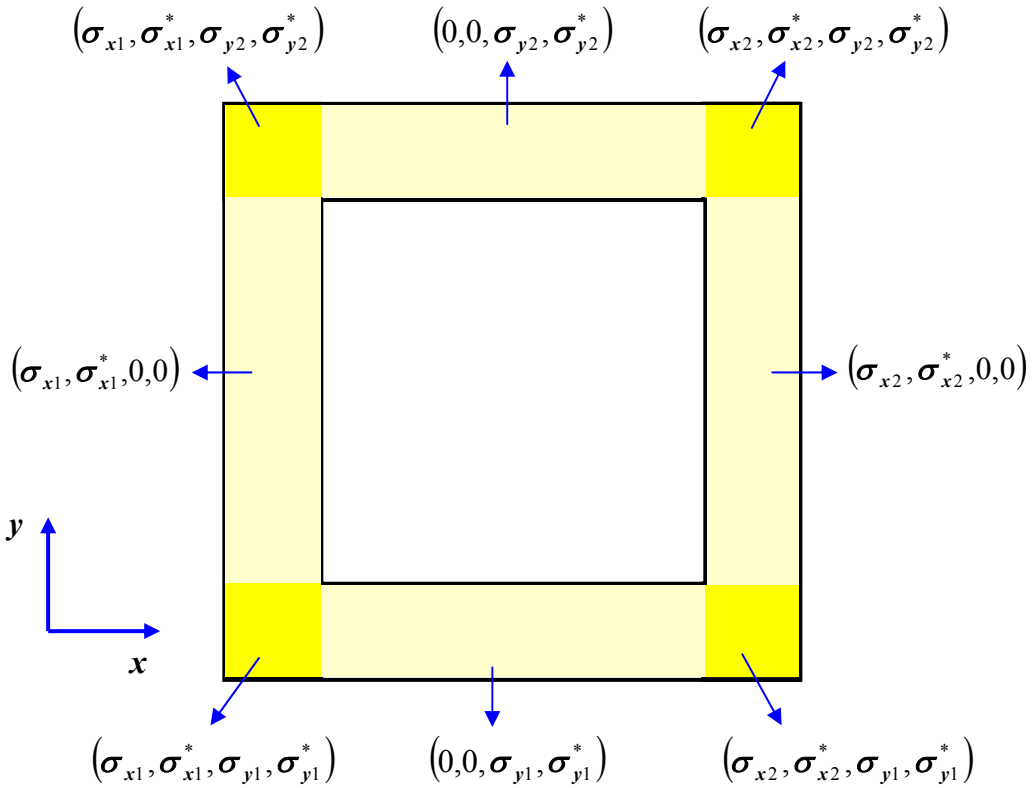

Figure 2.11: Implementing PML ABC for two dimensional FDTD with TE polarization case.

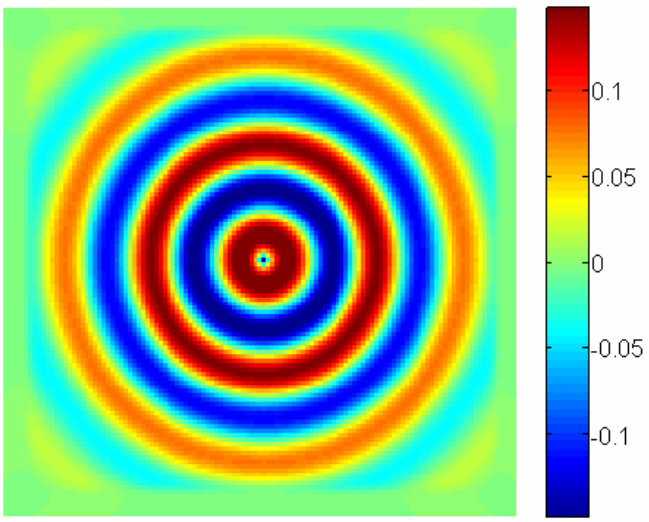

Figure 2.12: Point dipole source radiating in the center of the computational domain surrounded by PML.

2.5 FDTD with Recursive Convolution

Modeling the propagation of EM waves in PCs is feasible by implementing a computational method such as FDTD. In this method, the Maxwell equations are discretized in space and time by central differences using Yee's cell as formulated above. It enables the observation of the temporal and spatial variation of EM waves propagating through the medium. Typically, the medium is assumed to be nondispersive, so the permittivity and permeability are taken constant. However, when there is a material having significant frequency dependence on the constitutive parameters, the usual FDTD method must be modified. One approach is called FDTD with RC [13, 14]. It is based on the recursive evaluation of the convolution between the *D* and *E* fields, which comes from the frequency-dependent dielectric function Fourier transformed to time.

The formulation shown here is mostly adapted from Ref. [14]. The time-dependent Maxwell's curl equations in a source-free medium are

$$\begin{aligned} \nabla \times E &= -\frac{\partial B}{\partial t}, \\ \nabla \times H &= \frac{\partial D}{\partial t}, \\ \nabla . D &= 0, \\ \nabla . B &= 0. \end{aligned} \tag{2.28}$$

assuming zero conductivity $\sigma = 0$, and constant permeability $B = \mu_0 H$.

The spatial and time discretizations of Maxwell's equations for the TE mode can be written as follows

$$\frac{\partial D_x}{\partial t} = \frac{\partial H_z}{\partial y},$$

$$\frac{\partial D_y}{\partial t} = -\frac{\partial H_z}{\partial x}, \tag{2.29}$$

$$\frac{\partial H_z}{\partial t} = \frac{1}{\mu}\left[\frac{\partial E_x}{\partial y} - \frac{\partial E_y}{\partial x}\right].$$

The central-difference expressions for the space and time derivatives are

$$\frac{D_x^{n+1}(i,j) - D_x^n(i,j)}{\Delta t} = \frac{H_z^{n+1/2}\left(i, j+\frac{1}{2}\right) - H_z^{n-1/2}\left(i, j-\frac{1}{2}\right)}{\Delta y},$$

$$\frac{D_y^{n+1}(i,j) - D_y^n(i,j)}{\Delta t} = -\frac{H_z^{n+1/2}\left(i+\frac{1}{2}, j\right) - H_z^{n-1/2}\left(i-\frac{1}{2}, j\right)}{\Delta x}, \tag{2.30}$$

$$\frac{H_z^{n+1/2}\left(i+\frac{1}{2}, j+\frac{1}{2}\right)}{\Delta t} = \frac{1}{\mu}\left[\left(\frac{E_x^n(i,j+1) - E_x^n(i,j)}{\Delta y}\right) - \left(\frac{E_y^n(i+1,j) - E_y^n(i,j)}{\Delta x}\right)\right].$$

In general, the electric flux density is related to the electric field by $D = \varepsilon_0 \varepsilon_r E$. For a linear dispersive medium $\varepsilon_r(\omega) = \varepsilon_\infty + \chi(\omega)$ and then

$$D_y(\omega) = \varepsilon_\circ \varepsilon_r(\omega) E_y(\omega) = \varepsilon_\circ[\varepsilon_\infty + \chi(\omega)] E_y(\omega). \tag{2.31}$$

Since multiplication in the frequency domain corresponds to a convolution in the time domain: $D_y(t) = \varepsilon_\infty \varepsilon_\circ E_y(t) + \varepsilon_\circ \int_0^t E_y(t-\tau)\chi(\tau)d\tau$ where $\chi(t)$ is the time domain electric

susceptibility function, ε_0 is permittivity of free space, and ε_∞ is the infinite frequency relative permittivity.

When we write the above equation in discrete form using Yee's notation, we obtain

$$D_y(t) \cong D_y(n\Delta t) = D_y{}^n = \varepsilon_\infty \varepsilon_\circ E_y{}^n + \varepsilon_\circ \int_0^{n\Delta t} E_y(n\Delta t - \tau)\chi(\tau)d\tau, \tag{2.32}$$

assuming all field quantities are constant over each time interval Δt, then the integration can be written as follows

$$D_y{}^n(i,j) = \varepsilon_\circ \varepsilon_\infty E_y{}^n(i,j) + \varepsilon_\circ \sum_{m=0}^{n-1} E_y{}^{n-m}(i,j) \int_{m\Delta t}^{(m+1)\Delta t} \chi(\tau)d\tau. \tag{2.33}$$

At the next time step

$$D_y{}^{n+1}(i,j) = \varepsilon_\circ \varepsilon_\infty E_y{}^{n+1}(i,j) + \varepsilon_\circ \sum_{m=0}^{n} E_y{}^{n+1-m}(i,j) \int_{m\Delta t}^{(m+1)\Delta t} \chi(\tau)d\tau. \tag{2.34}$$

From equations (2.32) and (2.33) the central-difference expression for the time derivative is obtained as

$$\begin{aligned} D_y^{n+1}(i,j) - D_y^n(i,j) &= \varepsilon_\circ \varepsilon_\infty \left[E_y^{n+1}(i,j) - E_y^n(i,j)\right] \\ &+ \varepsilon_\circ E_y^{n+1}(i,j)\chi^\circ + \varepsilon_\circ \sum_{m=0}^{n-1} E_y^{n-m}(i,j)\left(\chi^{m+1} - \chi^m\right), \end{aligned} \tag{2.35}$$

where

$$\chi^m = \int_{m\Delta t}^{(m+1)\Delta t} \chi(\tau)d\tau.$$

To simplify the equation (2.34), one can also define

$$\Delta\chi^m = \chi^m - \chi^{m+1},$$

Then

$$D_y^{n+1}(i,j) - D_y^n(i,j) = \left(\varepsilon_\circ \varepsilon_\infty + \varepsilon_0 \chi^\circ\right) E_y^{n+1}(i,j) - \varepsilon_\circ \varepsilon_\infty E_y^n(i,j) - \varepsilon_\circ \sum_{m=0}^{n-1} E_y^{n-m}(i,j) \Delta\chi^m . \tag{2.36}$$

When we solve the equation (2.35) for E_y^{n+1} we find

$$E_y^{n+1}(i,j) = \frac{\varepsilon_\infty(i,j)}{\varepsilon_\infty(i,j) + \chi^\circ(i,j)} E_y^n(i,j) + \frac{1}{\varepsilon_\infty(i,j) + \chi^\circ(i,j)} \sum_{m=0}^{n-1} E_y^{n-m}(i,j) \Delta\chi^m(i,j) - \frac{\Delta t}{\left(\varepsilon_\infty(i,j) + \chi^\circ(i,j)\right)\varepsilon_\circ \Delta x} \left[H_z^{n+1/2}(i+1/2, j) - H_z^{n+1/2}(i-1/2, j) \right]. \tag{2.37}$$

In the above expression (2.36), the summation term is computationally heavy to implement directly. However, when $\chi(t)$ has an exponential time behavior, the convolution summation can be replaced by a recursive form. In this study, we take second order Lorentz form to model the dispersion

$$\varepsilon(\omega) = \varepsilon_\infty + (\varepsilon_s - \varepsilon_\infty) \frac{\omega_0^2}{\omega_0^2 + j2\delta\omega - \omega^2}, \tag{2.38}$$

where ε_s is the static permittivity, ω_0 is the resonant frequency, and δ is the damping coefficient. The following Fourier-Transform pair is useful to obtain the time domain susceptibility function for Lorentz form

$$\chi(t) = \gamma e^{-\alpha t} \sin(\beta t) u(t) \Leftrightarrow \frac{\gamma\beta}{\left(\alpha^2 + \beta^2 + j2\alpha\omega - \omega^2\right)}, \tag{2.39}$$

where $u(t)$ is the time step function, $\alpha = \delta$, $\beta = \sqrt{\omega^2 - \delta^2}$, and $\gamma = \dfrac{(\varepsilon_s - \varepsilon_\infty)\omega^2}{\beta}$.

The goal is to express the time domain susceptibility function in an exponential form and then update the summation term recursively. Therefore, we need to define complex time domain susceptibility function

$$\hat{\chi}(t) = -j\gamma e^{(-\alpha + j\beta)t} u(t), \tag{2.40}$$

so that $\chi(t) = \mathrm{Re}[\hat{\chi}(t)]$.

Since $\chi^m = \int_{m\Delta t}^{(m+1)\Delta t} \chi(\tau) d\tau$, and $\Delta\chi^m = \chi^m - \chi^{m+1}$,

$$\hat{\chi}^m = \frac{-j\gamma}{\alpha - j\beta} e^{(-\alpha + j\beta)m\Delta t}\left[1 - e^{(-\alpha + j\beta)\Delta t}\right], \tag{2.41}$$

and

$$\Delta\hat{\chi}^m = \hat{\chi}^m - \hat{\chi}^{m+1} = \frac{-j\gamma}{\alpha - j\beta} e^{(-\alpha + j\beta)m\Delta t}\left[1 - e^{(-\alpha + j\beta)\Delta t}\right]^2, \tag{2.42}$$

$$\Delta\hat{\chi}^{m+1} = e^{(-\alpha + j\beta)\Delta t}\Delta\hat{\chi}^m. \tag{2.43}$$

Let's write the summation term in the following form

$$\sum_{m=0}^{n-1} E_y^{n-m}(i,j)\Delta\chi^m(i,j) = \psi_y^n(i,j) = \mathrm{Re}\left(\hat{\psi}_y^n(i,j)\right). \tag{2.44}$$

When we write the first two terms, we obtain for $n = 1$

$$\psi_y^1(i,j) = E_y^1(i,j)\Delta\chi^\circ(i,j),$$

and for $n = 2$,

$$\psi_y^2(i,j) = E_y^2(i,j)\Delta\chi^0(i,j) + E_y^1(i,j)\Delta\chi^1(i,j) =$$
$$E_y^2(i,j)\Delta\chi^0(i,j) + E_y^1(i,j)e^{(-\alpha+j\beta)\Delta t}\Delta\chi^0(i,j) =$$
$$E_y^2(i,j)\Delta\chi^0(i,j) + e^{(-\alpha+j\beta)\Delta t}\psi_y^1(i,j),$$

from which it follows that

$$\hat{\psi}^n = E^n\Delta\hat{\chi}^\circ + e^{(-\alpha+j\beta)\Delta t}\hat{\psi}^{n-1}, \tag{2.45}$$

$$\psi^n = \mathrm{Re}\left[\hat{\psi}^n\right] = \sum_{m=0}^{n-1} E^{n-m}\Delta\chi^m. \tag{2.46}$$

The final forms are:

$$E_y^{n+1}(i,j) = \frac{\varepsilon_\infty(i,j)}{\varepsilon_\infty(i,j)+\chi^0(i,j)}E_y^n(i,j) + \frac{1}{\varepsilon_\infty(i,j)+\chi^0(i,j)}\psi_y^n(i,j) -$$
$$\frac{\Delta t}{\left[\varepsilon_\infty(i,j)+\chi^0(i,j)\right]\varepsilon_0\Delta x}\left[H_z^{n+1/2}(i,j) - H_z^{n+1/2}(i,j-1)\right],$$

$$E_x^{n+1}(i,j) = \frac{\varepsilon_\infty(i,j)}{\varepsilon_\infty(i,j)+\chi^0(i,j)}E_x^n(i,j) + \frac{1}{\varepsilon_\infty(i,j)+\chi^0(i,j)}\psi_x^n(i,j) +$$
$$\frac{\Delta t}{\left[\varepsilon_\infty(i,j)+\chi^0(i,j)\right]\varepsilon_0\Delta y}\left[H_z^{n+1/2}(i,j) - H_z^{n+1/2}(i-1,j)\right], \tag{2.47}$$

$$H_z^{n+1/2}(i,j) = H_z^{n-1/2}(i,j) + \frac{\Delta t}{\mu}\left[\frac{E_x^n(i+1,j)-E_x^n(i,j)}{\Delta x} - \frac{E_y^n(i,j+1)-E_y^n(i,j)}{\Delta y}\right].$$

where

$$\hat{\chi}^0 = \frac{-j\gamma}{\alpha - j\beta}\left[1 - e^{(-\alpha + j\beta)\Delta t}\right]$$

$$\chi^0 = \mathrm{Re}\left(\hat{\chi}^0\right)$$

$$\Delta\hat{\chi}^0 = \frac{-j\gamma}{\alpha - j\beta}\left[1 - e^{(-\alpha + j\beta)\Delta t}\right]^2$$

$$\Delta\chi^0 = \mathrm{Re}\left[\Delta\hat{\chi}^0\right].$$

These are the general expression and can be reduced to the usual FDTD equations when ε_∞ equals to ε_s. Following similar steps, one can formulate for the TM case easily too. To validate the above formulation of FDTD-RC, a test case is studied.

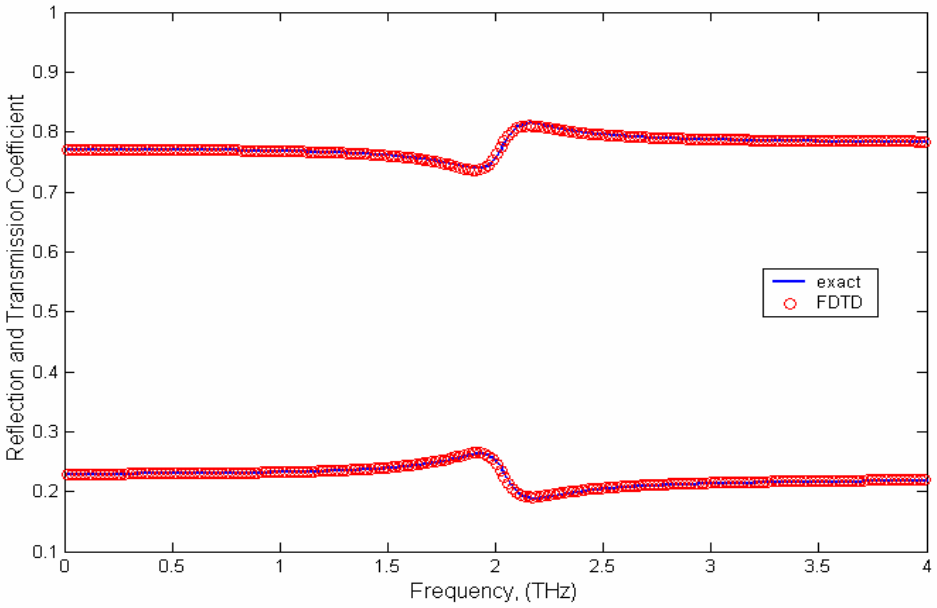

Figure 2.13: Numerical comparison of the transmission and reflection coefficient for an air-dispersive medium interface.

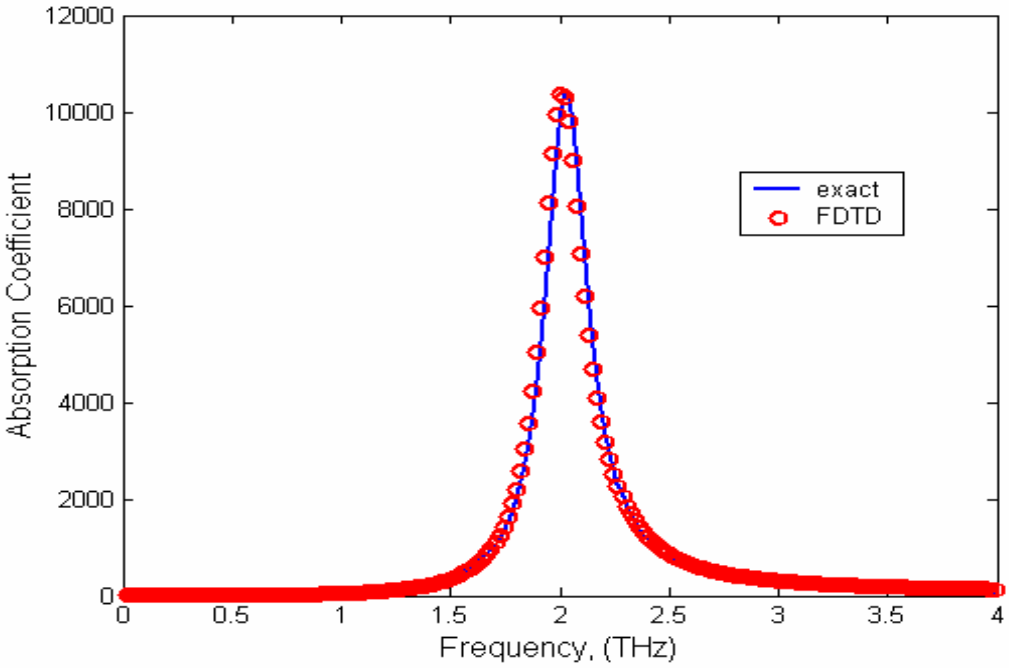

Figure 2.14: Numerical and analytical comparison of the absorption parameter of the second medium.

Transmission/reflection coefficients at air-dispersive medium interface and absorption parameter of the medium obtained by FDTD-RC are compared with the analytical results. They are shown in Figs. 2.13 and 14. The good agreement between the exact solution and the numerical method shows the validity of the above implementation.

CHAPTER III

Photonic crystals for biochemical sensing in the terahertz region*

3.1 Introduction

Photonic crystals (PCs) have numerous potential applications in optics to implement both active and passive devices as well as linear and nonlinear devices. Recently, PCs have attracted attention for chemical and biological sensing. The main attraction of such structures for this application is the ability to tailor the material-electromagnetic interaction. References 50 and 52 have recently proposed the use of PCs for chemical/fluid detection. In Ref. 52 multi-channel PCWs are designed such that the input is guided by a PC line defect and coupled to one of the channels if the fluid is inserted into the air holes of the same channel. Reference 50 used high-quality microcavities for chemical detection. The resonant frequency of the cavity is very sensitive to changes in the refractive index and geometry. Therefore, filling the defect hole with various samples alters the resonant frequencies.

In this Chapter, the frequency region of interest is the far-infrared in contrast to near-infrared or visible region in which most of the spectroscopic applications of PCs have been investigated. Due to the scalability of Maxwell's equations, the analysis of PC in one frequency range can be shifted to another frequency region by

*This chapter is based on: Hamza Kurt and D. S. Citrin, "Photonic crystals for biochemical sensing in the terahertz region," *Appl. Phys. Lett.* **87**, 41108 (1-3) (2005).

scaling the size of the PC. At near-infrared or visible wavelengths, however, it is difficult to manufacture PC structures; the richness of terahertz region in the spectroscopy of small and large molecules in gas and liquid phase together with the ease of fabrication for applications in this wavelength range make PCs attractive for biological and chemical sensing.

The use of terahertz region for biological and chemical sensing has largely been neglected due to the relative lack of sources and detectors even though large biomolecules may have fingerprints (vibrational and rotational modes) in this region of the spectrum. The frequency interval of the EM spectrum approximately from 0.1 to 20 THz is called the THz or far-infrared (FIR) region of the EM spectrum. Historically, accessing the scientifically rich, but technologically limited, THz range was hindered by the difficulty of generating and detecting THz radiation; recent advances in THz sources and detectors have led to renewed interest in the interaction of THz energy with matter for unique spectroscopy and imaging applications. Solid-state oscillators, quantum-cascade lasers, free-electron-based sources, and laser-driven THz emitters have recently been used for the production of FIR radiation, providing a means to close the so-called THz gap (Figure 3.1).

THz time-domain spectroscopy (THz-TDS), based on the generation of broadband EM transients from biased photoconductors excited by ultrafast laser pulses, is a versatile tool to provide absorption spectra of biological molecules [65, 66]. The dispersion and absorption of the sample material modifies the E-field of the THz signal as it propagates through a sample in the beam path. One can identify the presence or absence of specific materials including gases and biomolecules such as deoxyribonucleic acid (DNA) by inspecting the absorption signature.

THz-TDS is commonly used to investigate these modes of many biological materials and they have significant frequency dependence to their index of refraction in the terahertz regime [67-69]. It has been shown that an integrated terahertz microstrip line resonator sensitive to the loaded sample is capable of identifying and quantifying the hybridization state of the polynucleotides using the dependency of the binding state of the deoxyribonucleic acid (DNA) sequences to their refractive index [69]. Compared to the free-space measurements a detection sensitivity of femtomole levels was achieved reducing the required amount of DNA molecules by a factor of $>10^{-3}$.

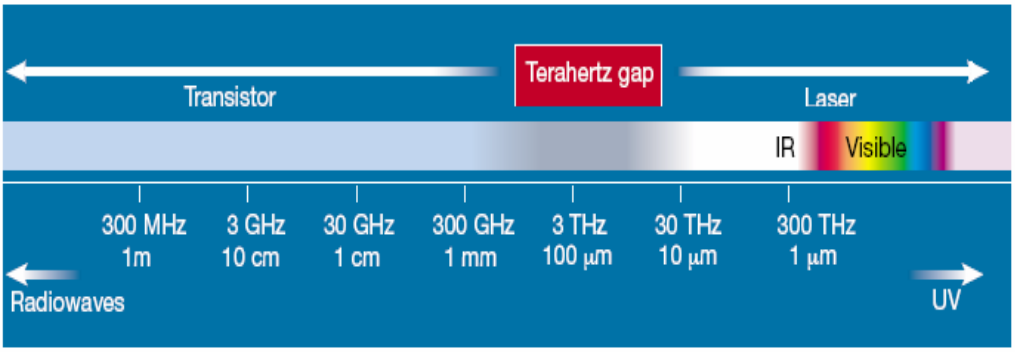

Figure 3.1: Electromagnetic spectrum. The terahertz gap is the regime between microwave and infrared region [64].

3.2 Photonic crystal waveguide sensors

A schematic diagram of the deployment of a PC-based sensor is shown in Fig. 3.2. A liquid or gaseous sample flows through the holes of a two-dimensional PC waveguide (PCW) while the propagation of a THz beam through a PCW is monitored for sample-induced changes. Due to the nature of light propagation through a PCW, the EM field of the THz radiation is confined to selected rows of holes, thus ensuring maximum interaction of the THz beam with the small quantity of sample contained in those

holes. Below, we cite computed figures of merit (FOM), which indicate that the sensors we envisage may out perform bulk gas-cell sensors and fiber sensors.

The dispersive effect of DNA molecules in PCs is investigated by using finite-difference time-domain (FDTD) method with the recursive convolution (RC) approach [13, 14] considering the frequency dependence of the electromagnetic response of biological samples. The PC studied has a triangular array of holes in a GaAs dielectric background. We assume that the dielectric background is nonabsorbing, and has constant index of refraction $n = 3.46$. The radius of the air holes is $r = 0.4a$, where a is the lattice periodicity. Figure 3.3 shows the dispersion diagram of the PC obtained by plane-wave expansion method. This structure possesses a wide PBG for TE polarization (electric field parallel to the plane) at $0.2452 < a/\lambda < 0.4022$ as shown in Fig. 3.3. If we take the lattice constant $a = 60\,\mu$m, then a band gap opens between $f_L = 1.226$ THz and $f_H = 2.011$ THz.

The transmission coefficient (spectrum) of the PCW is obtained from the FDTD-RC simulations as follows. First a Gaussian pulse with broad bandwidth is launched and the propagated field is recorded at the exit of the structure either at the presence of sample or absence of it in the waveguide region. Then, the same input is propagated through the dielectric medium without the structure and stored at the input. At the end these two recorded signals are Fourier transformed and the ratio of their squared moduli gives the transmission coefficient. The computational domain is terminated by perfectly matched layer boundary condition [63]. Each unit cell is divided into 30x30 grid points.

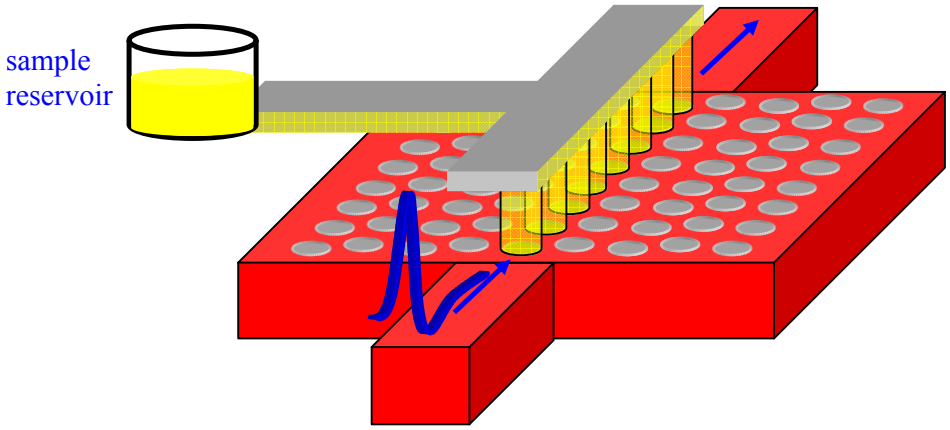

Figure 3.2: Schematic representation of photonic crystal waveguide sensor with sample delivery mechanism.

A simple way of making a PCW is to remove the air holes within a single row. However, in our case we need to keep the air holes in the waveguide to inject the analyte. Therefore, the PCW is obtained by increasing or reducing the radius of the air holes to $0.45a$ (PCW-A) and $0.3a$ (PCW-B), respectively, thereby permitting a propagating mode inside the PBG. The insets in Figs. 4(a) and 4(b) show the schematics of the waveguides. It is important to have a propagating mode in the PCW that has very high transmission and low group velocity. The spectroscopic change in the transmission spectrum with the sample inserted into the air holes in the line defect is monitored to ascertain the effect of the electromagnetic-matter interaction. The guided propagating signal interacts with the dispersion and absorption of the PC structure containing the biological material, which provides the sensing mechanism.

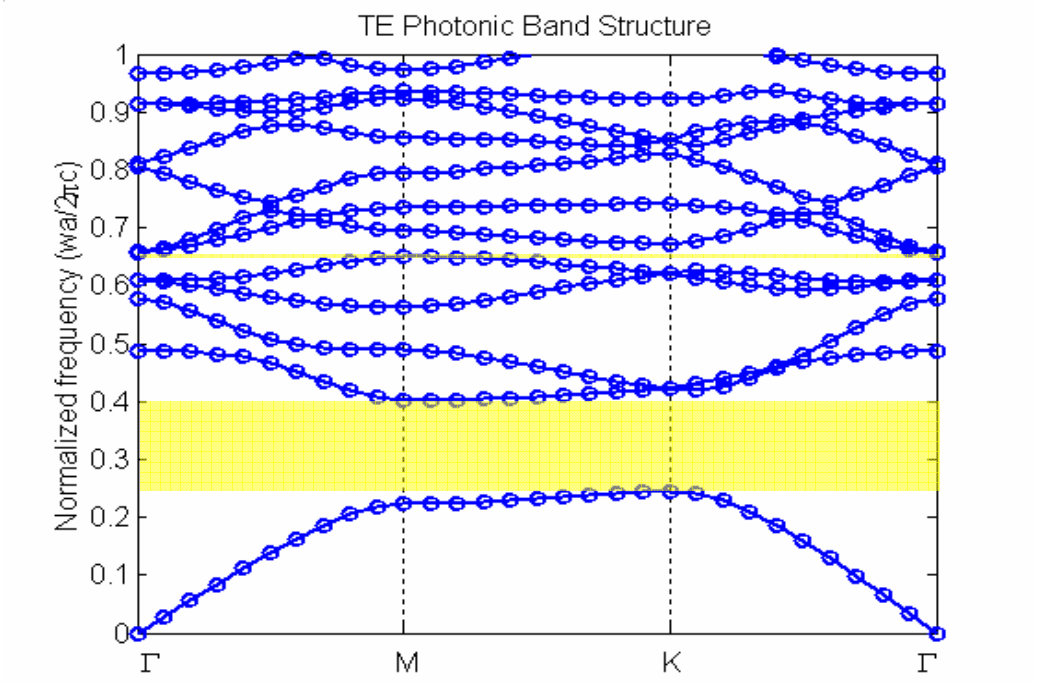

Figure 3.3: The photonic band diagram for the TE modes (E_x, E_y, H_z) of a triangular array of air holes (columns) with $r/a = 0.4$ in a dielectric background $(\varepsilon = 12)$. There is a complete PBG (shaded region) between the first and the second band at $0.2452 < a/\lambda < 0.4022$.

The effective path length over which the terahertz pulse interacts with the biological material should be very long. This can be achieved if the terahertz wave has low group velocity. Moreover the field amplitude and profile is also important. It is desired that the electric field maxima are confined inside the holes where the biological materials is placed. PCs can provide all these features with judicious design.

The recent study of Fischer shows that building blocks of DNA, adenine, guanine, cytosine, and thymine have absorption resonances in the terahertz region [66]. These resonances can be approximated by a Lorentz model. The complex dielectric permittivity of the dispersive DNA can be expressed in Lorentz form as

$$\varepsilon(\omega) = \varepsilon_r + i\varepsilon_i = \varepsilon_\infty + (\varepsilon_s - \varepsilon_\infty)\frac{\omega_0^2}{\omega_0^2 + i2\omega\delta - \omega^2}. \quad (3.1)$$

where ε_r and ε_i are the real and imaginary parts, respectively, ε_∞ is the high-frequency permittivity, ε_s is the static permittivity, ω_0 is the resonant frequency, and δ is the damping coefficient. In our study, the analysis is carried out for a single Lorentz resonance, but it can be increased to many resonances as required. As an example to show the applicability and the advantages of PCWs for biochemical sensing, we took the following values from Ref. 58 for the dispersive behavior of the DNA: $\varepsilon_\infty = 2.45$, $\varepsilon_s = 2.544$, $\omega_0/(2\pi) = 1.9$ THz for PCW-A and $\omega_0/(2\pi) = 1.6$ THz for PCW-B, $\delta = 0.06\omega_0$. However, the applicability of the PCW sensor studied here should not be restricted in application to this specific test case. Finally, we note that in general, in bulk systems the absorption coefficient [58] α (m^{-1}) is related to the imaginary part of the refractive index n_i as

$$\alpha = \frac{4\pi}{\lambda} n_i = \frac{4\pi}{\lambda}\left[\frac{|\varepsilon(\omega)| - \varepsilon_r}{2}\right]^{1/2}. \quad (3.2)$$

3.3 Results and discussions

A comparison of two transmission spectra shown in Figs. 3.4(a) and 4(b) with and without DNA within the air holes (line defect region) of the PCW-A and B shows that the signal is attenuated when it interacts with the DNA sample. Adding dielectric material by means of sample loading brings modes from air band down to band gap. Propagating modes pulled down from the air band provides the confinement of the field in low index medium enabling direct field-sample interaction. In PCW-B, two cases, reducing air hole radius and adding dielectric, have a parallel effect so there is

good propagation mode well inside the PBG away from the air band. However, increasing the size of the air holes and adding dielectric material have the opposite effect in PCW-A hence modes are shallow close to the air band. The decrease in the transmission at ~1.9 and 1.6 THz due to the presence of the absorbing molecules can be clearly seen. Even though similar changes in the transmission spectrum were observed with reduced air-hole PCW-B structure, PCW-A type of structures are desirable for practical reasons due to the larger air holes, and the consequent ease of loading the sample. Since the PCW is very sensitive to index changes, we considered the mean value of the Lorentz index profile of the analyte. As the sample is loaded, the mean index of the filled air holes has to be taken into account to calculate the transmission spectrum. We assumed uniform loading of sample throughout the air holes of the waveguide channel. Sample handling in the terahertz region is of special importance due to the strong absorption lines of water. In practice, an aqueous solution of the analyte can be delivered by injection, by free-fluid flow, or by integrated microfluidic channels onto the holes, and evaporation and desiccation carried out subsequently to exclude terahertz absorption due to water. However, one notes that quite rapid evaporation may be possible due to the extremely small analyte amount delivered to the 36 to 54 μm diameter holes depending on the depth of the sensor structure. Depending on the analyte, one may employ a gaseous carrier or a liquid carrier or solvent that is not strongly absorbing in the frequency window of interest.

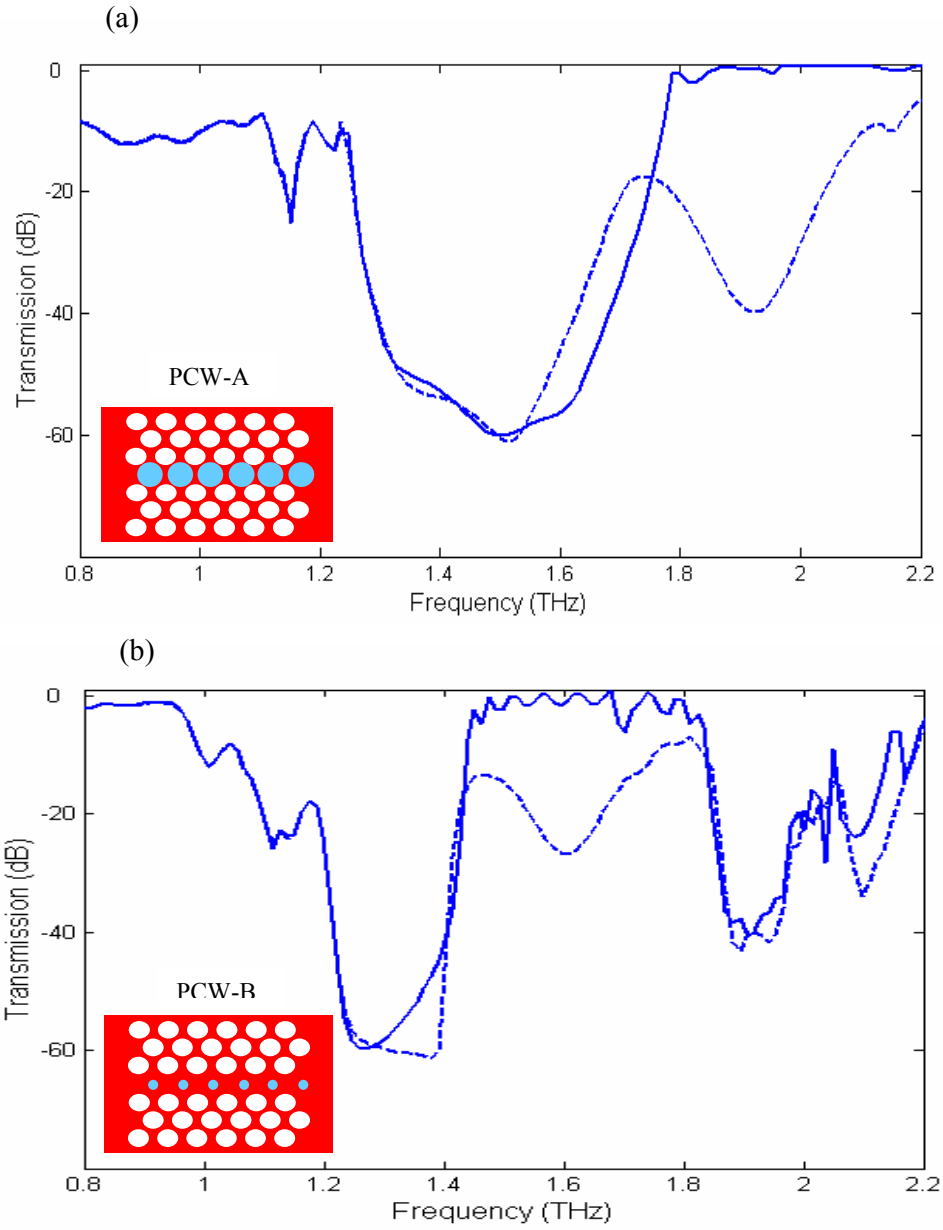

Figure 3.4: Transmission spectrum of the photonic crystal in the ΓK direction for TE polarization; (a) Photonic crystal waveguide (PCW-A) with (solid line) and without (dashed line) absorption at 1.9 THz. The inset is the schematic diagram of the waveguide. The defect radius is $0.45a$. (b) Photonic crystal waveguide (PCW-B) with (solid line) and without (dashed line) absorption at 1.6 THz. The inset is the schematic diagram of the waveguide. The defect radius is $0.3a$.

In order to explore the *intrinsic* enhancement of PCW sensor performance compared with bulk gas cells, we carefully eliminate the effects of the PCW ends, including in- and out-coupling. This is important since, while various in- and out-coupling strategies may be envisaged, the intrinsic attenuation provides a fundamental limit to performance. By carrying out simulations for sets of sufficiently long structures, one verifies numerically that the guided signal is exponentially attenuated by the sample, and thus the attenuation can be attributed exclusively to the absorption in the waveguide region. Figure 5(a) shows the single-frequency variation (1.9 THz) through the line-defect PCW-A. When there is no sample in the air holes, the signal while confining in the low index medium propagates through the PCW-A without loss; the inserted sample material attenuates the signal and the attenuation is exponential. Due to the less absorptive material and low value of absorption coefficient of PCW-B at 1.6 THz, attenuation is not as much as PCW-A case as is shown in Fig. 5(b).

To benchmark the PCW, say versus a bulk gas cell, for sensor applications, it is necessary to define the appropriate figure of merit. The propagation of the electric field in bulk E_{bulk} and the PCW E_{PC} can be formulated as

$$E_{\text{in,bulk}} e^{-\alpha_{\text{bulk}} z_1} = E_{\text{out,bulk}}, \tag{3.3}$$

$$E_{\text{in,PC}} e^{-\alpha_{\text{PC}} z_2} = E_{\text{out,PC}}, \tag{3.4}$$

where z_1 and z_2 measure the propagation distance within the gas cell or PCW. Note, for the PCW sensor, we define the locations of the input and output sufficiently far

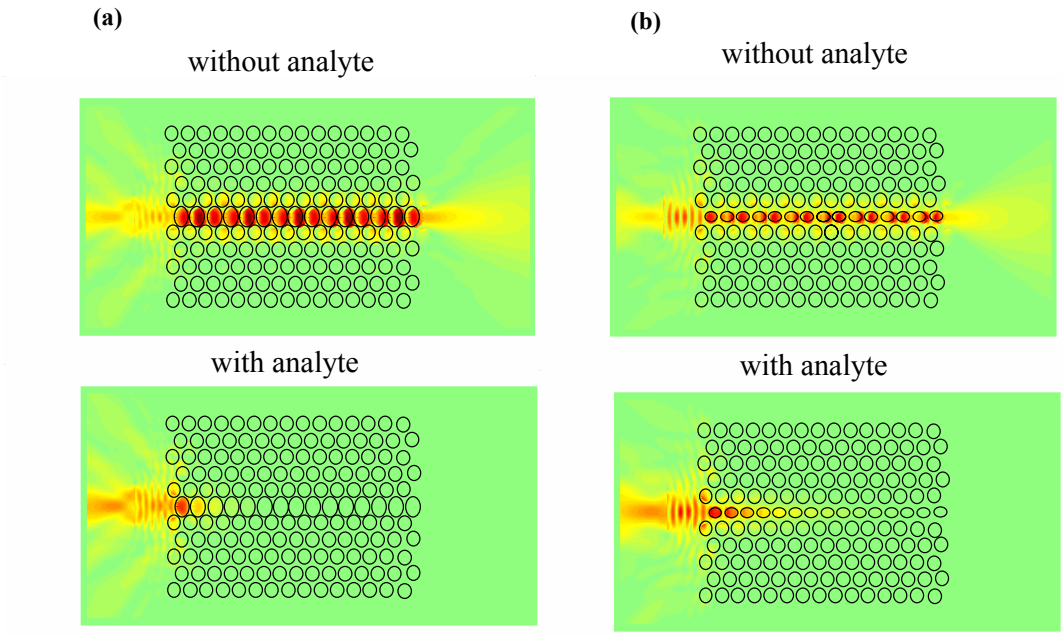

Figure 3.5: Two types of photonic crystal waveguides (a) PCW-A (b) PCW-B with and without analyte in the guiding region. (a) Steady-state resonant frequency, $\omega_0/(2\pi) = 1.9$ THz, transmission in the PCW-A structure with and without analyte. (b) Steady-state resonant frequency, $\omega_0/(2\pi) = 1.6$ THz, transmission in the PCW-B structure with and without analyte.

from the waveguide ends to ensure that the attenuation measured is exponential and independent of the in- or out-coupling. We defined the enhancement factor *M* as a measure of the change of attenuation induced by the PCW compared with bulk:

$$\alpha_{\mathrm{PC}} = \mathrm{M}(\Gamma\alpha_{\mathrm{bulk}}), \tag{3.5}$$

where Γ is the optical confinement factor measuring the degree of the concentration of the energy in sensing areas (i.e. holes). The final form of *M* is

$$M = \frac{z_1 \ln\left(E_{\text{out,PC}} / E_{\text{in,PC}}\right)}{\Gamma z_2 \ln\left(E_{\text{out,bulk}} / E_{\text{in,bulk}}\right)}. \tag{3.6}$$

For $M = 1$, the two systems have the same performance, while $M > 1$ means the PCWs have better performance. We need to make it clear that even for $M = 1$ for which the two systems have same performance, the PCW still has the obvious advantage of compactness.

In order to ascertain the degree to which the effects presented above might be useful for sensing applications, we compared our structures PCW-A and PCW-B with a bulk DNA system of the same concentrations in two different cases. In one case, all have the same length; in other, the comparison is made by the required amount of dispersive material (i.e., DNA). M value is obtained for PCW-A with 11 holes and ω_0 is changed from 2.0 THz to 1.8 THz. Similarly, PCW-B has 13 holes and ω_0 is changed from 1.75 THz to 1.45 THz. For both cases, corresponding bulk lengths of $330\Delta x$ and $210\Delta x$, where $\Delta x = 2 \times 10^{-6}$ μm are taken. It is important to specify that the M calculation is independent of the length as long as the sensor is in the linear region. As shown in Fig. 3.6, M increases greatly near the PBG at which the group velocity is low and the interaction time is longer. This performance correlates with the electric-field enhancement in the air holes in the vicinity of the air band. This enhancement increases the sensitivity of the proposed sensor. The amount of material is reduced by more than five orders of magnitude assuming that a free space approach uses 1cmx1cm size cuvette and PCW-B has 7 sensing holes which are enough to carry the measurement. As a result additional sensitivity is achieved.

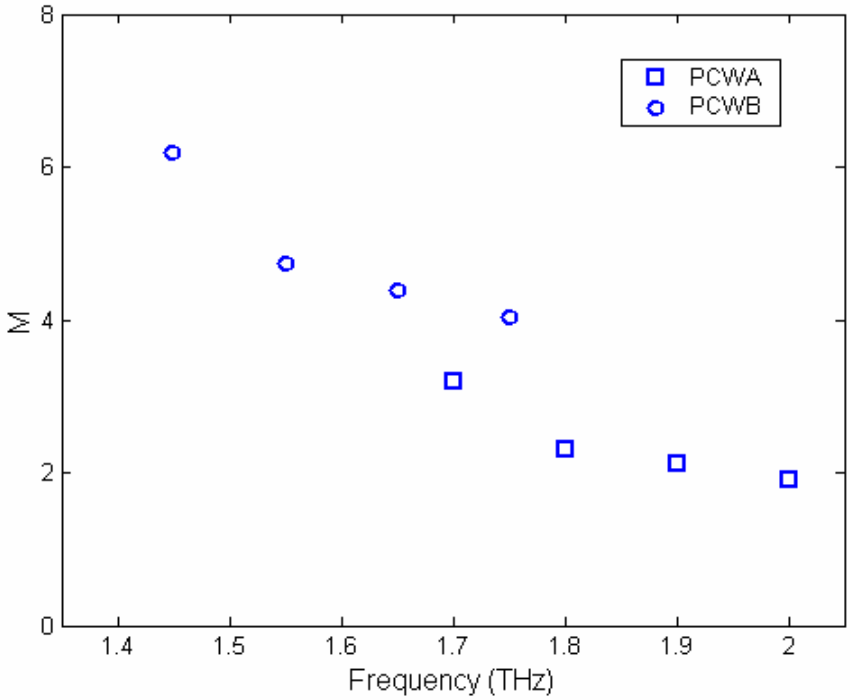

Figure 3.6: The enhancement factor M near the photonic band gap (PBG) for PCW-A and PCW-B for the same length case. PCW-A and B have 11 and 13 holes respectively corresponding to the lengths of $330\Delta x$ and $210\Delta x$ for bulk structure, where $\Delta x = 2\times10^{-6}\,\mu$m.

3.4 Photonic crystal waveguide sensors in the microwave regime

The working principles of PCW sensors explained above can be tested in any section of the EM spectrum. The selection of the microwave region is mainly due to the fact that it is relatively easy to fabricate PCs and perform the experiments at these frequencies as the unit lattice is around a few millimeters. In this regard, we collaborate with Prof. Martin Koch at the Technical University of Braunschweig to perform the experiment. Figure 3.7 shows the image of a prototype triangular lattice PC perforated on a high-density polyethylene (HDPE) which provides band gap at around 100 GHz with $n = 1.57$ and $r = 0.26a$. The initial stages of experiment include the investigation of transmission spectrum of different organic solvents loaded to

PCW. These liquids are refractive indices of $n = 1.422$ (cyclohexane), $n = 1.51$ (CCl4), and $n = 1.507$ (benzene).

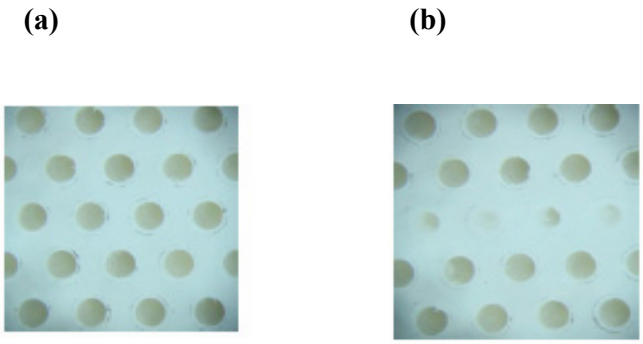

Figure 3.7: The pictures of fabricated PC and PCW. The hole radius is $r = 0.26a$ and the defect radius is $r = 0.19a$. The background has refractive index of $n = 1.57$.

The experimental results are obtained by the set up shown in Fig. 3.8. The TE polarized light is incident to PC and the transmitted field is detected by the receiver.

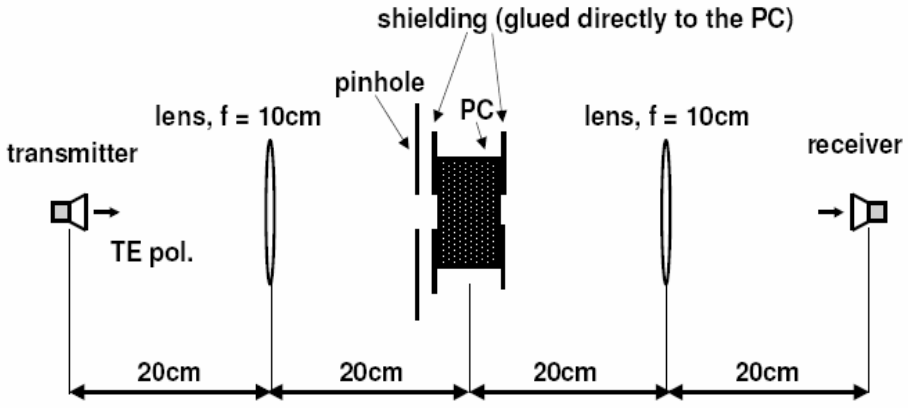

Figure 3.8: The experimental set up used for the study of PC sensors in the microwave region.

The experimental results are indicated in Fig. 3.9 along with the smoothed data obtained by extracting the Fabry-Perot oscillations. They are compared with the theoretical results as plotted in Fig. 3.10. Figure 3.10 shows the transmission plots of three cases: PC, PCW and PCW filled with cyclohexane ($n = 1.422$). The unperturbed structure provides band gap around 100 GHz. The PCW is obtained by reducing the radius of holes to $r = 0.18a$ which means increasing the effective index of the waveguide region. The transmission spectrum of the PCW indicates that the air band moves to lower frequencies while the dielectric band stays relatively unchanged. Infiltrating the holes in the waveguide region with cyclohexane increases the effective index further; hence, similar variation for the air band is observed. In addition, one can see that, the minimum peaks of the transmission spectra experience red shift as the waveguide is created and loaded with sample (cyclohexane).

3.5 Conclusions

Based on our detailed simulations in addition to the preliminary experimental results, PCWs for bio-sensing applications are found to be promising. Low group velocity and localization of light in these structures result in enhanced terahertz absorption by DNA molecules (the specific example treated in this study) within the low refractive index medium. Compared with the free space (bulk) approach, device size can be reduced dramatically, less sample material is needed, and an integrated system can be made with PCs; hence, different molecules could be analyzed simultaneously. Sensors based on terahertz PCWs can sample small absolute quantities of materials that can nevertheless flow through the sensor in real time, and thus such sensors may be integrated into industrial processes.

(a)

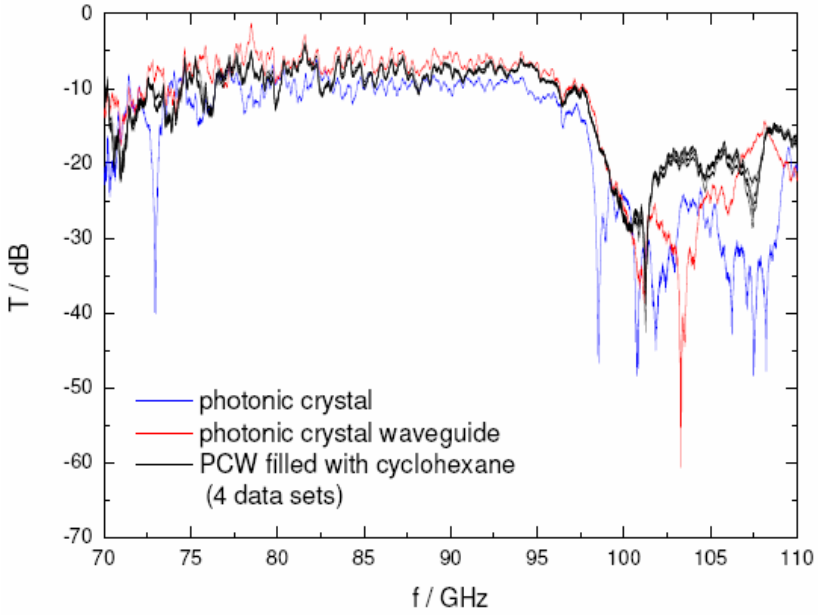

(b)

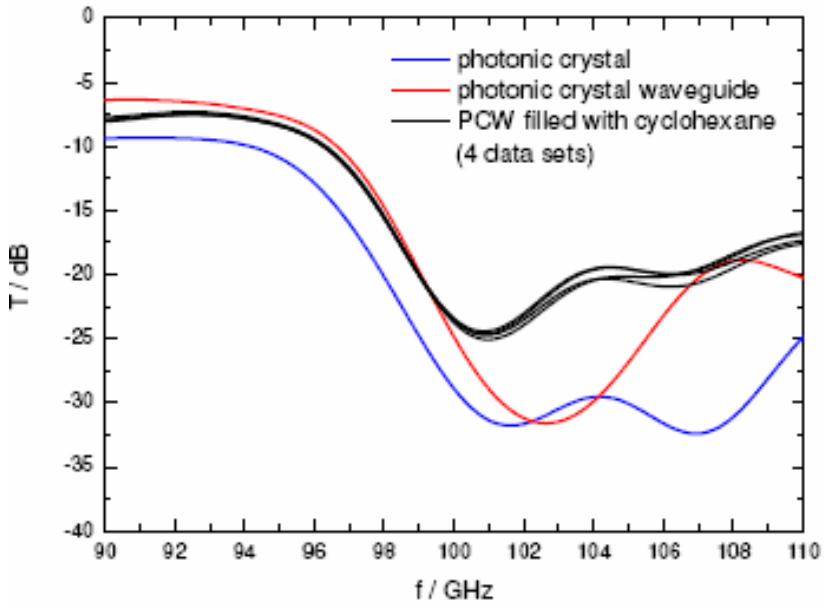

Figure 3.9: The transmission spectra of (a) PC and (b) PCW. The waveguide section is also infiltrated by cyclohexane.

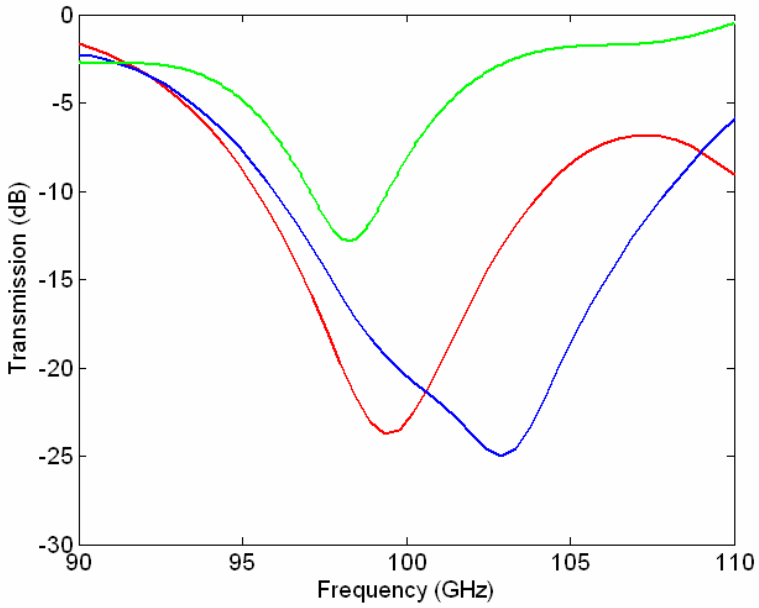

Figure 3.10: Transmission spectra of PC, PCW and PCW filled with cyclohexane.

Moreover, in the terahertz regime, it is relatively easy to manufacture these structures. One notes, however, that due to the scalability of Maxwell's equations, the designed structure can be used in any frequency region. The relatively small scale of the device with low sample volumes in addition to the integration of such sensors into arrays may enable microfluidic devices, also called "lab-on-a-chip," that are promising analytical tools for analyzing liquids and biomolecules.

CHAPTER IV

Coupled-resonator optical waveguides for biochemical sensing of nanoliter volumes of analyte in the terahertz region*

4.1 Introduction

Depending on the targeted area from environmental monitoring to biomedical applications the constraints on a biochemical sensor will be different. However, sensitivity, efficiency, miniaturizability, low latency, manufacturability, and cost-effectiveness are usually commonly desired features. There are varieties of recently proposed biochemical sensors utilizing different configurations. For example, photonic crystal (PC) fiber (holey fibers) sensors based on the use of evanescent wave are the subject of considerable current research [70, 71]. The electric field in such structures is confined in the core region that is enclosed by air holes in which the sample is inserted. The field-matter interaction occurs in the air holes. In general, the sensitivity of the evanescent-field sensor is very low because exponentially decaying electromagnetic field penetrating to the sensing region is low. To increase the sensitivity one can use longer PC fibers, but then different issues have to be addressed such as increased sample quantities, greater latency, and the uniformly diffusion of the sample through the air holes. Another example is called hollow-core antiresonant reflecting optical waveguides (ARROW) [72].

*This chapter is based on: Hamza Kurt, D. S. Citrin, "Coupled-resonator optical waveguides for biochemical sensing of nanoliter volumes of analyte in the terahertz region," Appl. Phys. Lett. **87**, 241119 (1-3) (2005).

The hollow core is surrounded by high reflective Fabry-Perot mirrors and can be filled with liquids both to confine light and sense the analyte. Since light interacts only once as it propagates down the core, the sensitivity of this design is also low.

A number of these difficulties are potentially addressed by sensors based on PC cavities [50, 51] and PC waveguides (PCW) [73]. In Chapter III, PCW structures were proposed for biochemical sensing in the terahertz region. The spectroscopic change in the transmission spectrum with the sample inserted into the air holes in the line defect is monitored to ascertain the effect of the direct electromagnetic-matter interaction rather than the evanescent field-matter interaction as in holey fibers. The guided propagating signal interacts with the dispersion and absorption of the PC containing the biological material, which provides the sensing mechanism. The long effective pathlength over which the terahertz pulse interacts with the biological material was ensured without increasing the actual structure size by making sure that the propagating mode in the band gap has low group velocity. Moreover the field was confined largely within the holes where the biological material is placed.

4.2 Coupled-resonator optical waveguide sensors

Recently, a new type of PCW called coupled-resonator optical-waveguide (CROW) has been introduced [74]. The waveguiding is based on tightly confining electromagnetic waves in each cavity and weakly coupling the cavities to their neighbors by the evanescent field of the resonator modes outside the cavity. Using the tight-binding (TB) approximation, it was shown that the phase and group velocity strongly depend on the coupling parameter κ_1 which is controlled by cavity properties and intercavity distance

[75]. Similar to the PCW, the group velocity of the propagating mode can be very low in CROW. On the other hand, CROW's have very sharp resonant propagating modes, which lead to enhanced field confinement compared with PCW's in which the modes are close to the band edge and confinement is poor. In this Letter, we present the potential applications of CROW devices as biochemical sensor due to aforementioned properties.

We can briefly summarize our biochemical sensor design goals as follows. The first is to provide the interaction of the field with the target where the field is near its maximum, instead of via the evanescent part of the wave. In other words, the electric-field maxima should be confined inside the holes where the biological material is loaded. This enhances the sensitivity. Second, we aim to increase the effective interaction length without making the structure larger. The advantages are twofold. Miniaturization is vital especially for integrated structures, and the ability to sense small quantities of analyte is of paramount importance for many biomedical applications. Finally, it is important to note that the selection of terahertz region of the electromagnetic spectrum brings the richness of the spectral features of many molecules with the ease of fabrication of PC based devices as well as the potential for realtime flow of fluids through the sensor for low-latency operation.

4.3 Results and discussions

Below, the dispersive effect of the DNA molecules in CROW's is investigated by using finite-difference time-domain (FDTD) method with the recursive convolution approach [13, 14]. The computational domain is terminated by a perfectly matched layer (PML) [63]. Each unit cell (*axa*) is divided into 30 x 30 grid points. CROW's are formed in

two-dimensional photonic crystal dielectric slabs with a triangular array of air holes in a GaAs dielectric background. We assume that this dielectric background is nonabsorbing within the frequency range of interest, and has constant index of refraction $n = 3.46$. The radius of the holes is, $r = 0.4a$ where a is the lattice periodicity and the schematic diagram is shown as an inset in Fig. 4.1(c). We use *N* and *K* to describe the number of air holes between each cavity and the number of cavities respectively. For example in Figs. 4.1(a) and 4.1(b) $N = 2$ and $K = 5$. Cavities are created either increasing or reducing the radius of the air holes to $r = 0.45a$ and $r = 0.3a$, respectively, and they are represented by CROW-A and B. The defect free photonic crystal contains a band gap at $0.3504 < a/\lambda < 0.4176$ as shown in Fig. 4.1(c). To model the dispersive medium (analyte) within the sites comprising the defect waveguide, we used the same parameters as in Chapter III and uniform sample distribution is assumed. A common method of sample preparation is to mix DNA with water and evaporate the solution ending with DNA films. Due to the strong water absorption in the far infrared region, one needs to eliminate its influence to be able to extract the absorption characteristics of analyte in an optimal fashion. In general, the sensor response should ideally be independent of the sample preparation. An aqueous solution of DNA sample may be delivered by injection, by free-fluid flow, or by integrated microfluidic channels onto the holes, and evaporation and desiccation carried out subsequently to exclude terahertz absorption due to water. However, this may end up with a nonuniform sample distribution.

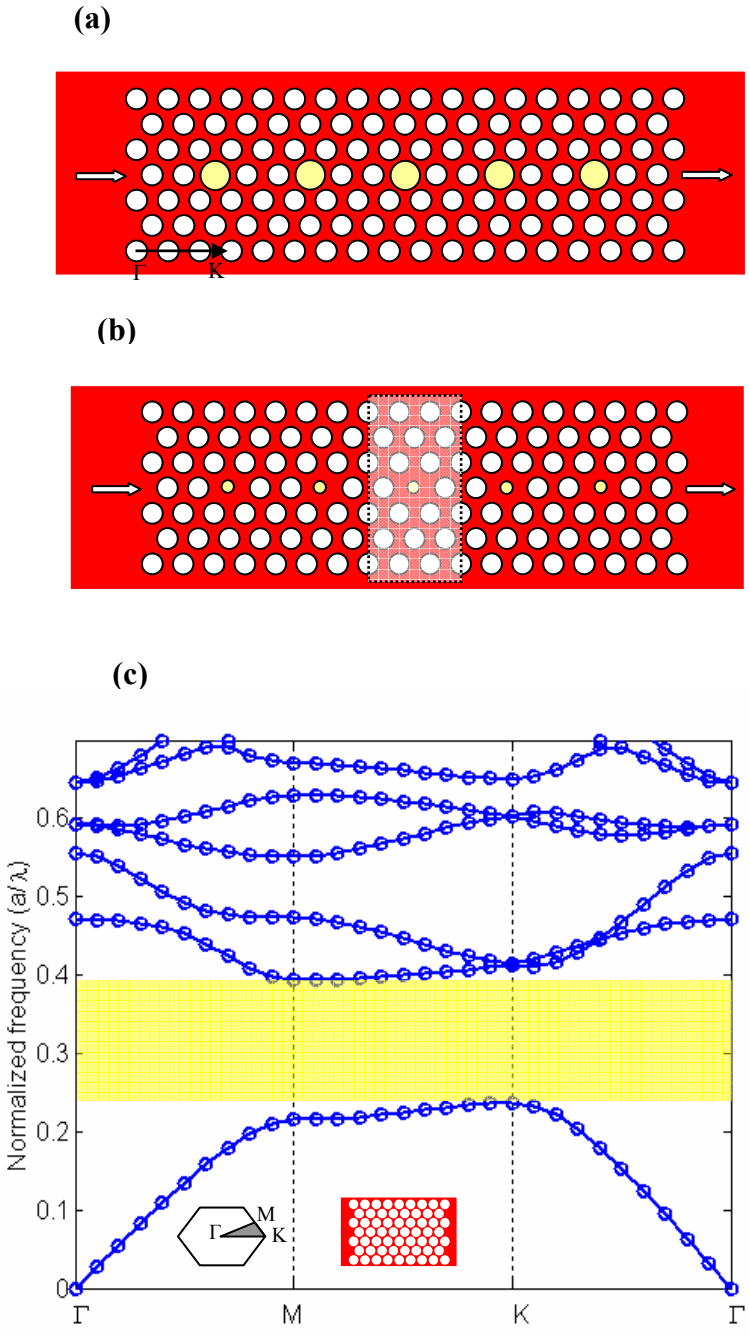

Figure 4.1: (a) Schematic diagram of the coupled-resonator optical waveguide (CROW) with increased air holes $r_{def} = 0.45a$ (CROW-A). There are 5 defect cavities (K=5) and the number of holes between each cavity is 2 (N=2). (b) Schematic diagram of the coupled-resonator optical waveguide with the reduced air holes $r_{def} = 0.3a$ (CROW-B). N and K are the same as in (a). A supercell is highlighted. (c) Dispersion diagram of the unperturbed triangular array photonic crystal for TE polarization.

One can study the non-uniform sample loading effect on the sensor response, but another way is to enable a loading process such that the sample distribution is uniform. For example, the filler can be obtained by mixing DNA with non-polar liquids which are transparent and not strongly absorbing in the terahertz region. This way the uniform sample distribution can be achieved. Another way of sample loading that may enable uniform distribution is the immobilization of the biomolecule on the surfaces of the microchannels by covalently biding of the antibodies [76]. The DNA example was a case study so any biomolecules that have frequency dependent refractive index within the frequency region of interest can also be studied.

Table 4.1 shows the different configurations studied here. In fact, $N = 0$ means successive cavities occupy consecutive periods of the PC structure, resulting in the standard PCW. The resonant modes of CROW's are well inside the gap; hence, it is anticipated that the confinement of the electric field will be strong [77]. The CROW structure can be interpreted as a chain of moderate Q cavities, the number of holes between each cavity determining the quality factor. The electric field enhancement is proportional to Q. In effect, for a λ-cavity, Q gives the number of times the electric field bounces around within the cavity before escaping. It can be seen; moreover, from Fig. 4.2 that electric field has large amplitude in defect sites with matching field maxima within the cavity where analyte is loaded.

TABLE 4.1: Design parameters of the coupled-resonator optical-waveguide operating in the terahertz region. The lattice periodicity is denoted by a and $a = 60$ μm. Two types of defect radius were used $r_{def} = 0.3a$ and $r_{def} = 0.45a$. N and K describe the number of air holes between each cavity and the number of cavities respectively.

N	K	r_{def}
1	7	$0.3a, 0.45a$
2	5	$0.3a, 0.45a$
3	3	$0.3a, 0.45a$

It is important to note that as N increases group velocity defined as $\partial\omega/\partial k$ decreases. N has important effect to the overall transmission amplitude and also coupling of input light to the CROW. Increasing N reduces the transmitted light and also makes the coupling to the waveguide difficult; however, larger N means weak coupling between each cavity hence lower group velocity. On the other hand, reducing N can increase the coupling factor and group velocity. Thus, the judicious selection of N is important to ensure simultaneous low group velocity and high transmission. Also, as N increases the resonant mode is confined inside the band gap and separated well from the band gap edge.

In order to compare the operation of the CROW sensor with either free-space cells or PCW's, it is essential to define the appropriate figure of merit. We defined the enhancement factor M (the details can be in previous chapter) as a measure of the change of attenuation induced by the CROW compared with bulk:

$$M = \frac{z_1 \ln\left(E_{\text{out,CROW}} / E_{\text{in,CROW}}\right)}{\Gamma z_2 \ln\left(E_{\text{out,bulk}} / E_{\text{in,bulk}}\right)}, \tag{4.1}$$

where Γ is the optical confinement factor measuring the degree of the concentration of the energy in sensing areas (i.e. holes), z_1 and z_2 measure the propagation distance within the gas cell or CROW. In short, when M = 1, the two systems have the same performance, while $M > 1$ means the CROW's have better performance. Figure 4.3 shows how M changes as N is increased. There is large improvement in the enhancement when N increases from 1 to 2, and even though the improvement in sensitivity continues to increase from $N = 2$ to 3, the increase is not substantial. Therefore $N = 2$ can be selected considering a compact sensor structure. Also increasing $N > 3$ may reduce the group velocity and increase the sensitivity of the sensor but transmission amplitude at the output of the sensor will be small due to the difficulty in input coupling so that the detection will be difficult. Another observation from Fig. 4.3 is that although CROW-A and B exhibit similar trends in their enhancement parameter, CROW-B has better performance than A because of the superior confinement of the field modes; however, structures of the type of CROW-A may be desirable for practical reasons due to the larger air holes, and the consequent relative ease of loading the sample.

The other crucial parameter is the number K of cavities that comprise the CROW. The transmitted field shows exponential dependence on the length of the CROW. Longer waveguides, however, may increase the response time which may not be desired especially for real-time sensing. Also, sensor size is of paramount importance for integrated devices. Another issue in some applications is the ability to sense small quantities of material. Therefore selection an optimum value of K is important.

(a)

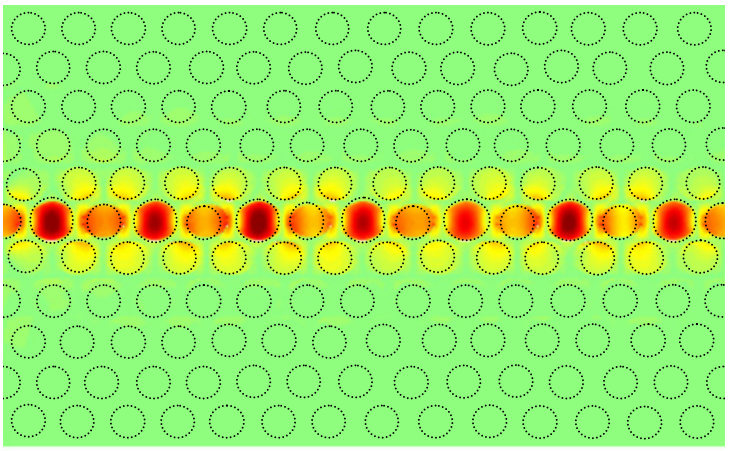

(b)

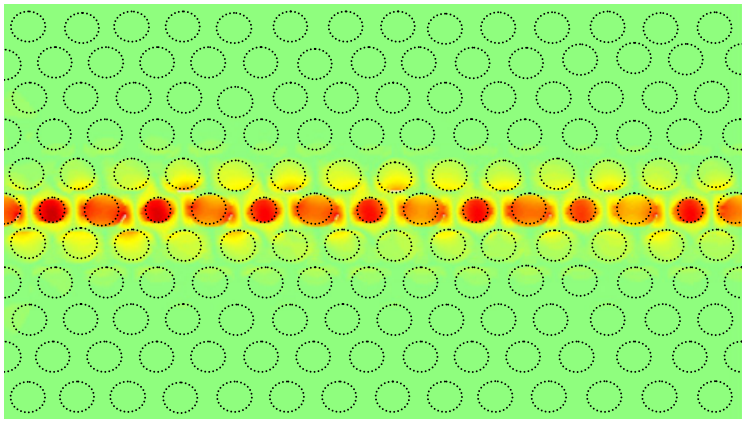

Figure 4.2: (a) Steady-state electric field variation for CROW-A and (b) similarly for CROW-B with *N* (number of air holes between each cavity) equals to 1.

Figures 4.4(a) and 4.4(b) show the variation of resonant frequency when refractive index of the analyte changes from $n = 1.414$ to $n = 1.581$. The spectral peak experiences red-shift for both CROW-A and B as the refractive index increases. The shift in CROW-A, however, is more than two times larger than in B, as can be seen in Fig. 4.4(c). One sees a linear relation between the frequency and the refractive index. As the refractive index increases the propagating mode moves away from the air band. A refractive index change of $\Delta n = 0.033$ corresponds to a wavelength shift of $\Delta\lambda = 1.17$ μm. It is also interesting to note that since both CROW-A and B have propagating mode pulled down from air band they show similar variation to the refractive index change. Depending on the way the cavity is obtained the defect modes can be created either from air band (adding dielectric) or from dielectric band (removing dielectric).

The absorptive medium greatly changes the spectral shape of the resonant mode both in amplitude and width for on and off-resonance cases. Amplitude and width increase as the center frequency of the Lorentz medium moves away from that of the resonant mode. As a result the quality factor of the resonant mode is modified. As the absorption peak of the analyte and the resonant mode of the waveguide overlap the change in the transmission spectrum is large compared to the off-resonant case. As a result this is a more sensitive detection regime.

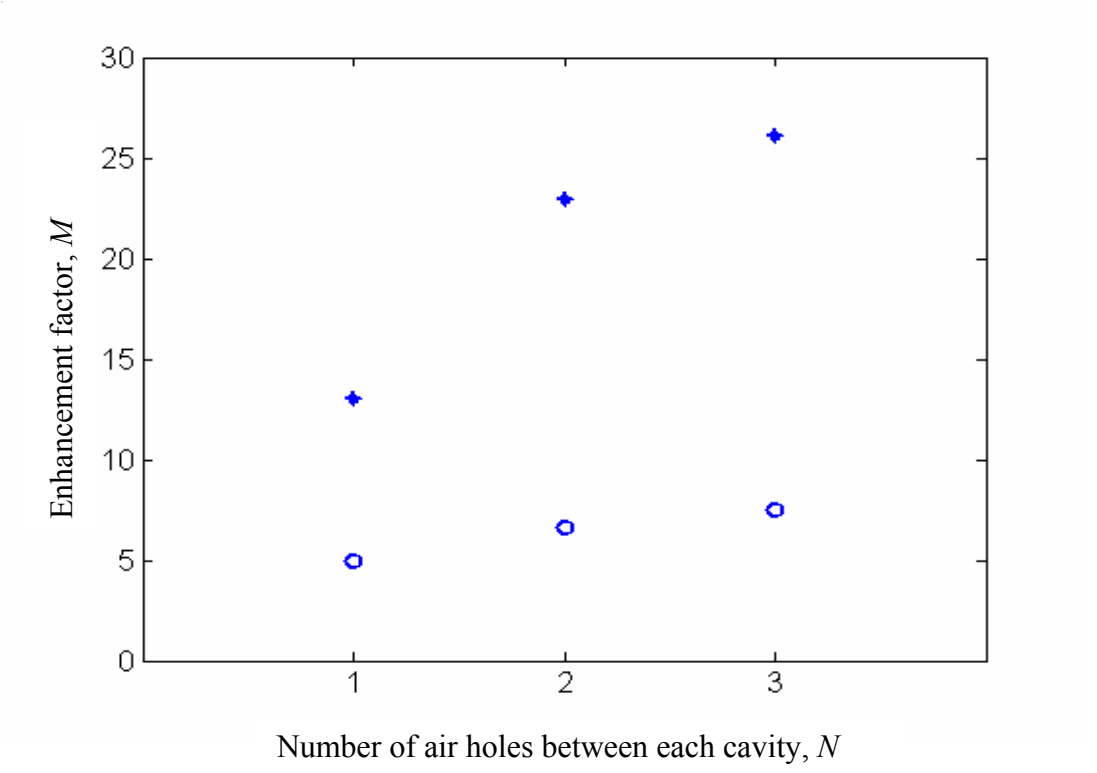

Figure 4.3: The intercavity distance *N versus* enhancement parameter *M* for CROW-A (circle) and B (plus).

4.4 Conclusions

In conclusion, after carrying out detailed simulations we have shown that very high sensitive biochemical sensors can be designed by selecting appropriately the CROW parameters (defect radius, number of cavities, and inter-cavity distance) in the terahertz region. If the sample has weak absorbance then CROW-B type of structure is favorable due to high M factor. On the other hand CROW-A is more sensitive simply because of more material used. The sensor is extremely sensitive to the changes in the absorption of the nanoliter volume samples. We have shown that the enhancement, *M*, of CROW-based sensors may be much higher than bulk structure and PCWs. We have demonstrated that the propagating mode of the CROW is very sensitive to the concentration of the sample

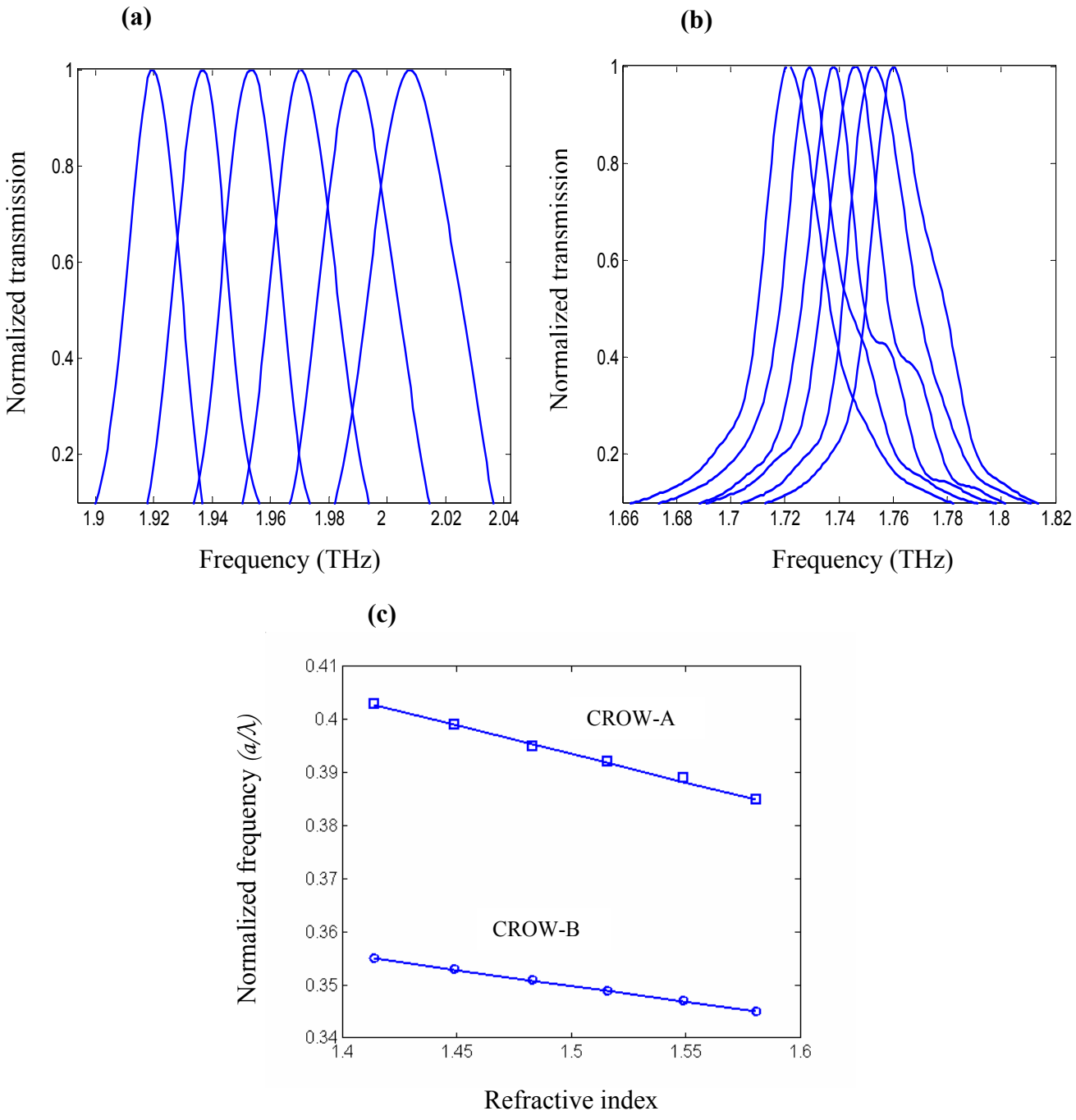

Figure 4.4: (a) Resonant frequency shift of CROW-A for six different cases. (n=1.414 to n =1.581) (b) similarly for CROW-B. (c) Normalized frequency variation for the same refractive indexes.

(DNA) and resonant shift is linearly dependent on the concentration of the bio-molecule. A 2% change in concentration gives rise to approximately 2.4% change in the transmission spectrum. We have attributed the better enhancement and sensitivity of the proposed sensor to the low group velocity hence longer field-matter interaction, and the strong confinement of the field maxima in the low index medium where the analyte is loaded. Even though the selected sample was DNA molecule in our study one should note that this sensing mechanism can potentially be used to other bio-molecules and detection of gases as well as liquids are additional possible applications for CROW-based sensor. Integration of such sensors with microfluidics may enable high-throughput, real-time terahertz sensors. The idea proposed in this work can be applied directly to the mid-IR too.

CHAPTER V

Annular photonic crystals*

5.1 Introduction

Since the first proposal of multidimensional artificially periodic dielectric structures known as photonic crystals [1, 2] (PC), tremendous progress has been made towards the realization of the main property of PCs, *viz*. the photonic band gap (PBG), which has enabled applications throughout the electromagnetic spectrum [3, 78]. The PBG is a range of frequencies where the modes are evanescent and thus not allowed to propagate irrespective of the propagation direction and polarization type. Even though one can obtain the full benefit of the PC in three-dimensional structures, the challenge of manufacturing submicron-scale three-dimensional PCs at visible to near-infrared wavelengths has directed research efforts towards more easily fabricated two-dimensional PCs. The implementations of PCs include photonic band-edge lasers, highly reflective mirrors, superprisms, high-Q microcavities, low-threshold lasers, all-optical switches, optical transistors, and optical logic gates [15-32, 38-45, 79]. PBGs have been used to improve the gain and the far-field patterns of patch antennae in the microwave region [46, 47]. Other applications in this region include high-impedance surfaces, compact uniplanar slow-wave lines, and broad-band filters [48, 49, 80, 81].

*This chapter is based on: Hamza Kurt and D. S. Citrin, "Annular photonic crystals," Opt. Express, **13**, 10316-10326, (2005).

There are some concerns related to making PC's more functional and practical for deployment in real devices, even for the two-dimensional case. In particular, there are serious difficulties obtaining a wide PBG, for *all* polarizations, using simple, though widely used, geometries. For example, for many applications, one requires polarization-insensitive devices. We directly addresses this problem by exploring a relatively simple geometry that is surprisingly effective in enabling the independent control of the PC properties associated with different polarizations. Namely, we consider a PC structure that combines desirable properties of two widely exploited slightly simpler geometries to attain this control. We also show that in some cases, the PBG can exceed the PBG's expected from the two PC geometries that motivate our design.

Specifically, square and triangular arrays of circular air holes in a dielectric background and that of circular dielectric rods in an air background are the most commonly found PCs in the literature. The former (air holes) provides an absolute PBG near close-packed conditions. The latter (rods) usually does not provide a complete PBG, but there are ways as mentioned below to obtain a PBG even in this case. To have a PBG and to increase its size for all polarizations, to obtain polarization independent PBGs, or to engineer only TE or TM band gaps are all important aims. Employing an anisotropic material, reducing the structure symmetry, inclusion of metallic components, structural deformation, and composite structures are among the approaches to engineer the PBG that have been explored, and in these cases the PBG can be enhanced [82-87]. Each of these approaches, however, faces different problems. For example, metals are very lossy especially in the optical region. Therefore, very small metallic inclusions have been proposed. Structural deformation raises manufacturing concerns as the pattern of the

lattice becomes complex. It is difficult to find strongly anisotropic materials. We are aware of no simple rules that can be drawn upon, such as which symmetry breaking structure gives larger PBG by lifting the degeneracies at the high symmetry points. The reduction of the symmetry typically also enlarges the high-order PBGs while reducing the lowest-order PBG. Finally, if a larger PBG is achieved at very close-packed conditions, then fabrication of the PC will be challenging due to the resulting very thin veins.

5.2 The structure

It is well known that a PC of isolated high-dielectric regions tends to support TM band gaps, whereas a connected lattice typically provides TE band gaps. One can illustrate this by referring to gap map for the specific type of PCs (square- and triangular-lattice dielectric rods in air and square- and triangular-lattice holes in dielectric background) [3]. The idea is to have a lattice that leverages off the strengths of both isolated and connected regions. As a result, there may be complete PBG.

The structure we consider was motivated by the desire to control independently, to the maximum extent possible, the size and the location of the TE and the TM band gaps. The convention for the TE and TM polarization is taken as the electric field is parallel to plane for the previous one and the magnetic field is parallel to plane for the latter one. The PBGs for both polarizations can be matched in frequency by selecting the proper structural parameters such as the radii of the rods and holes, and the refractive index of the various components of the structure.

The schematic diagrams of the structures are shown in Figs. 5.1(a) and (b). The dielectric rods of radius r_2 and permittivity ε_{r_2} are inserted in the middle of the holes with

radius r_1 and permittivity ε_{r_1} ($r_1 > r_2$). The new structure can be thought of as the combination of the dielectric rods in the low refractive index background and the holes in the high dielectric background. In general, ε_{r_1} and ε_{r_2} can be taken different; however, we assume here $\varepsilon_{r_1} = \varepsilon_{r_2} = \varepsilon_r$. The region where $r_2 < r < r_1$ is denoted *air* (ε_0) while other regions are denoted *dielectric* (ε_r); a is the PC lattice constant.

From the PBG maps of square- and triangular-lattice rods in an air and square- and triangular-lattice holes in a dielectric background, we can see that the rods of relatively small radius tend to support substantial TM gaps while the holes of relatively large radius tend to support substantial TE gaps. The aim is to merge these two desirable regions of the disparate PBG maps by varying the radii of the rods and holes. As the rod radius increases, the band gap moves to lower frequencies for the TM polarization. On the other hand, the band-gap frequencies move to higher values as the radius of the holes increases. Thus, to have substantial overlap of both the TE and the TM gaps, one needs to increase (reduce) the radii of the dielectric rods while that of holes are decreased (increased).

5.3 Results and discussion

The photonic band diagrams are calculated by the two-dimensional frequency-domain eigenmode solver [88, 89]. The computational error was estimated to be less than 2 % for the frequencies around the PBG. We first investigated the PBG variation as both the dielectric-rod radius r_2 and the air-hole radius r_1 are varied for the high-dielectric case $\varepsilon = 13$ (GaAs). It is obvious that when r_2 equals zero, the usual square and triangular lattice air-hole PCs are attained. One would expect that the PBG decreases with the

addition of more dielectric material inside the holes by increasing r_2 starting from zero. It can be seen from Figs. 5.2(a) and (b) that the PBG closes completely at first as expected. However, another PBG appears in the dispersion diagram if r_2 continues to increase. For the square-lattice PC, as r_1 decreases the first PBG also decreases monotonically with smaller r_2 values. The second PBG is larger than the first one and the r_2 values corresponding to the peaks of the second PBG move to the higher values. On the other hand, the first PBG of the triangular lattice first increases and then begins to decrease as r_1 decreases and r_2 increases. The first PBG closes and a second one appears. As r_1 decreases, the second PBG first increases, reaches a maximum, and then decreases while r_2 values corresponding to the peaks of the second PBG move to higher values monotonically again. These observations based on Fig. 5.2 confirm our aim to overlap the PBG of TE and TM polarizations via increasing (reducing) the radii of dielectric rods while decreasing (increasing) that of holes.

Figures 5.3(a) and (b) show the dispersion diagrams of a triangular lattice of the circular holes with $r_1 = 0.47a$ and the dielectric rods in the middle with two values of $r_2 = 0.02a$ and $r_2 = 0.14a$. The two r_2 values were selected to show the effect of the first PBG reduction in size and to indicate the opening of the second PBG. The insets are the first Brillouin zone of the triangular lattice. The dotted lines represent the TE modes and the solid lines represent the TM modes. The PBG is indicated as the shaded region that appears between the first TE and the first TM band gaps. The small inclusion of the dielectric rods reduces the width of the PBG as expected, at first up to a threshold value of around $(r_2 = 0.09a)$, because the upper TM band (dielectric band) shifts downward.

Meanwhile, the bands below the PBG remain similar compared to the bands above the PBG that moves towards the lower frequencies. However, increasing r_2 beyond the threshold value brings another PBG. The air band becomes the dielectric band for the second PBG in the dispersion diagram. Its size is comparable to the first PBG where gap width to mid-gap ratios are as follows for the two cases $\Delta\omega_{\max}/\omega_0 = 15.40\%$, $r_1 = 0.47a$, and $r_2 = 0.02a$; $\Delta\omega_{\max}/\omega_0 = 10.00\%$, $r_1 = 0.47a$, and $r_2 = 0.14a$. The PBG of the TE modes is reduced in size but that of the TM modes is increased in size. One astonishing result is that the upper edge of the TM band becomes flat even though other bands stay similar.

Similarly, Figs. 5.4(a) and (b) show the dispersion diagrams of a square lattice circular holes with $r_1 = 0.49a$ and the dielectric rods in the middle with $r_2 = 0.02a$ and $r_2 = 0.11a$. The reason for the selection of the r_2 values is the same as above and the insets show the first Brillouin zone of the square lattice. The dotted lines represent TE modes and the solid lines represent TM modes. The PBG is indicated as the shaded region that appears between the first TE and the second TM band gaps. The PBG behaves similarly to the previous case. The upper band edge of the second TM mode moves to lower frequencies swapping positions with the original PBG. It closes the PBG around a threshold value of around $r_2 = 0.08a$ and becomes the dielectric band for the second PBG. The second PBG is

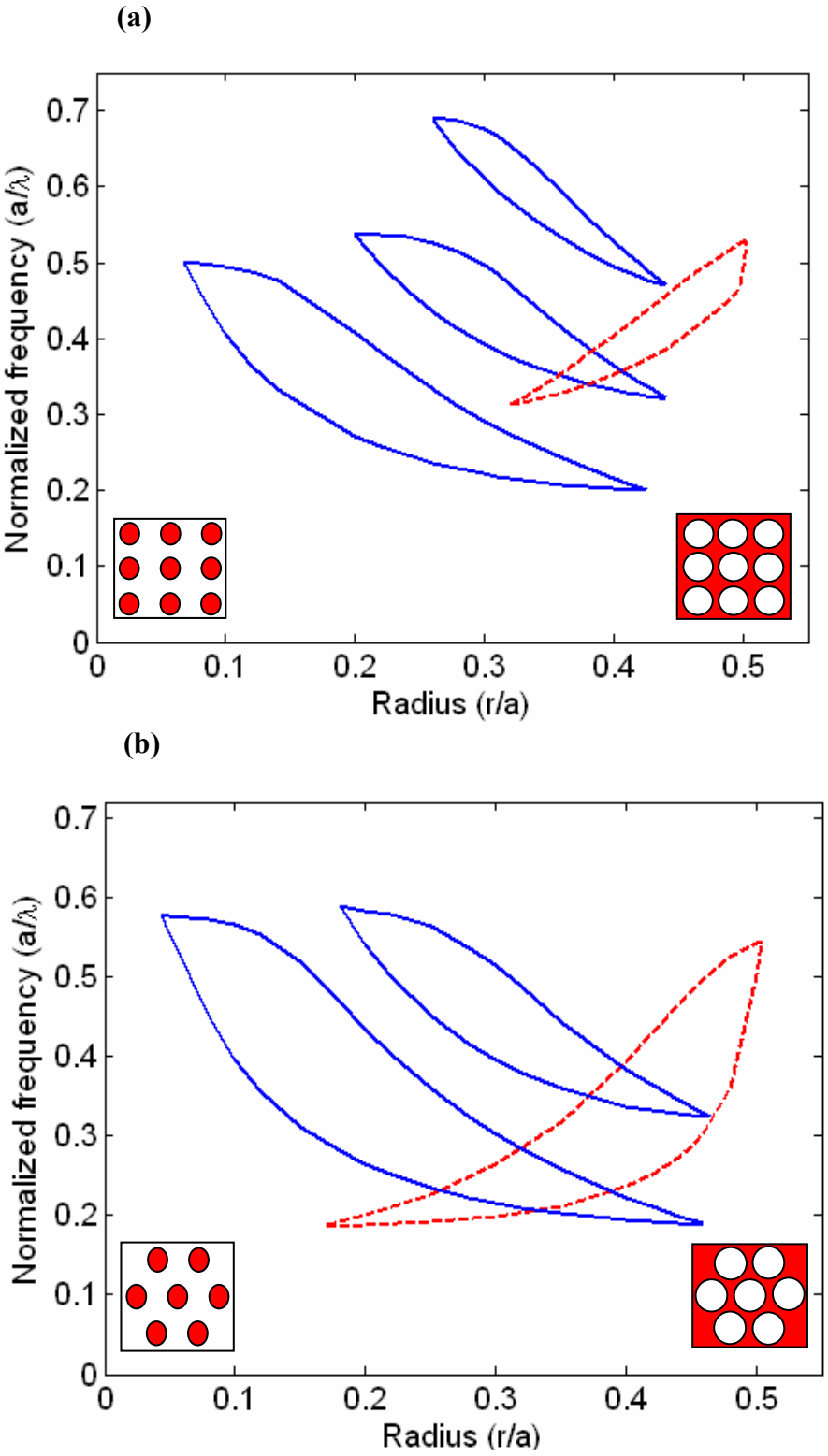

Figure 5.1: Band gap map of square and triangular lattice PC for air holes in dielectric background and rods in air.

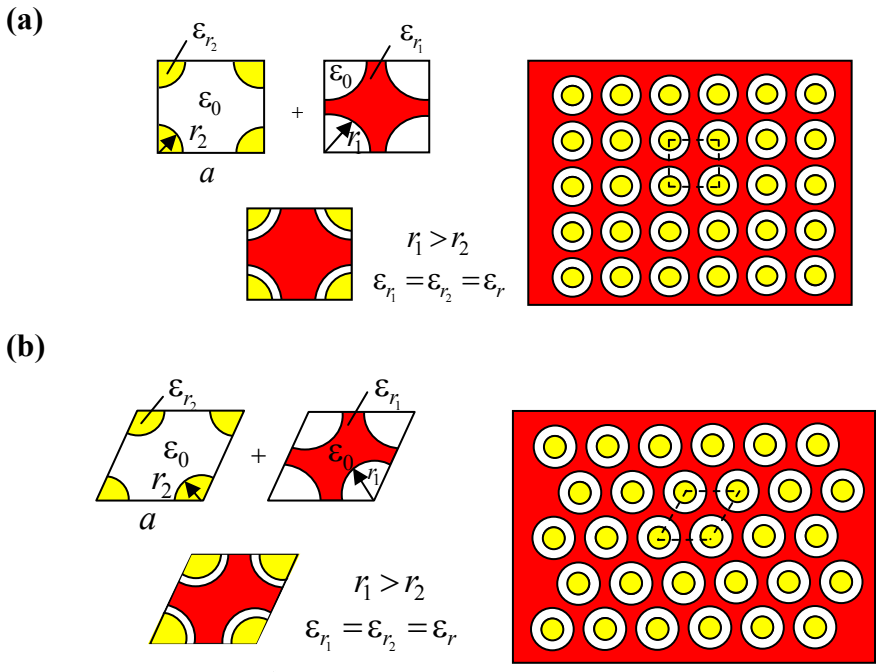

Figure 5.2: Schematic diagram of the PC lattice. (a) Square lattice with cylindrical dielectric rods of radius r_2 and permittivity ε_{r_2} are inserted in the middle of the holes with radius r_1 in dielectric background ε_{r_1} and $r_1 > r_2$. The unit cell is a combination of the dielectric rod in the air and hole in dielectric background. (b) Triangular lattice with cylindrical dielectric rods of radius r_2 and permittivity ε_{r_2} are inserted in the middle of the holes with radius r_1 in dielectric background ε_{r_1} and $r_1 > r_2$. The unit cell is a combination of the dielectric rod in the air and hole in dielectric background.

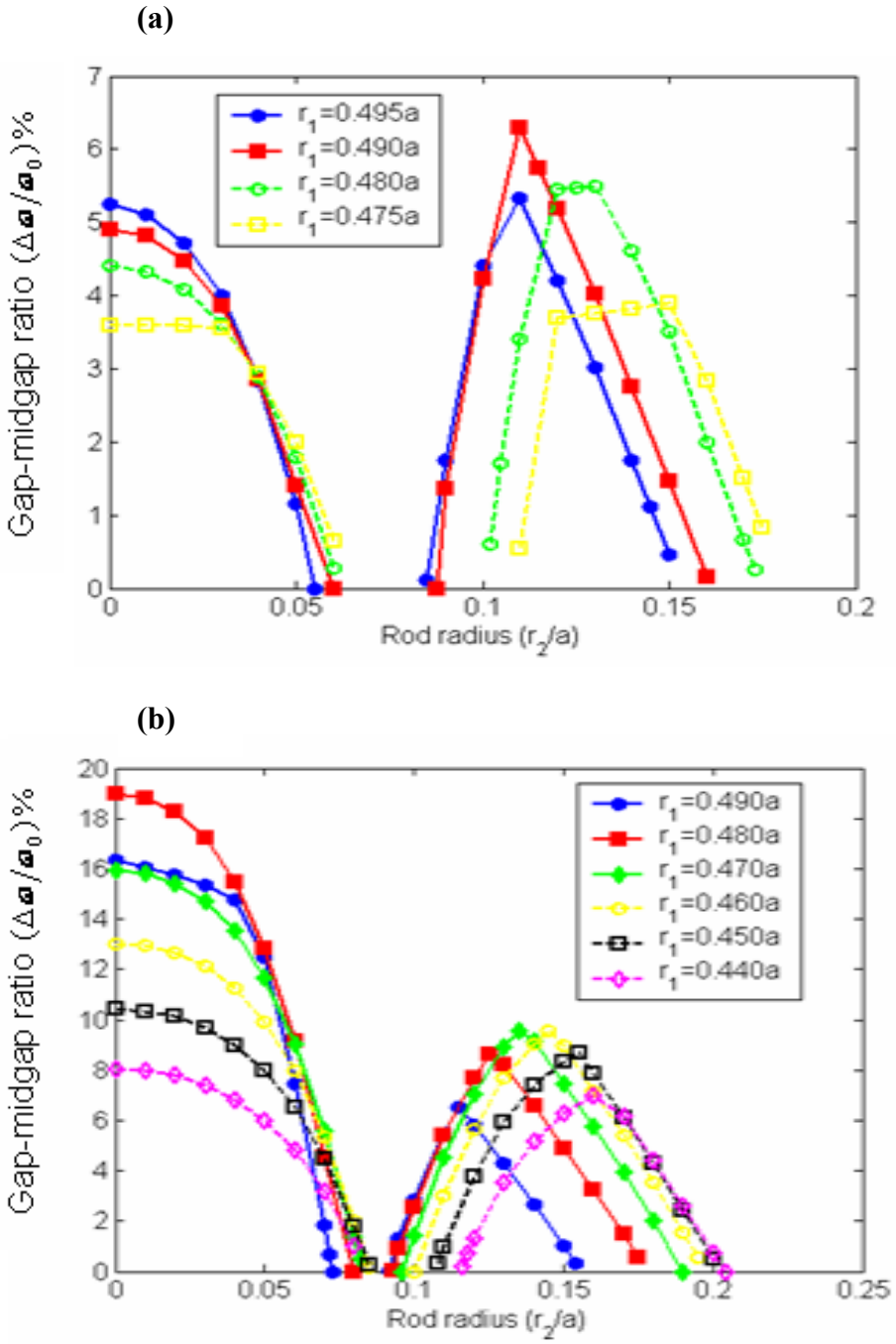

Figure 5.3: Complete PBG variation, $\Delta\omega/\omega_0$ with respect to the changes of inner dielectric rod radius. (a) Square lattice with r_1 from $0.49a$ to $0.47a$ and r_2 from zero to $0.20a$. (b) Triangular lattice with r_1 from $0.49a$ to $0.43a$ and r_2 from zero to $0.20a$. After the closure of the first PBG, the second one appears as r_2 increases.

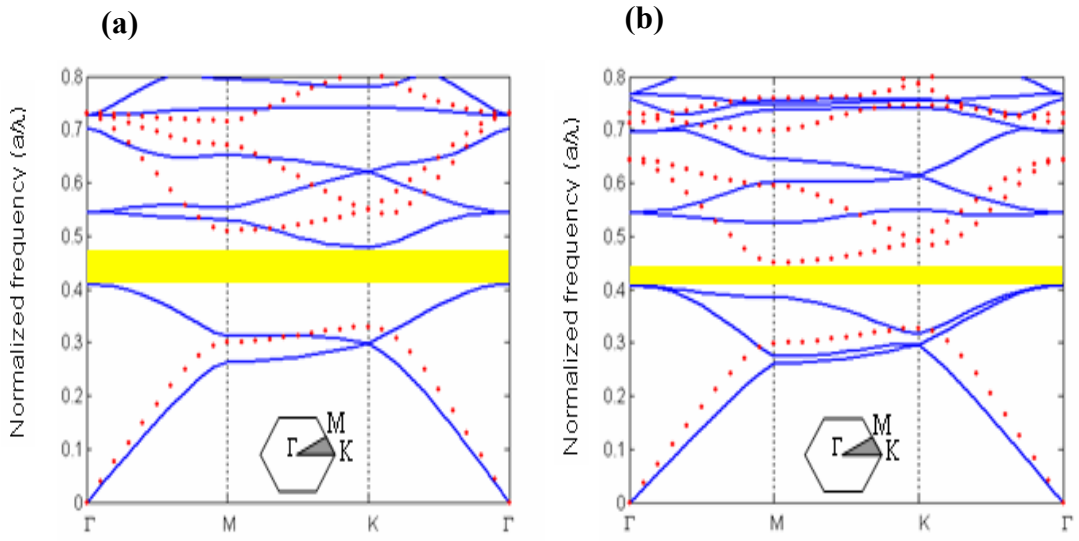

Figure 5.4: Dispersion diagram of triangular-array PBG lattice: (a) $r_1/r_2 = 0.47/0.02$ and $\varepsilon_r = 13$ (b) $r_1/r_2 = 0.47/0.14$ and $\varepsilon_r = 13$. Solid lines represent TM modes and dashed lines represent TE modes. The shaded frequency region corresponds to the PBG.

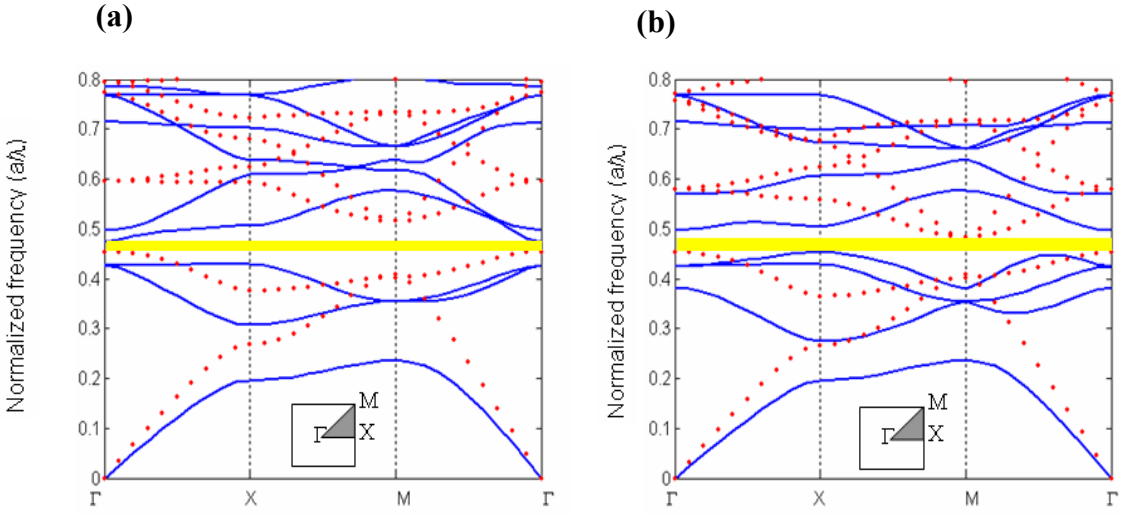

Figure 5.5: Dispersion diagram of square-array photonic-crystal lattice: (a) $r_1/r_2 = 0.49/0.02$ and $\varepsilon_r = 13$ (b) $r_1/r_2 = 0.49/0.11$ and $\varepsilon_r = 13$. Solid lines represent TM modes and dashed lines represent TE modes. The shaded frequency region corresponds to the PBG.

wider than the first PBG for the square lattice: for the first case, $\Delta\omega_{\max}/\omega_0 = 4.39\%$, $r_1 = 0.49a$, and $r_2 = 0.02a$; for the second case $\Delta\omega_{\max}/\omega_0 = 6.89\%$, $r_1 = 0.49a$, and $r_2 = 0.11a$. It is worth noting that the same lattice structure, either square or triangular, shows two PBGs in the same frequency region; one remains open only for small values of r_2 and the other one appears as r_2 increases beyond a critical value.

Inclusion of the dielectric rods within the structure shifts one of the TM band down. Changes to the inner structure (radius r_2, permittivity ε_{r_2}) affect the TM modes to a greater degree. On the other hand, variation of the matrix parameters such as r_1 and ε_{r_1} have more effect for TE polarizations. Since the air band is sensitive to the dielectric material added, it swaps the PBG region, first closing it and then becomes the dielectric band for the second PBG. In Fig. 5.6 images represent the electric field at M point (band number = 4) for low and high dielectric inclusions. The nature of the 4th band changes from air band to dielectric band. In Fig. 5.6(a), the field is mostly distributed through the veins and since the inner rod radius is small there is small field confined in the middle of the holes (higher frequency). However, for Fig. 5.6(b), the field is very well confined within the rods and reduces the frequency of the 4th band (lower frequency). One important conclusion that can be drawn from Fig. 5.6 is that the tunability of the TM modes (n=4 for square lattice and n=3 for triangular lattice) is quite large compared to the TE modes, which stay relatively unchanged. The movie shows the same electric field variations as the inner radius changes between $0.06a$ and $0.12a$. From these plots and movie, one can conclude the above mentioned statement such that as the amount of inserted dielectric material increases field stays confined and its frequency decreases. As a result, the air band of TM modes becomes the dielectric band of the same modes.

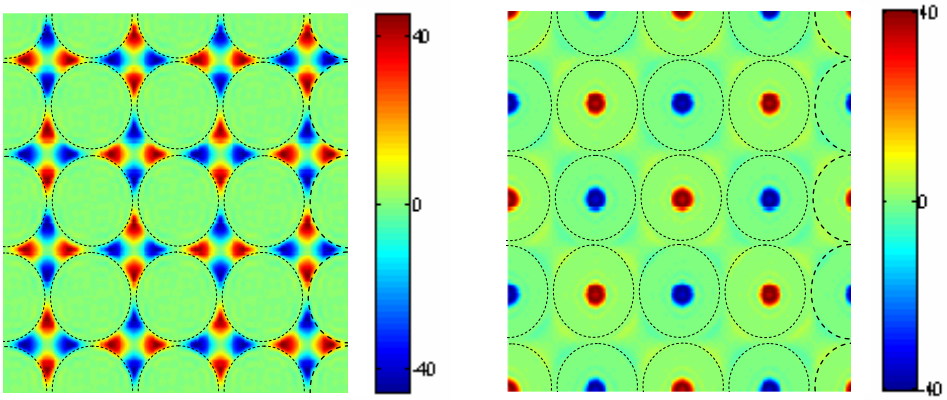

(a) **(b)**

Figure 5.6: Electric field of TM modes for square array of annular photonic crystal. The inner rod radius is $0.02a$ (left) and $0.12a$ (right).

We also looked at the case where the dielectric constant is $\varepsilon = 16$, as in germanium (Ge). An important feature is obtained. Though both the first PBG where $r_2 = 0$ and the second PBG where r_2 is greater than the critical value are enhanced with the high permittivity, the enhancement of the second PBG is almost doubled for the square and triangular lattice compared to the case of $\varepsilon = 13$ and the first PBG only increases slightly in size (Square lattice: the first PBG, $\Delta\omega_{\max}/\omega_0 = 4.83\%$ to 6.50%, $r_1 = 0.49a$, $r_2 = 0$ and the second PBG, $\Delta\omega_{\max}/\omega_0 = 6.89\%$ to 9.69%, $r_1 = 0.49a$, $r_2 = 0.11a$. Triangular lattice: the first PBG, $\Delta\omega_{\max}/\omega_0 = 15.90\%$ to $18.21\%, r_1 = 0.47a$, $r_2 = 0$ and the second PBG, $\Delta\omega_{\max}/\omega_0 = 10.00\%$ to 18.34%, $r_1 = 0.47a$, $r_2 = 0.14a$). Table 5.1 and 2 list the values of different cases. The first PBG is determined by the TM modes and the second PBG is determined from below by the TM mode and from above by the TE mode for the triangular lattice.

TABLE 5.1. The comparison of the usual and annular PC square lattice.

	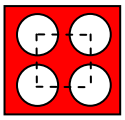 $r_1 = 0.49a$	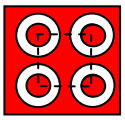 $r_1 = 0.49a$ $r_2 = 0.11a$
$\varepsilon = 13$	$\Delta\omega_{\max}/\omega_0 = 4.83$	$\Delta\omega_{\max}/\omega_0 = 6.89$
$\varepsilon = 16$	$\Delta\omega_{\max}/\omega_0 = 6.50$	$\Delta\omega_{\max}/\omega_0 = 9.69$

TABLE 5.2. The comparison of the usual and annular PC triangular lattice.

	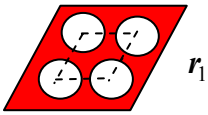 $r_1 = 0.47a$	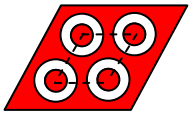 $r_1 = 0.47a$ $r_2 = 0.14a$
$\varepsilon = 13$	$\Delta\omega_{\max}/\omega_0 = 15.90$	$\Delta\omega_{\max}/\omega_0 = 10.00$
$\varepsilon = 16$	$\Delta\omega_{\max}/\omega_0 = 18.21$	$\Delta\omega_{\max}/\omega_0 = 18.34$

Therefore, increasing the refractive index brings the first PBG to lower frequencies shifting the TM band pairs. However, for the second PBG, since the upper edge is TE and lower edge is TM, the TM mode shifts more than the TE toward the lower frequencies. Therefore, the increment of the second PBG as a result of the refractive-index change is larger. For the square lattice, the first PBG is determined by the TE mode from below and the TM mode from above. The second PBG, on the other hand, is bounded by TE mode. Both PBGs move to lower frequencies and due to differences between TE and TM modes response to the refractive index increment wider PBG was obtained.

There are two conditions that are important to achieve a PBG for all polarizations. One is to confine strongly the lowest order mode (dielectric band) in the dielectric region hence to lower the frequency and push the higher order modes in the air region hence increase the frequency. The other condition is related to either the radii of the dielectric rods or the amount of the dielectric background. The dielectric medium should have enough area to support primarily the lowest band and to be small enough not to be able to support higher order modes. The electromagnetic boundary conditions help elucidate why the TM modes are favored by the isolated dielectric rods and the TE modes are in the connected regions. Due to the boundary condition on the normal component of the electric flux density in the absence of charge density, the electric field is mostly in the air region for the dielectric rods surrounded by air. Thus the first condition is not satisfied for TE case. Consequently, there is no band gap. For the TM mode since the tangential component of the electric field must be continuous at the boundary, the field can be confined in the dielectric medium more strongly than in the TE case. The second condition can be achieved by having rod radius r_2 around $0.2a$ such that the higher order

modes have nodes in the dielectric medium. For the holes in the dielectric background the scenario is different. Since one needs to have less dielectric material therefore radius of the hole should be fairly large. As a result, the connectivity helps TE modes to have a PBG. At some air-hole radius r_1 the lattice also looks like dielectric rods in air giving rise to a band gap for the TM polarization. Since the new structure (annular PC) has dielectric rods inside the air holes the rods are sensitive to TM polarization more than the dielectric background which plays similar role for TE polarization.

Since the symmetry of the lattice is preserved by the inclusion of the dielectric rods, the degeneracies at the symmetry points (Γ, M, and K) are unchanged. The structure is simple and the PBG is obtained at well less than close-packed conditions. In addition, the PBG appears at low frequencies, making it less susceptible to the disorder.

With the usual lattice geometry one can have only the radius of air holes and the background of the dielectric material to change the dispersion properties of the PC. On the other hand, annular PC's provides extra two more variables due to inner rod (radius and refractive index) that can be utilized to alter the properties of the crystal such as to implement the tunability. This is another advantage of the annular PC. It may find other advantages especially when implemented in applications such as super-prism or self-collimations, switches, and splitters.

To show that the inclusion of dielectric rods (annular PC) is not the same as simply increasing the filling factor inside the holes, we have made several comparisons. Consider a unit triangular lattice annular PC ($r_1 = 0.15a$, $r_2 = 0.45a$, $\varepsilon = 13$) in the four configurations (Fig. 5.7): (i) dielectric rod ($r_1 = 0.15a, \varepsilon = 13$) in the low index medium ($\varepsilon = 4.468$), (ii) the high index background ($\varepsilon = 13$) filled with low index

material ($r_2 = 0.45a,\ \varepsilon = 2.333$), (iii) air holes in the high index medium ($r_3 = 0.424a,\ \varepsilon = 13$), and finally (iv) high index dielectric rods in air ($r_4 = 0.309a,\ \varepsilon = 13$). When we consider the dispersion diagrams of these configurations, there is no complete PBG for cases (i), (ii) and (iv), while there is PBG only for case (iii), which is almost half of the gap of the annular lattice structure as indicated in Fig. 5.8. Thus, the approach presented in this work (annular PC) is clearly different than simply increasing the filling factor within the unit cell.

The story is different when the dielectric contrast is low because it is difficult to achieve a complete PBG at low refractive-index values. At low dielectric values ($\varepsilon_r = 4$) the air hole square lattice has TE and TM gaps at close-packed conditions. Besides, the TE gap is very small. However, the new structure has a fairly high TE band gap as shown in Fig. 5.9(a) for the values of r_2 and r_1 that are likely to ease fabrication. For the air-hole triangular lattice, the TE band gap is available for very low dielectric values with large filling ratio. However, there is no TM gap for the low dielectric contrast case well away from the close-packed condition. On the other hand, the new structure has a very large TM band gap for a large range of r_2 and r_1 as shown in Fig. 5.9(b).

It has been shown that a larger PBG can be obtained as the lattice symmetry and the scatterer shape (e.g., circular or square) are the same i.e., square rods or holes in a square lattice and circular rods or holes in a triangular lattice [90]. It may thus be possible to enhance the PBG of the square lattice even more with the square rods inserted inside of square holes instead of circular rods inserted inside of circular holes.

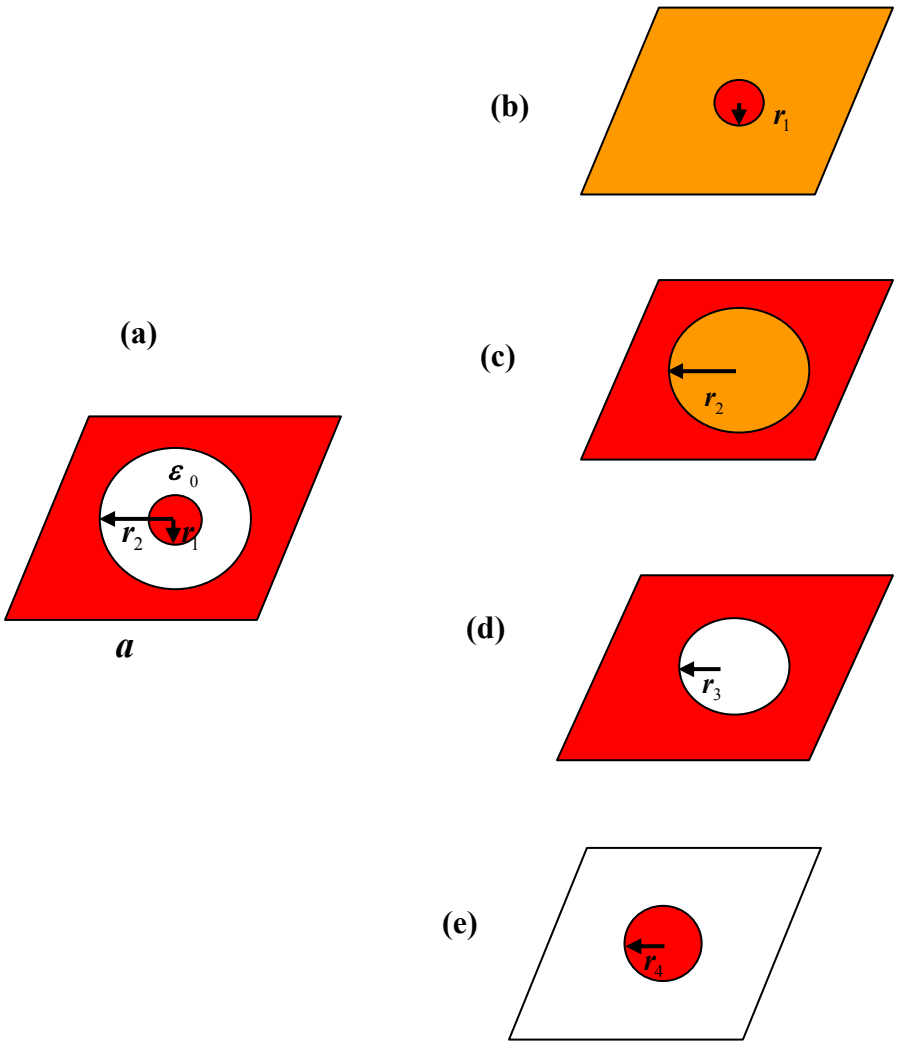

Figure 5.7: Annular photonic crystal unit cell $(\varepsilon = 13, r_1 = 0.15a, r_2 = 0.45a)$ (a) and its decomposition in to four types of lattices: (b) high dielectric rod $(\varepsilon = 13)$ in low refractive index $(\varepsilon = 3.389)$ background (c) holes filled with low refractive index $(\varepsilon = 2.064)$ material and the high refractive index background $(\varepsilon = 13)$ (d) air holes in high refractive index background $(r_3 = 0.424a, \varepsilon = 13)$ and (e) dielectric rods in air $(r_4 = 0.309a, \varepsilon = 13)$.

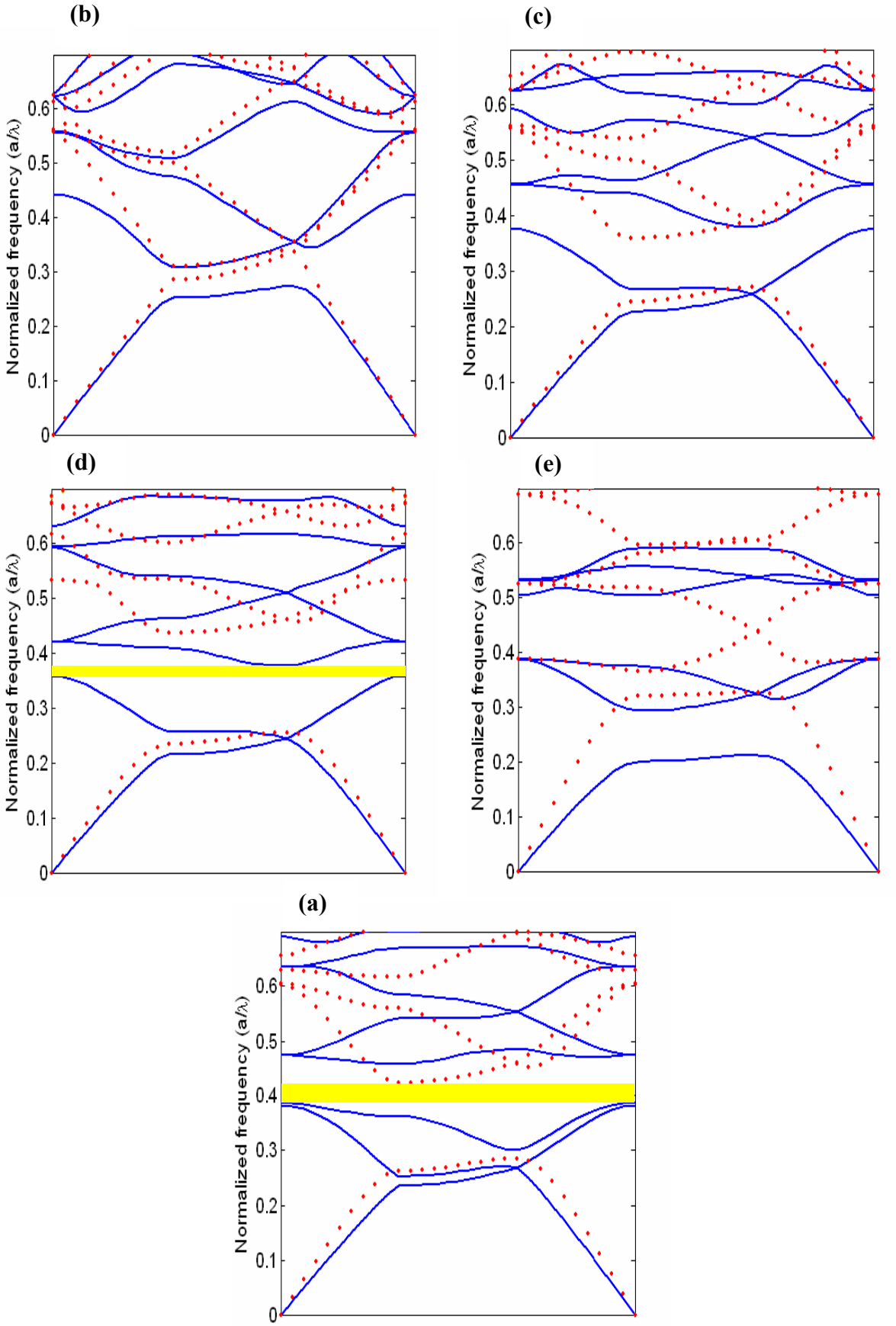

Figure 5.8: Dispersion diagrams of the lattices in Fig. 5.6.

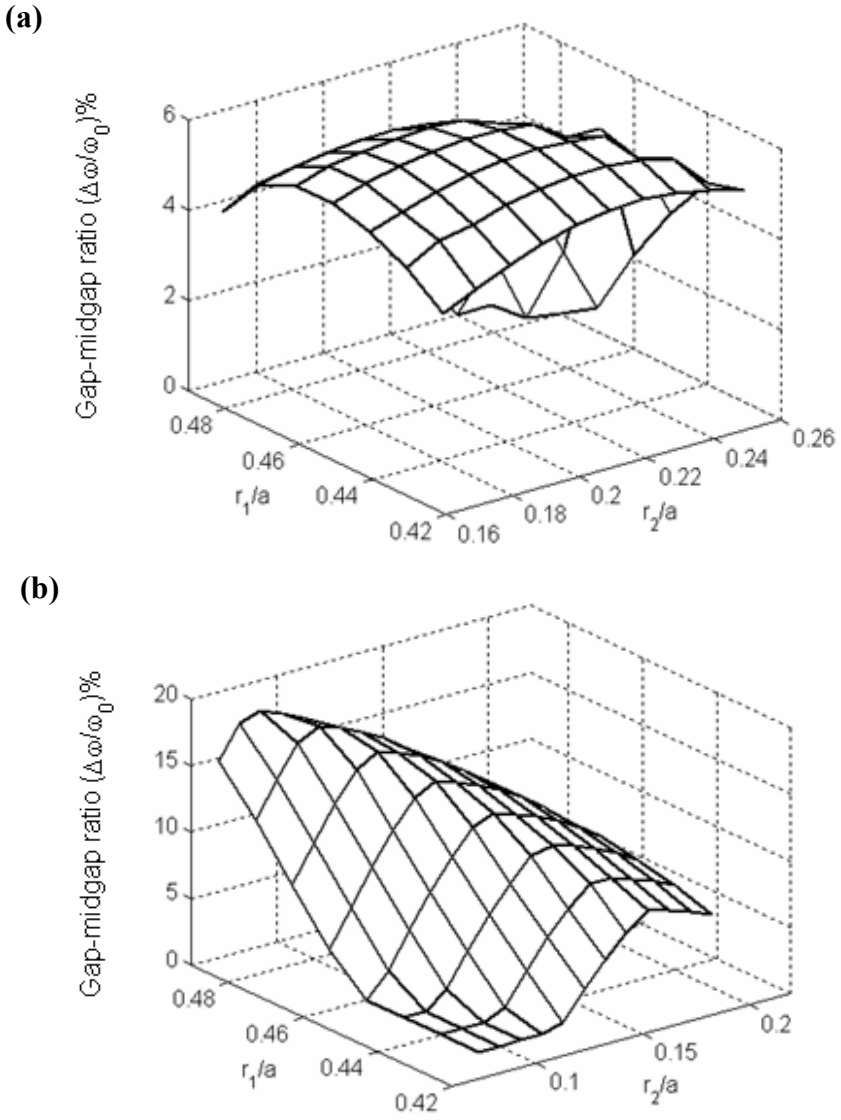

Figure 5.9: (a) PBG to midgap ratio, $\Delta\omega/\omega_0$, for square lattice with low dielectric value ($\varepsilon_r = 4$) for the TE modes with respect to the rod radius r_2 and hole radius r_1. (b) PBG to midgap ratio, $\Delta\omega/\omega_0$, of triangular lattice with low dielectric value ($\varepsilon_r = 4$) for the TM modes with respect to the rod radius r_2 and hole radius r_1.

The analysis is carried out for the ideal 2D case assuming infinite thickness in the z direction. We also presented the work with unperturbed annular PC. However, annular PC should have finite thicknesses for device applications. Since the confinement in the vertical direction relies on index guiding in this case, out-of-plane scattering losses become critical [91, 92].

One may envision our annular PC structure either as a very thin slab supported by a low index substrate, such as silicon-on-insulator and operating below the light-line with excited Bloch modes, or as a photonic heterostructure, where the core is sandwiched between cladding layers on both sides (three-layer structure). In the latter case, the scattering loss is roughly proportional to the index contrast between the layers. Therefore, the index contrast should be low with deeply etched holes to reduce the scattering losses. In fact, increasing the depth of the cladding layers with small index contrast differences is an approximation to the ideal 2D PC. The origin of the out-of plane scattering losses is due to the air holes where there is no local guiding in the vertical direction. The radiation losses increase as the air fraction increases. Since the inner dielectric rods in the center of the each air hole reduce the distance that the light travels in air we think that annular PC will reduce that loss. Other losses due to manufacturing imperfections or structural disorders may degrade the performance of the annular PC compared to usual PC as the former has one more sidewall within each unit cell. However, strengthen the arguments above, further work is needed. For example, analysis including the out-of plane losses (adding an effective imaginary ε within the air holes) and the finite thickness of the structure by the effective index method may be needed to provide better answers to the above questions.

5.4 Conclusion

In conclusion, we have analyzed the proposed structure, a two-dimensional annular photonic-crystal composed of a dielectric-rod and a circular-air-hole array in a square or triangular lattice such that the dielectric rod is centered within each air hole, in two different cases where the dielectric contrast is very high and very low. The inner dielectric rod reduces the PBG width and closes completely as expected. On the other hand, increasing the radius of the rod after the closure of the PBG gives rise to a second PBG. In some cases, this second PBG is larger than the PBG that one can get from the original PC lattice (circular and square lattice air hole array in dielectric background). Partial PBGs were obtained for certain polarizations for the low-contrast dielectric case. The ability to control TE and TM band gap with some degree of independence may vastly broaden the interest in two-dimensional PC structures.

CHAPTER VI

Photonic-crystal heterostructure waveguides

6.1 Introduction

Two-dimensional (2D) periodic dielectric structures, or photonic crystals (PC), can provide a light guiding via two main mechanisms depending on PC waveguide (PCW) design: utilizing either the band-gap effect for frequencies within the gap or a dispersive effect known as self-collimation for frequencies around but outside the gap [93, 94]. In the former case, the full 2D periodicity of the lattice is broken, while the underlying structure is unperturbed in the latter case. Ultimately, PCW bends are expected to be essential building blocks of photonic integrated circuits no matter what the guiding principle may be. While bending the light through large angles with high index-contrast materials is possible using conventional dielectric waveguides, the corner radii of such bends cannot typically be reduced to the regime of the electromagnetic wavelength—a limitation that may be a bottleneck for making extremely compact devices. Two-dimensional PCs, however, bring entirely new possibilities to control the flow of light. Sharp corners having small radii of curvature yet high transmission can be obtained because the guiding mechanism in the plane of the periodicity is due to distributed Bragg reflection, while total internal reflection confines the light in the vertical direction [33, 34]. PCW bends may thus play a major role to route optical signals efficiently through the optical circuitry. Early theoretical and experimental work proposed various types of PCW bends. Here we focus on PCWs obtained by introducing line defects in otherwise period 2D PCs with the aims

of enhancing the typical poor and low-bandwidth transmission through sharp PCW bends.

Due to the large TE (electric field is in the 2D periodic plane) band gap, PCs with a triangular lattice of holes in a high dielectric background (e.g. $\varepsilon = 12$ for Si) are a common selection. We therefore chose this structure as our starting point. One can form a PCW by filling in a row of holes (a line defect) with the background dielectric in special directions, such as ΓK in these crystals. The six-fold lattice symmetry easily enables a bending angle of 60^o by coupling two line defects along ΓK direction. Limiting design to bends through this angle is a strong constraint on photonic integrated-circuit design; clearly the availability of bends with other angles is highly desired.

There have been several approaches to improve the efficiency of light transmission through PCW bends. One is to modify the lattice in the vicinity of the bend by shifting the hole centers. As a result, the corners are effectively smoothed and the width of the corner region is reduced to suppress the high-order modes that may be present while passing the bend. Other methods include the introduction of a low-Q or high-Q cavity, topology optimization, and using polycrystalline structures [95-99].

Some of the drawbacks of the above methods are as follows. Introducing a defect may increase out-of plane radiation losses, and in some cases the small radii defects introduce additional fabrication difficulties. Moreover, such an approach typically provides transmission enhancement within a relatively narrow frequency band. High-Q resonators incorporated in the corners may also provide high transmission only for a narrow band of high transmission. Low-Q resonators, however, are good for broadband transmission, but that transmission is usually not high. Corner regions modified by topology optimization are usually complex in shape

so that manufacturing problems may arise. Other device applications such as Y-splitters may not be feasible with polycrystalline structures due to the irregularities at the junctions. Once again, nearly 100 % transmission is obtained only for a small range of frequencies. For broad bandwidth transmission, the overall efficiency is typically low even though there is significant improvement compared to the basic PCW bend structure. Most of the aforementioned approaches have preserved the underlying triangular lattice PC geometry and have only optimized the part of the structure around the corners or sides of the bend region.

A physical understanding of the origins of the bend losses is important to guide the devising of effective solutions. We first note that the propagating mode experiences a rotation of its phase fronts at each corner. Thus, if this rotation cannot be provided smoothly, then significant radiation loss may occur. The wave fronts must be slowed down and/or accelerated above and below the PCW center, respectively, to suppress the modal mismatches and reduce the back reflections. Back reflections may be reduced with small angle bends. Since the lattice geometry already fixes a natural bend angle (either 90^0 for square PCs or 60^0 for triangular PCs) there are few obvious alternatives for other angles.

6.2 Design of photonic-crystal heterostructure waveguides

PC heterostructures are formed by sequentially connecting PCs with different lattice constants or underlying crystal symmetry. Such structures have been proposed for nanocavity and line drop filters. It has been shown that they can provide far superior performance compared with more common PC structures [100, 101]. The purpose of employing PC heterostructures we propose here is entirely different from those hitherto studied. Our aim is to lift the angle constraints imposed by a single lattice

type—in particular to increase light throughput by reducing the bending angle while maintaining a small radius of curvature. We examine the properties of a heterostructure between a triangular-lattice-based PCW and a novel deformed triangular-lattice-based PCW. Specifically, we consider a PC heterostructure composed of regions of PCW-bearing triangular PCs and regions of suitably designed deformed PCs in the bend region obtained by suitably squeezing the triangular PC in the ΓM direction, but retaining the structure intact in other directions, as shown in Fig. 6.1; Figure 6.2 shows the schematic layouts of the two PCs and their Brillouin zones (BZ) with the irreducible BZ corners labeled. As can be seen, the BZ of the deformed PC is a rotated and enlarged version of that of usual PC. In this way we obtain a lattice type which can provide any angle θ between lattice vectors $\vec{a}_1$ and $\vec{a}_2$ where $\vec{a}_1 = a\hat{x}$, $\vec{a}_2 = \frac{a}{2}\left(\hat{x} + \tan\theta\,\hat{y}\right)$ and a is the lattice constant. The usual triangular lattice PC has $\theta = 60^0$ and for this work we take $\theta = 30^0$ for the bend angle, as we explain later. The deformation is represented by $\vec{\delta} = \mp\frac{a}{2}\left(\sqrt{3} - \tan\theta\right)\hat{y}$.

The great flexibility of this approach is that using this deformed lattice, one can also obtain a 90^0 degree bend with the triangular lattice PC (in two bending steps, 30^0 and 60^0) and further build up also Y-type splitters and other structures. Denser PC structures are also possible as the length of the lattice in ΓM direction is reduced by one third.

The dispersion diagram of the deformed PC is calculated in the entire first BZ to ensure that the PC has a complete band gap. The band diagram, shown in Fig. 6.3,

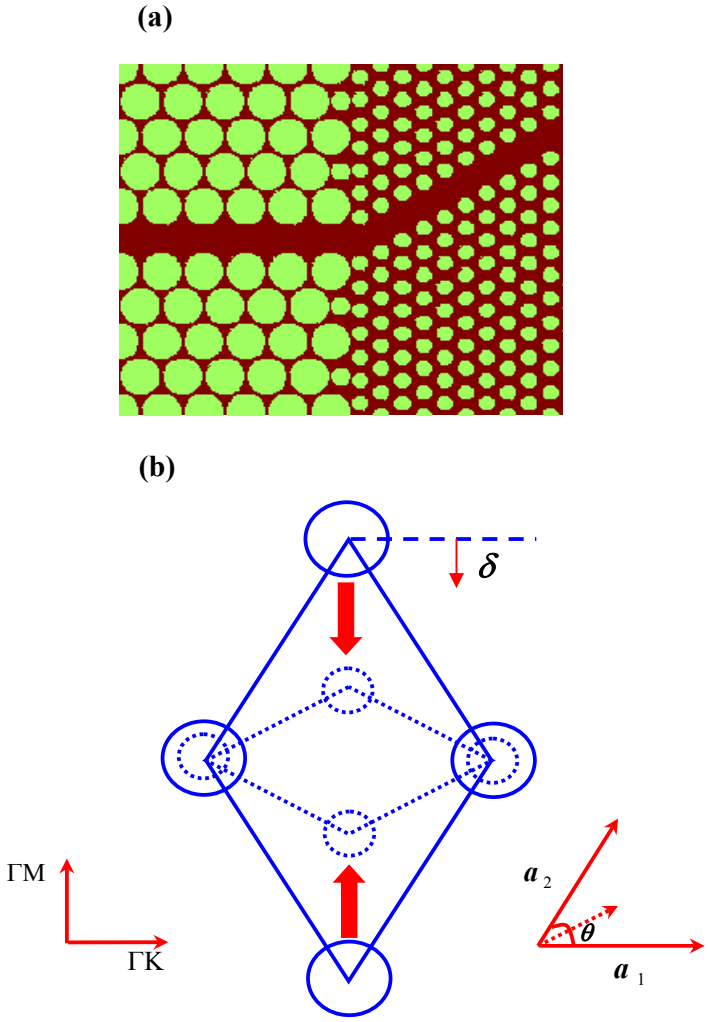

Figure 6.1: Schematic layout of the photonic crystal hetero structure waveguide bend and the unit cell configuration. (a) Two different photonic crystal waveguides is combined to provide 30^0 bend. (b) The diagram illustrates how to obtain the proposed lattice photonic crystal from the original lattice triangular array PC by deforming in ΓM direction only. The perturbed unit cell is shown as the dashed line. Basic lattice vectors a_1 and a_2 are also shown. The perturbation is represented by δ.

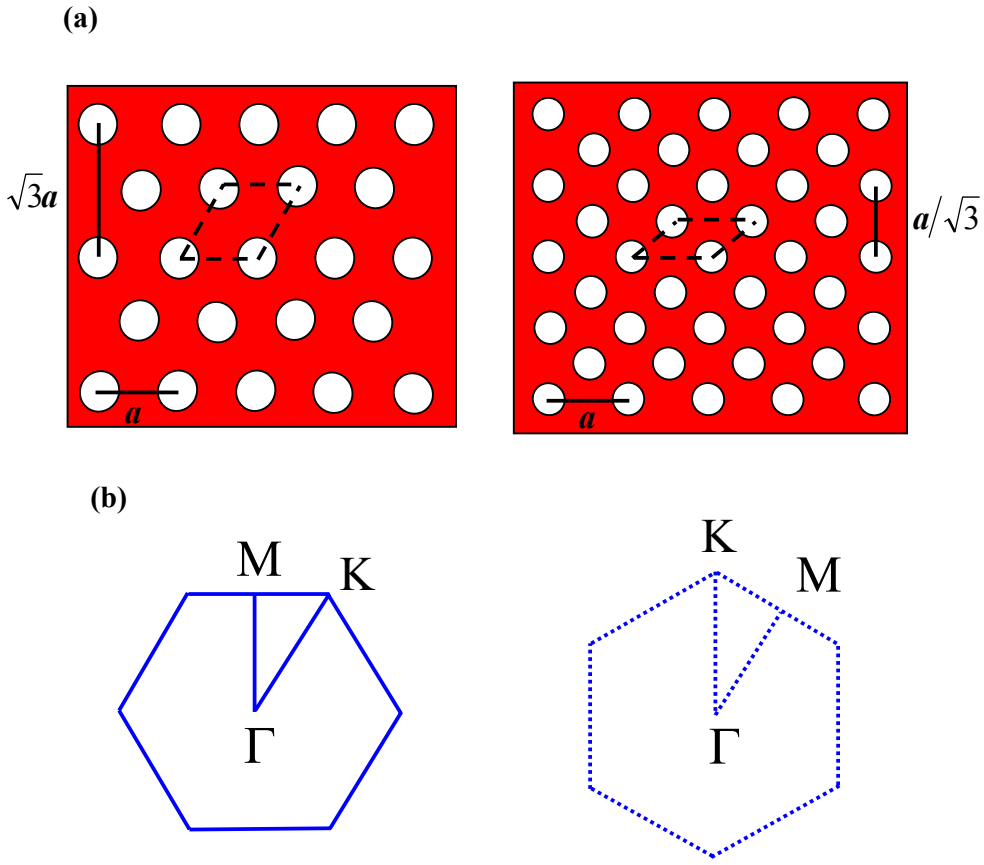

Figure 6.2: The usual triangular lattice photonic crystal and the perturbed photonic crystal. (a) Schematic diagrams of triangular array PC and its deformed one in ΓM direction. Both have the same length in ΓK direction but the length in ΓM direction is reduced by one third. (b) Brillouin zones (BZ) of each photonic crystal and the irreducible BZ corners (high-symmetry points) are labeled.

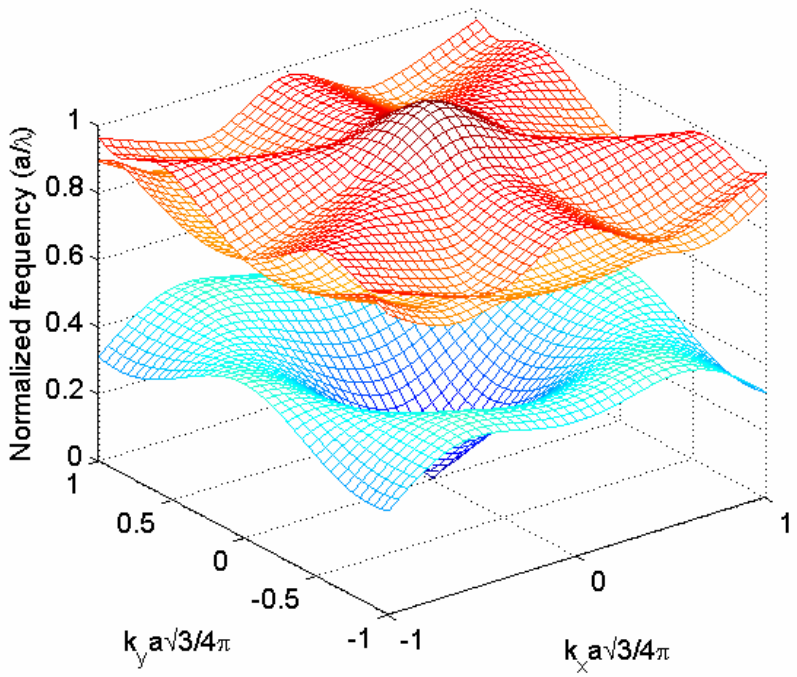

Figure 6.3: Dispersion diagram. The diagram is for the deformed photonic crystal with hole radius $r = 0.25a$ where a is the lattice constant and relative permittivity of the dielectric background $\varepsilon = 12$.

exhibits a band gap at relatively high frequencies $(0.4757 < a/\lambda < 0.7957)$ for $r = 0.25a$ and $\varepsilon = 12$, parameters representative of semiconductor-based structures. One characteristic of the deformed lattice can be understood on the basis of the scalability of the Maxwell's equations: band-gap frequencies calculated by the planewave expansion method experience an upward shift proportional to the perturbation amount $(\sim 67\%)$ defined as the percentage ratio of the deformation induced to the maximum deformation $100\,|\delta|_{0^0<\theta<60^0} : |\delta_{\max}|_{\theta=0^0}$, as plotted in Fig. 6.4.

A natural question that may arise is how to choose an appropriate value of θ. The selection of θ is constrained as follows. On the one hand, if θ is too small, as a result of the large deformation that results, one cannot employ large-radius holes. On

the other hand, small-radius holes may cause fabrication difficulties. In addition, the band-gap frequencies in the deformed PC move to fairly high values and thus there may not be sufficient overlap in the band gaps of the deformed and usual PC, which is an essential requirement (as we discuss below) to ensure high, broadband transmission. Moreover, small-angle bends mean longer lengths of deformed-lattice PCWs are required to direct the light to its destination, and this contradicts the idea of employing PC structures for compact photonic integrated circuitry. Above all, symmetry and connectivity of the PCs are crucial for the deformed PC to possess a significant band gap. For example, for $\theta = 45^0$ the structure resembles a rotated square lattice and its performance for the TE modes is quite poor, i.e., the band-gap width is narrow. Therefore, applications utilizing the photonic band-gap effect restrict the selection of θ. One notes that if one depends on index guiding, then most of the aforementioned problems are no longer relevant and θ can be chosen from a larger range of values. The general idea here is to halve the bend angle of a triangular lattice while keeping the lattice symmetry almost the same. As can be seen from the schematic diagrams shown in Fig. 6.2, the two PC structures have same lattice constant a in one direction but the deformed PC is denser in the other direction.

Figure 6.5 shows the path-length difference L of the propagating wave fronts due to the bend and it is equal to $L = |BB'| - |AA'| = W_b \tan(\theta)$ where W_b is the width of the waveguide bend and θ is the bend angle. Comparison of the L values of 60^0 and 30^0 PCW bends reveal that it is reduced by approximately 3.5 times with the latter case.

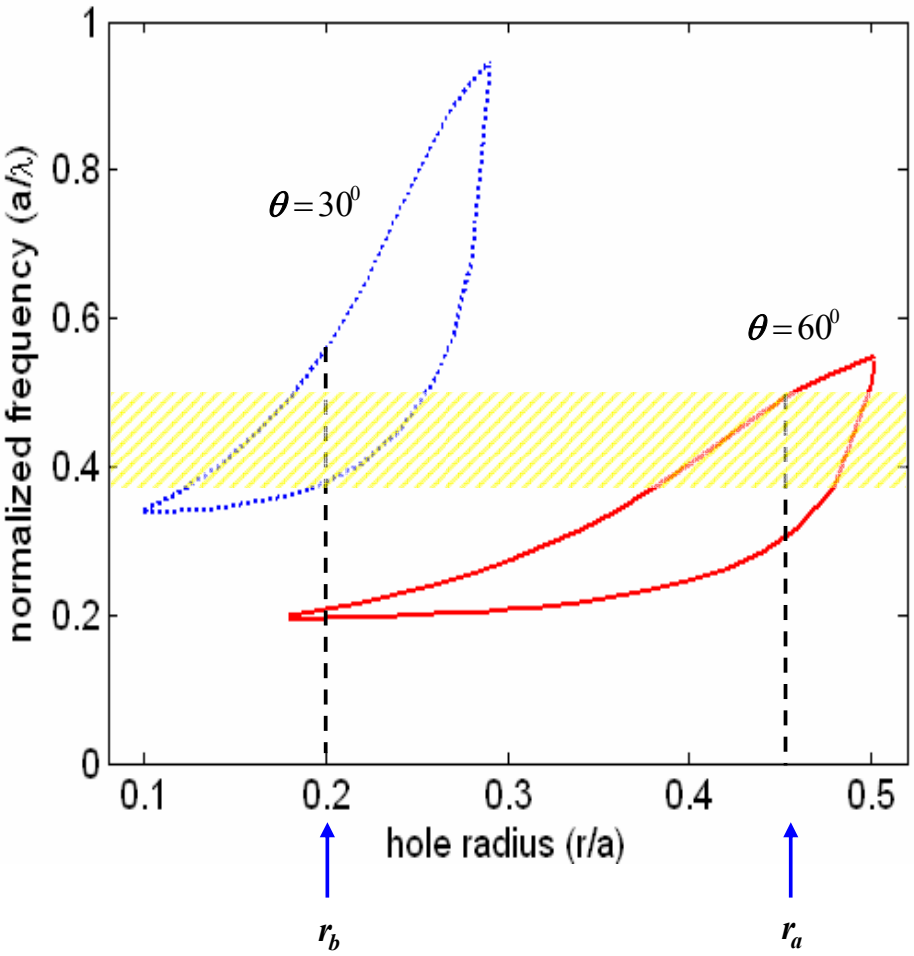

Figure 6.4: Band gap map. The usual and the deformed triangular lattice photonic crystal provide photonic band gap for TE modes. The overlap of the band gap frequencies is shaded for the hole radius of usual lattice $r_a = 0.45a$ and hole radius of the deformed lattice $r_b = 0.20a$.

From this simple argument, one may easily see the advantage of reducing the bend angle to improve the transmission around the corners as a result of small path-length difference. This also explains why most of the aforementioned approaches modified the BB' section to accelerate the wave fronts in this part of the junction by increasing the volume of the low index material. Similarly, the AA' section is used to

decelerate thewave fronts by increasing the effective index in this region of the bend. Either increasing the effective index in AA' or reducing it in BB' may work as well instead of changing θ. The modifications made in this region, however, may degrade the performance of the PC. Increased out-of-plane scattering losses may result due to adding small holes in addition to manufacturing difficulties. Next we explain the methods and the design steps.

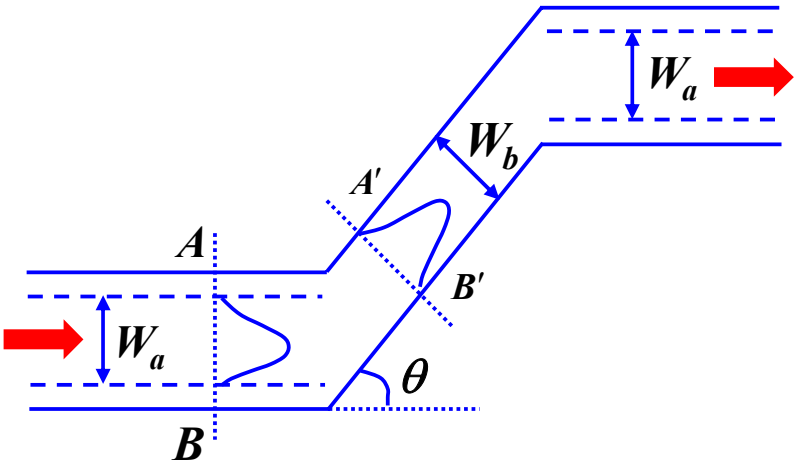

Figure 6.5: Illustration of photonic crystal heterostructure waveguide bend parameters. The waveguide widths are represented by W_a and W_b, the width of triangular lattice photonic crystal waveguide and the width of the deformed lattice photonic crystal waveguide respectively. They made equal to the lattice constant ($W_a = W_b = a$).

6.3 Calculating the bending efficiency

Naturally, the aim is to improve the transmission of this structure with respect to a standard 60^{o} PCW bend. The input and output sections of PCWs are retained undeformed. One must engineer them ultimately for input and output coupling to further devices, but such questions are beyond the scope of this article. Figure 6.6 represents the structure layouts for two different cases.

To suppress overlap and thus interference of fields localized near the bends, the length of the bend region must be sufficiently long. All studied structures have the same input and output coupling PCW to extract the effect of the bends themselves. The efficiency analysis is carried out by the 2D finite-difference time-domain (FDTD) method assuming perfectly matched layer boundary conditions surrounding the entire structure [52, 53]. To obtain correctly the power transmission coefficient $\eta(\omega)$ of the PCW incorporating bends, special care has to be taken. The input and output detection points should be placed inside the PCW properly to suppress end effects and reflections. As long as the structure is large enough and the input pulse is a sufficiently narrow-band modulated Gaussian, the input and output pulses can be separated temporally from the reflected pulse, as will be shown later. The time-averaged Poynting vector $S = \frac{1}{2}\mathrm{Re}\left[E \times H^{*}\right]$ is integrated over a cross section through the PCW to obtain the input and the output power where E is the electric field and H^{*} is the complex conjugate of the magnetic field. Since the field associated with a confined PCW mode decays exponentially in transverse directions, enough field points are taken for the calculation of S. The ratio of the output power to the input gives the waveguide bend transmission $\eta(\omega)$. To obtain the reflection coefficient the reflected power is divided by the input power. We also check to ensure that the center

PCW region is sufficiently long so that the results are independent of its length. Below we outline design steps for a case study.

Design Steps (for guiding by PBG effect): We assume perforated holes in a dielectric background with high-refractive index ($\varepsilon = 12$, representative of a range of commonly employed semiconductors, such as Si or GaAs). The width of the PCW is important to transmit and bend the signal properly. PCWs obtained by removing more than one row of holes can propagate signals better, but due to the multimode nature in the bend region, the transmission may be poor. Since the aim here is to enhance the transmission through the bends, we adjusted the widths of the two PCWs accordingly. One row of holes is removed in the 30^0 bending region, and, consequently, the width of the straight parts must be adjusted as a result.

The design steps are thus as follows: (i) Start with the band-gap maps of both PC structures and select the radii of air holes that provide the best overlap of the two band gaps. According to Fig. 6.4, if we select $r_a = 0.45a$ and $r_b = 0.20a$, then the two band gaps overlap at $0.379 < a/\lambda < 0.489$. (ii) Obtain a PCW using triangular-lattice PC in ΓK direction by removing a single row of holes (width: W_a). (iii) Obtain again another PCW with the deformed triangular lattice in ΓM direction by removing a single row of holes (width: W_b). Simply removing one row of holes from each type of PC ends up with a different PCW width. Combining them may produce unacceptable back reflection at junctions due to PCW-width mismatch. (iv) Next fix the width of bend region made of the deformed PC by removing one row of holes (to suppress multimode wave propagation) and equate it to the width of the usual PCW such as removing one row of holes and reducing further W_a so that $W_b = W_a = a$ (Fig. 6.5). (v) Choose the propagating frequencies of each PCW separately and the intersection

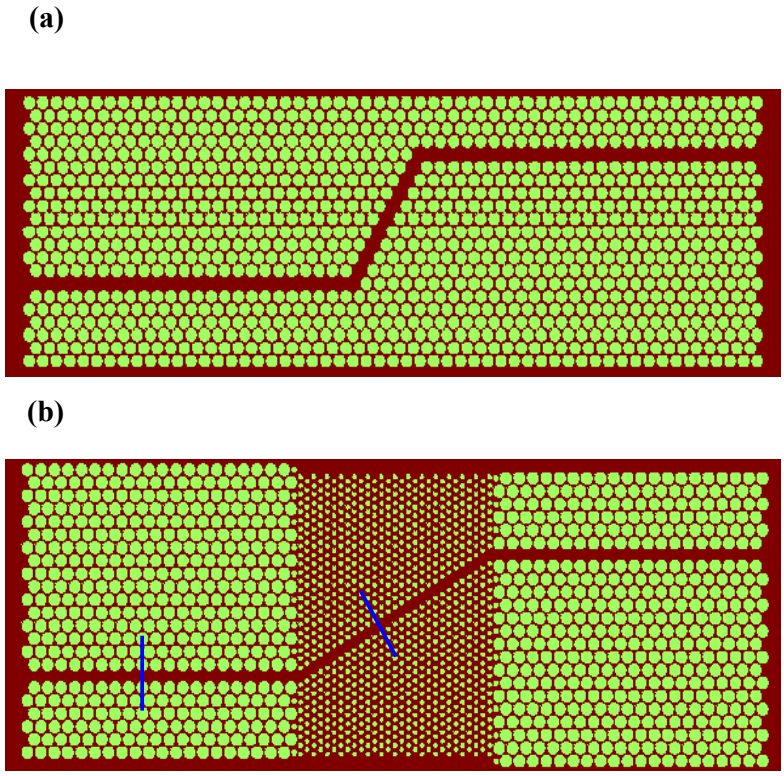

Figure 6.6: Photonic crystal waveguide bends. (a) Configuration of photonic crystal waveguide for 60^0 bend. (b) 30^0 waveguide bend obtained by photonic crystal heterostructure. The two lines transverse to the waveguide axis represent the planes where time-averaged Poynting vector is calculated.

of the frequency ranges corresponding to the propagating modes of the PCW, which is subject to the bend loss. (vi) Select a center frequency corresponding to high transmission for a modulated Gaussian (narrow band) pulse to send through the PCW. More than one pulse with different center frequency must be sent to map the transmission throughout the entire band. (vii) Integrate the time-averaged Poynting vector across the PCWs on both sides of the bend to obtain the power transmission coefficient $\eta(\omega)$. (viii) The steady-state field variations are checked for consistency. The results obtained by applying these steps will be discussed next.

6.4 Results and discussions of the 30^0 PCW bend

Normalization of the modes is carried out carefully to make sure not to include other loss mechanisms, such as in and out coupling associated with the initial excitation of the PCW, end effects, and propagating losses except that specifically resulting from the bend. We have also checked to ensure that there is no loss associated with possible excitation of surface modes between the various PCs comprising the PC heterostructure. The observation points placed as shown in Fig. 6.6 stored time-varying fields (for the input: E_y, H_z and for the output: E_x, E_y and H_z). The Gaussian pulse propagation through the bend is indicated in Fig. 6.7. The field is mainly confined around the center of the waveguide and the input as well as the transmitted and reflected fields can be extracted easily as indicated in Fig. 6.8. We plotted H_z at the center of the detection plane with respect to time in Fig. 6.9 for clarity purposes. Using these data, time-averaged Poynting vectors are calculated to obtain the power transmission and reflection coefficients. As can be seen from Fig. 6.10, high transmission ($\eta > 90\%$) is obtained.

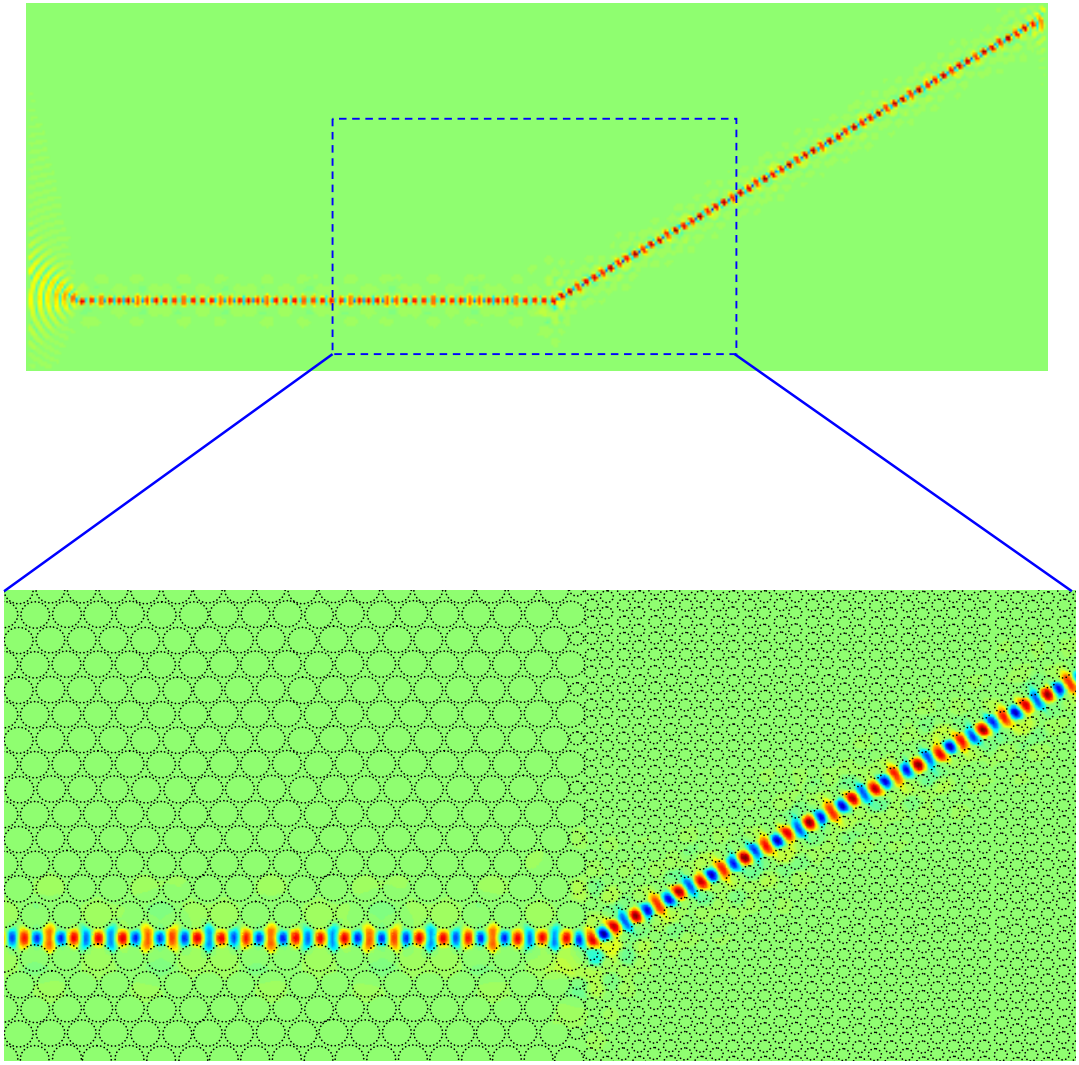

Figure 6.7: PCHS waveguide 30 degree bend field profile Hz, with phase information.

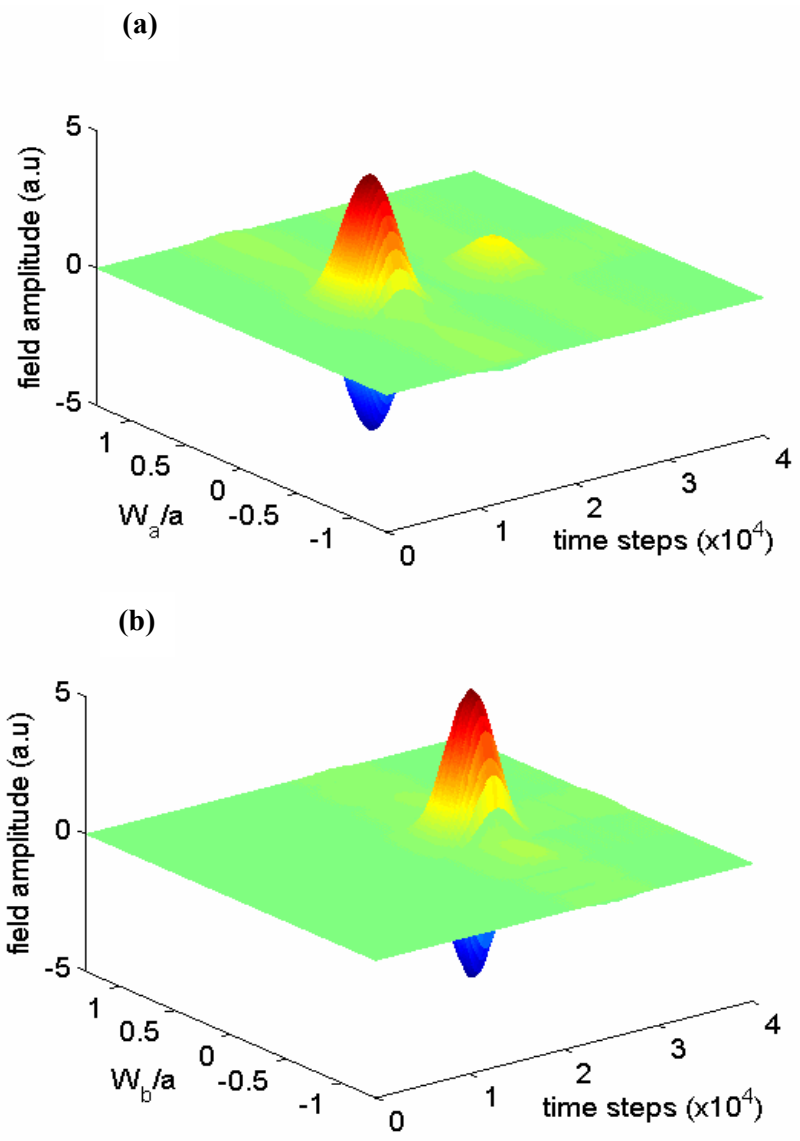

Figure 6.8: The narrow band modulated Gaussian pulse propagation (H_z) in time at the detection points. (a) The observation plane stores the input as well as the reflected pulse. (b) Only the transmitted pulse after the bend is stored.

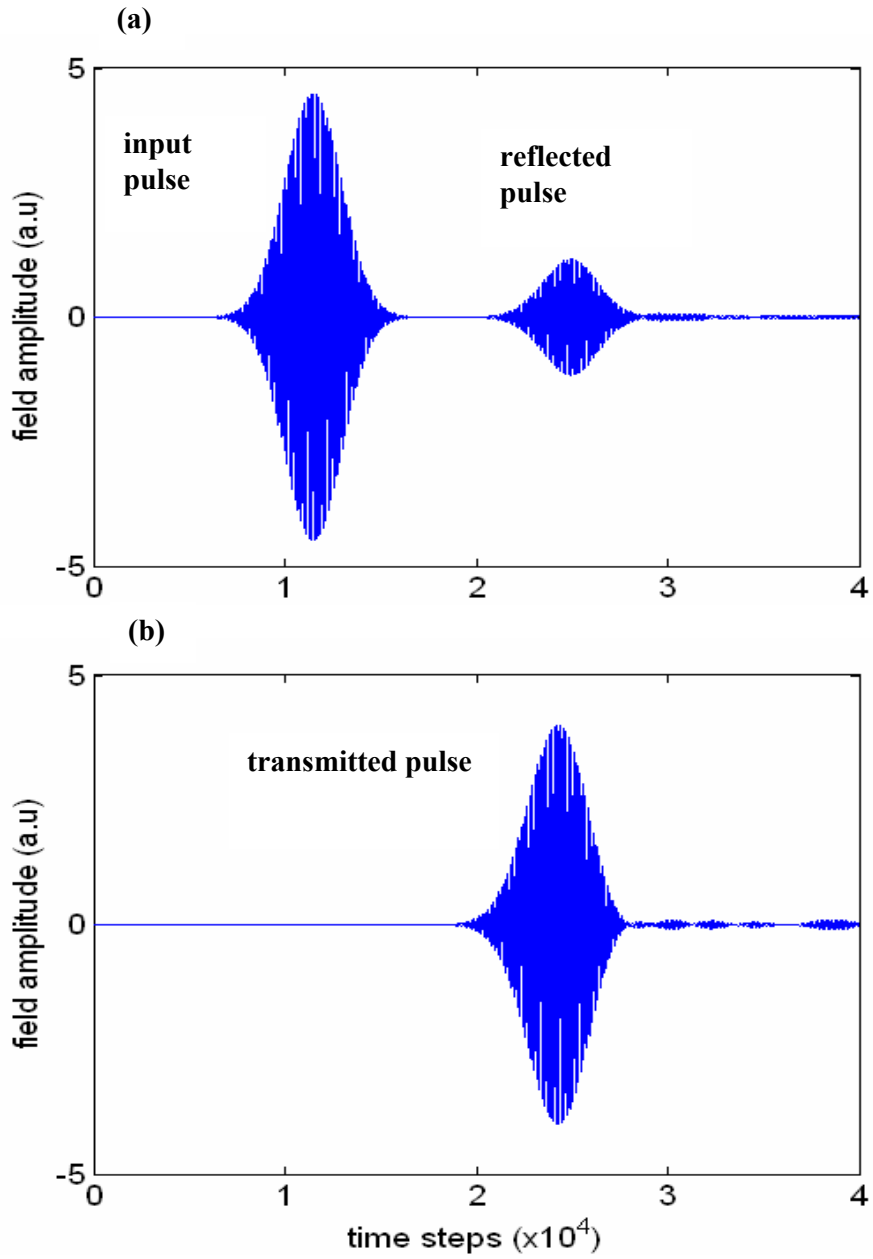

Figure 6.9: Field amplitudes stored in time at the input and output detection points. (a) The input and the reflected pulse is shown. (b) The transmitted pulse is shown.

The power transmission through the bend is peaked ($\eta > 95\%$) around $\omega = 0.414\, a/\lambda$ and if a is taken to be 642 nm, the wavelength is $\lambda = 1.55\,\mu$m. This observation is further corroborated by plotting the steady-state field variations in Fig. 6.11. The center wavelength $\lambda = 1.55\,\mu$m of the narrow-band modulated Gaussian is selected as the wavelength at which there is high transmission. The transmission is uniform and no strong cavity effect is seen around the corners. This is an obvious advantage to have small path-length difference of the PCW with $\theta = 30^0$ for phase-front compensation. Since there is no modification in the PCW corner region, such as inserting hole defects, the proposed approach in principle should be broadband and should not suffer from enhanced out-of plane radiation losses.

It is important to note that the performance of the new structure is not restricted to the case study outlined above. For example, one may select $r_b = 0.15a$ and $r_a = 0.40a$ or some other range of parameters. It may not be necessary to depend solely on PBG guiding in some cases. Due to high index-contrast, the index-guiding mechanism can also be employed. It may be worth looking at the transmission through such PCW bends keeping in mind that the performance of routing the field will definitely be lower than the PBG guiding case. It may appear disadvantageous not to have a large frequency overlap for the two PCW structures. We can, however, increase the overlap of the band gaps by scaling down the lattice constant a of the usual PC, hence shifting the frequencies to higher values. As a result, almost 100 % overlap in the transmission region might become possible. Potential applications of the deformed PC should not be restricted only to PCW bend designs. Other bend angles, such as 90^o and U-type bends, are also possible. In fact, Fig. 6.12 shows a 90^0 bend design. All the parameters are kept the same including the input pulse and only the bend configuration is modified. The high transmission through four bends can be

seen from the figure. Engineering the middle section may help to implement different devices, e.g., Mach-Zehnder interferometers and directional couplers as well.

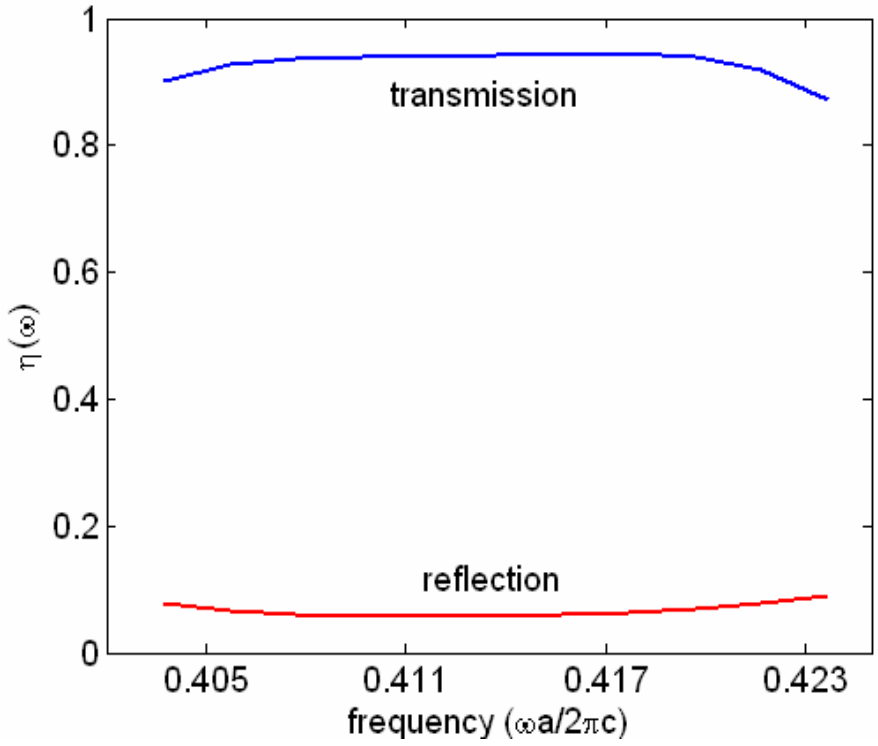

Figure 6.10: The bending efficiency $\eta(\omega)$ of the photonic crystal heterostructure waveguide. The ratio of transmitted power to the input power gives the transmission coefficient and the reflection coefficient is obtained by taking the ratio of the reflected power to the input power.

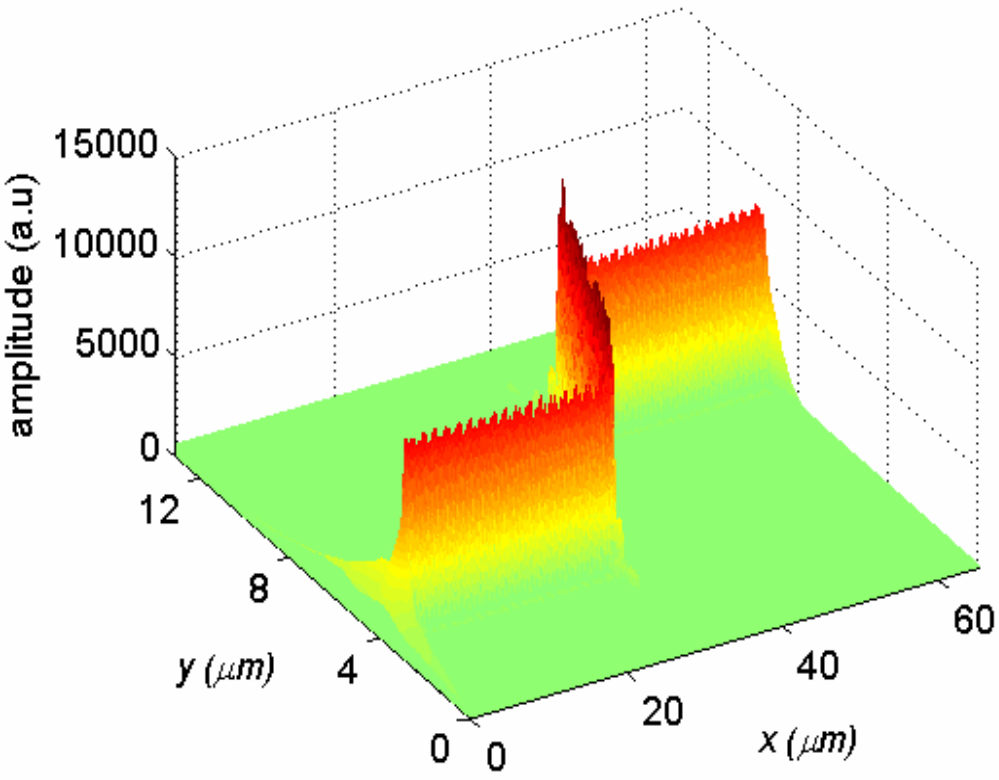

Figure 6.11: Steady-state field variation of 30^0 PCW bend for a modulated Gaussian pulse. The center frequency of the pulse is centered at $\omega = 0.414\, a/\lambda$ where a is the lattice constant and λ is the wavelength of light.

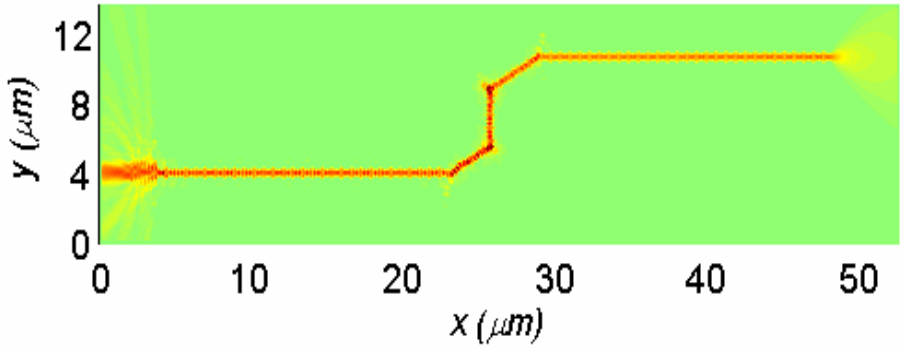

Figure 6.12: Photonic crystal heterostructure for 90^0 bend. The input pulse and the parameters are the same as in Fig. 6.10.

The inclusion of another type of lattice may give rise difficulty in the fabrication as compared to the single type of lattice case. Especially, the interfaces of different PC waveguide section have to be terminated properly not to cause spurious reflections from these parts. On the other hand, the approach is free from implementing cavity-type effects at the bend so that one does not need to engineer single lattice sites in the vicinity of the bend, a procedure that makes the fabrication difficult yet more sensitive to the disorder. Moreover, the second type of lattice is the squeezed and rotated version of the original lattice, triangular lattice of circular air holes. Therefore, similar fabrication procedures can be followed for the whole structure except changing the mask. Features sizes of 114 nm and 64 nm would be required to fabricate such a PC heterostructures operating at telecom wavelengths. Even though such structures can be manufactured with the current fabrication techniques such as electron beam lithography or deep ultraviolet lithography [106, 108], availability of selecting another pairs of pore radii e.g., $r_a = 0.40a$ and $r_b = 0.15a$ may ease the fabrication difficulties.

6.5 Conclusions

In conclusion, we have introduced a deformed triangular-lattice PC obtained by perturbing the lattice in ΓM direction and carried out analysis for PCW bends based on PC heterostructures aiming towards low-loss and high-bandwidth light propagation. The enhancement of power transmission ($\eta > 90\%$) across significant bandwidths, even without optimizing the corners, is achieved with 30^0 PCW bends. Further improvements may be realized by modifying the corner region using some of the techniques cited above. The physical interpretation of bend loss mechanisms was explained. To deploy PC devices for high-bandwidth/high-speed integrated optics,

high bend loss and low-transmission bandwidths are not tolerable. The improvement predicted here is a large step and it may make more flexible design for photonic-integrated circuits.

CHAPTER VII

Conclusions and future research directions

In the final chapter of the thesis, the contributions along with the possible future research directions that may be followed are outlined.

7.1 Conclusions

There are two main categories that this thesis made contributions. The first one is the bio-sensing applications of PC-based devices and the second one is concerning with the improvement of the performance of current PCs and waveguide bends by introducing of two new concepts; annular PC and PC heterostructure waveguides. The key achievements of this research can be summarized as:

- The propagation of terahertz waves in 2D PCWs was studied computationally to investigate the effects of introducing small quantities of molecules, such as deoxyribonucleic acid, into the selected air holes for sensor applications. The finite-difference time-domain method with recursive convolution technique as formulated in Chapter II was used for the numerical analyses. Low group velocity around the photonic band edge and electric-field enhancements in the low-index medium enabled significantly enhanced interaction of guided light with the molecular sample in addition to reducing the required amount of sample considerably. Comparison with bulk systems showed that PCWs are promising for biochemical sensing.

- The improvement of the sensor performance has been achieved with a cavity type of waveguide structure, called coupled-resonator optical-waveguide (CROW). The prospects of this structure are the nature of the moderately supporting high-Q and low group velocity.
- A detailed study of CROW-based sensors for biochemical sensing and of design issues affecting the sensitivity was presented. The terahertz interaction with the analyte was modeled as a Lorentz medium. The sensitivity dependence on the CROW structure parameters, such as intercavity distance and cavity type (donor/acceptor), was investigated for the effects in the terahertz region of the electromagnetic spectrum of introducing small quantities of molecules, such as DNA, in the air holes. The proposed device was predicted to exhibit sensitivity enhancement over bulk systems and PCW structures. The CROW-based device required a small analyte volume of nanoliters ($<10^{-9}$ L) and a refractive index change of $\Delta n = 0.033$ corresponded to a wavelength shift of $\Delta\lambda = 1.17$ μm. Introducing the absorptive material into the low-index medium greatly affected the shape of the propagating modes of the CROW and the transmitted electric field. The shift of the resonant frequency also depended linearly on the refractive index changes for off-resonant case (dispersive effect).
- PC-based sensors hold promises. Both small absolute analyte quantities (nanoliters) and low-concentration samples (picomoles) should be detectible. The uniquenesses of the approach here are as follows. PC provides enhanced interaction between the EM field and the analyte mainly due to the two effects: enhancing the E-field proportional to the Q of the cavity and lowering the group

velocity hence increasing the interaction time. Because the sample is contained within the PC, the sensor can be integrated with light sources and detectors. Moreover, multi-analyte and compact-sensing schemes are feasible with PC structures as one can easily obtain array of multi-channel PC waveguides. Finally, because the field can be confined in the low-index medium (air in this case) within the PC, there is direct field-sample interaction rather than evanescent-wave sensing as some of the common sensing methods such as fiber-optic and slab waveguides that employ such means. In general, the sensitivity of the evanescent-field sensor is very low because exponentially decaying EM field penetrating to the sensing region is low.

- The initial stages of experiment performed in the group of our collaborator Prof. Martin Koch of the Technical University of Braunschweig included the investigation of transmission spectrum of different liquids loaded to PCW. The implementation of the approach provided an opportunity to test the initial theoretical work carried out and feedback obtained from this work will be valuable for further research directions as outlined below.
- Engineering the PCs for the PBG enhancement has resulted in a novel type of PC called annular PC composed of a dielectric-rod and a circular-air-hole array in a square or triangular lattice such that a dielectric rod is centered within each air hole is studied. The dielectric rods within the air holes greatly modified the dispersion diagram of the photonic crystal despite the fact that the percentage of volume occupied by the dielectric rods may be small (<12%). Increasing the radius of the inner-dielectric rod, starting from zero to a critical value, reduced the

band gap and closed it completely as expected, because of the addition of more dielectric material inside the unit cell. Continuing to increase the radius of the rod above the critical value surprisingly created another photonic band gap. Comparison of the dispersion diagrams of the new structure and the original lattice (circular air hole square/triangular array in dielectric background) revealed that the photonic band gap is considerably enhanced in size for both square and triangular lattice with the new structure. This approach preserved the symmetry of the structure and provided a complete photonic band gap away from the close-packed condition and at low normalized frequencies.

- The typically low and/or narrow band transmission efficiency of PCW bends has been improved incorporating the idea of perturbing the unit cell lattice in some special directions, e.g., ΓM; hence, obtaining PC hetero-structures. The high transmission for a bending angle of 30^0 is achieved with triangular lattice PC. We showed how PCW bends occurring at heterojunctions between different PCs may enable unprecedented flexibility in meeting these aims.

7.2 Future Research Directions

The aforementioned completed works bring new horizons (visions) for the future research directions.

The preliminary explorations have only covered a small area of parameter space. One may study PCWs obtained from double rows of holes to enhance the overlap of the guided field with the analyte. As for CROW waveguides, there are many further degrees of freedom that may enable stronger interaction between the guided EM field and the

analyte. It has been found that by slightly displacing the holes immediately proximate to a PC cavity, strong enhancement of the Q can be obtained [29]. For the CROW-based sensors, this should translate into stronger EM-analyte interaction, and thus improved sensitivity. Alternative PCW configurations may be attractive, aiming to obtain superior enhancement over the ones studied. Therefore, one part of the future work will be to carry out a similar analysis for different configurations while given the emphasis to the role of the waveguide parameters, such as width (W), length (L), and the positions and the number of holes in waveguide section, on the sensor performance. The aim of studying all these parameters should be to search for the configurations that possess longer field-matter interaction, enabling smaller amounts of analyte. For example, assuming two PCWs having same υ_g, the one with fewer holes should be preferable.

The main reason to implement PCW sensors are their simplicity. The same waveguide section can be used for propagation and sensing purposes. More advanced structures to increase the sensitivity further, such as Mach-Zehnder interferometers, could be studied. Such devices will employ sensing criteria other than attenuation, e.g., phase sensing.

The beauty of the APC compared to the usual lattice PC is that one may interpret APC as having an air defect in each unit cell or two interfaces for the scattering. Both interpretations will pave the way for novel device implementations. Regarding the out-of plane scattering losses, APCs are expected to perform better than simple rod or air-hole arrays since the inner dielectric rods in the center of the each air hole reduce the distance that the light travels within air; this will suppress the out-of-plane losses as these losses increase with increasing air fraction. Since the unit cell of annular PC contains two

interfaces for scattering of light so it is expected to function superior in applications requiring dispersive elements such as super-prisms as well.

The idea of deforming unit lattice crystal in some special directions may arise all the new device implementations of PCs such as couplers, interferometers, and add-drop filters by breaking the angle constraints of PC lattice while improving the transmission efficiency through the bends significantly. The performance of the previously proposed structures may be improved with the incorporation of the heterostructure PC together with the conventional PC.

REFERENCES

[1] E. Yablonovitch, "Inhibited spontaneous emission in solid-state physics and electronics," *Phys. Rev. Lett.,* vol. 58, pp. 2059-2062, May 1987.

[2] S. John, "Strong localization of photons in certain disordered dielectric superlattices," *Phys. Rev. Lett.,* vol. 58, pp. 2486-2489, June 1987.

[3] J. D. Joannopoulos, R. D. Meade, and J. N. Winn, *Photonic Crystals, Molding the Flow of Light,* Princeton, New Jersey: Princeton University Press, 1995.

[4] C. Kittel, *Introduction to Solid State Physics,* John Wiley & Sons, Inc. 1996.

[5] A. Yariv, and P. Yeh, *Optical Waves in Crystals,* John Wiley & Sons, Inc. 1984.

[6] E. Yablonovitch, T. J. Gmitter, R. D. Meade, A. M. Rappe, K. D. Brommer, and J. D. Joannopoulos, "Donor and acceptor modes in photonic band structure," *Phys. Rev. Lett*., vol. 67, pp. 3380–3383, Dec. 1991.

[7] E. Yablonovitch and T. J. Gmitter, "Photonic band structure: The face-centered-cubic case," *Phys. Rev. Lett*., vol. 63, pp. 1950–1953, Oct. 1989.

[8] E. Özbay, A. Abeyta, G. Tuttle, M. Tringides, R. Biswas, C. T. Chan, C. M. Soukoulis, and K. M. Ho, "Measurement of a three-dimensional photonic band gap in a crystal structure made of dielectric rods," *Phys. Rev. B,* vol. 50, pp. 1945–1948, July 1994.

[9] K. Busch and S. John, "Photonic band gap formation in certain self-organizing syetems," *Phys. Rev. E,* vol. 58, pp. 3896-3908, Sept. 1998.

[10] M. Plihal and A. A. Maradudin, "Photonic band structure of two-dimensional systems: The triangular lattice," *Phys. Rev. B,* vol. 44, pp. 8565-8571, Oct. 1991.

[11] K. M. Ho, C. T. Chan, and C. M. Soukoulis, "Existence of a photonic gap in periodic dielectric structures," *Phys. Rev. Lett.,* vol. 65, pp. 3152-3155, Dec. 1990.

[12] J. B. Pendry and A. MacKinnon , "Calculation of photon dispersion relations," *Phys. Rev. Lett*., vol. 69, pp. 2772–2775, Nov. 1992.

[13] A. Taflove, *Computational Electrodynamics - The Finite-Difference Time-Domain Method,* Norwood, Massachusetts: Artech House, 2000.

[14] K. S. Kunz, *The Finite Difference Time Domain Method for Electromagnetics*, Boca Raton: CRC Press, 1993.

[15] N. Stefanou, V. Karathanos, and A. Modinos, "Scattering of electromagnetic-waves by periodic structures," *J. Phys.-Condes. Matter,* vol. 4, pp. 7389-7400, Sept. 1992.

[16] X. D. Wang, X. G. Zhang, Q. L. Yu, and B. N. Harmon, "Multiple-scattering theory for electromagnetic waves," Phys. Rev. B vol. 47, pp. 4161-4167, Feb. 1993.

[17] E. Lidorikis, M. M. Sigalas, E. N. Economou, and C. M. Soukoulis, "Tight-Binding Parametrization for Photonic Band Gap Materials*," Phys. Rev. Lett.* vol. 81, pp. 1405–1408, Aug. 1998.

[18] G. P. Nordin, S. Kim, J. Cai, and J. Jiang, "Hybrid integration of conventional waveguide and photonic crystal structures," *Opt. Exp.*, vol. 10, pp. 1334-1341, Nov. 2002.

[19] H. Kosaka, T. Kawashima, A. Tomita, M. Notomi, T. Tamamura, T. Sato, and S. Kawakami, "Superprism phenomena in photonic crystals," *Phys. Rev. B,* vol. 58, pp. R10096–R10099, Oct. 1998.

[20] H. Y. Ryu, M. Notomi, and Y. H. Lee, "Finite-difference time-domain investigation of band-edge resonant modes in finite-size two-dimensional photonic crystal slab," *Phys. Rev. B*, vol. 68, pp. 045209 (8 pages), July 2003.

[21] S. Noda, M. Yokoyama, M. Imada, A. Chutinan, and M. Mochizuki, "Polarization mode control of two-dimensional photonic crystal laser by unit cell structure design," *Science*, vol. 293, pp. 1123-1125, Aug. 2001.

[22] P.R. Villeneuve, S. Fan, and J. D. Joannopoulos, "Microcavities in photonic crystals: Mode symmetry, tunability, and coupling efficiency," *Phys. Rev. B*, vol. 54, pp. 7837-7842, Sept, 1996.

[23] P. Rigby and T. F. Krauss, "The Vs and Qs of optical microcavities," *Nature,* vol. 390, p. 125, Nov. 1997.

[24] O. Painter, J. Vučković, and A. Scherer, "Defect modes of a two-dimensional photonic crystal in an optically thin dielectric slab," *J. Opt. Soc. Am. B,* vol. 16, pp. 275-285, Feb. 1999.

[25] O. Painter, R. K. Lee, A. Scherer, A. Yariv, J. D. O'Brien, P. D. Dapkus, and I. Kim, "Two-Dimensional photonic band-gap defect mode laser," *Science,* vol. 284, pp. 1819-1821, June 1999.

[26] T. Yoshie, J. Vuckovic, A, Scherer, H. Chen, and D. Deppe, "High quality two-dimensional photonic crystal slab cavities," *Appl. Phys. Lett.* vol. 79, pp. 4289-4291, Dec. 2001.

[27] Y. Akahane, T. Asano, B. S. Song, and S. Noda, "High-Q photonic nanocavity in a two-dimensional photonic crystal," *Nature*, vol. 425, pp. 944-947, Oct. 2003.

[28] K. Srinivasan, P. E. Barclay, and O. Painter, "Fabrication-tolerant high quality factor photonic crystal microcavities," *Opt. Express*, vol. 12, pp. 1458-1463, April 2004.

[29] B. S. Song, S. Noda, T. Asano, and Y. Akahane, "Ultra-high-Q photonic double-heterostructure nanocavity," *Nature Materials*, vol. 4, pp. 207-210, Feb. 2005.

[30] T. F. Krauss, B. Vogele, C. R. Stanley, R. M. De La Rue, R.M, "Waveguide microcavity based on photonic microstructures," *IEEE Photon. Technol. Lett.,* vol. 9, pp. 176-178, Feb. 1997.

[31] J. S. Foresi, P. R. Villeneuve, J. Ferrera, E. R. Thoen, G. Steinmeyer, S. Fan, J. D. Joannopoulos, L.C. Kimerling, H. I. Smith, E. P. Ippen, "Photonic-bandgap microcavities in optical waveguides," *Nature*, vol. 390, pp. 143-145, Nov. 1997.

[32] M. Notomi, H. Suzuki, and T. Tamamura, "Directional lasing oscillation of two-dimensional organic photonic crystal lasers at several photonic band gaps," *Appl. Phys. Lett.,* vol. 78, pp. 1325-1327, March 2001.

[33] S. G. Johnson, P. R. Villeneuve, S. Fan, and J. D. Joannopoulos, "Linear waveguides in photonic-crystal slabs," *Phys. Rev. B,* vol. 62, pp. 8212–8222, Sept. 2000.

[34] M. Lončar, T. Doll, J. Vučković, and A. Scherer, "Design and fabrication of silicon photonic crystal optical waveguides," *J. Lightwave Tech.*, vol. 18, pp. 1402-1411, Oct. 2000.

[35] M. Lončar, J. Vučković, and A. Scherer, "Methods for controlling positions of guided modes of photonic-crystal waveguides," *J. Opt. Soc. Am. B*, vol. 18, pp. 1362-1368, March 2001.

[36] S. G. Johnson, S. Fan, P. R. Villeneuve, J. D. Joannopoulos, and L. A. Kolodziejski, "Guided modes in photonic crystal slabs," *Phys. Rev. B*, vol. 60, pp. 5751–5758, Aug. 1999.

[37] A. Adibi, Y. Xu, R. K. Lee, A. Yariv, and A. Scherer, "Properties of the slab modes in photonic crystal optical waveguides," *J. Lightwave Tech.*, vol. 18, pp. 1554-1564, Nov. 2000.

[38] A. Scherer, O. Painter, J. Vučković, M. Loncar, and T. Yoshie, "Photonic crystals for confining, guiding, and emitting light," *IEEE Trans. Nanotechnology*, vol. 1, pp. 4-11, March 2002.

[39] A. Mekis, J. C. Chen, I. Kurland, S. Fan, P. R. Villeneuve, and J. D. Joannopoulos, "High transmission through sharp bends in photonic crystal waveguides," *Phys. Rev. Lett.,* vol. 77, pp. 3787–3790, Oct. 1996.

[40] A. Chutinan, M. Okano, and S. Noda, "Wider bandwidth with high transmission through waveguide bends in two-dimensional photonic crystal slabs," *Appl. Phys. Lett*., vol. 80, pp. 1698-1700, March 2002.

[41] M. Notomi, K. Yamada, A. Shinya, J. Takahashi, C. Takahashi, and I. Yokohama, "Extremely large group-velocity dispersion of line-defect waveguides in photonic crystal slabs," *Phys. Rev. Lett.,* vol. 87, pp. art. no. 253902, Dec. 2001.

[42] V. Berger, "Nonlinear photonic crystals," *Phys. Rev. Lett.,* vol. 81, pp. 4136–4139, Nov. 1998.

[43] L. –H. Peng, C. –C. Hsu, and Y. –C. Shih, "Second-harmonic green generation from two-dimensional χ^2 nonlinear photonic crystal with orthorhombic lattice structure," *Appl. Phys. Lett*., vol. 83, pp. 3447-3449, Oct. 2003.

[44] F. Cuesta-Soto, A. Martínez, J. García, F. Ramos, P. Sanchis, J. Blasco, and J. Martí, "All-optical switching structure based on a photonic crystal directional coupler," *Opt. Exp.,* vol. 12, pp. 161-167, Jan. 2004.

[45] M. F. Yanik, S. Fan, and M. Soljačić, "High-contrast all-optical bistable switching in photonic crystal microcavities," *Appl. Phys. Lett*., vol. 83, pp. 2739-2741, Oct. 2003.

[46] R. Gonzalo, P. De Maagt, and M**.** Sorolla, **"**Enhanced patch-antenna performance by suppressing surface waves using photonic-bandgap substrates," *IEEE Trans. Microwave Theory Tech*., vol. 47, pp. 2131-2138, Nov. 1999.

[47] E. R. Brown, C. D. Parker, and E. Yablonovitch, "Radiation properties of a planar antenna on a photonic-crystal substrate," *J. Opt. Soc. Am. B*, vol. 10, pp. 404-407, Feb. 1993.

[48] Y. Fei-Ran, M. Kuang-Ping, Q. Yongxi, and T. Itoh, "A uniplanar compact photonic-bandgap (UC-PBG) structure and its applications for microwave circuit," *IEEE Trans. Microwave Theory Tech*., vol. 47, pp. 1509-1514, Aug. 1999.

[49] B A. Munk, *Frequency Selective Surfaces: Theory and Design,* New York: Wiley, 2000.

[50] M. Loncar, A. Scherer, and Y. Qiu, "Photonic crystal laser sources for chemical detection," *Appl. Phys. Lett.,* vol. 82, pp. 4648-4650, June 2003.

[51] E. Chow, A. Grot, L. W. Mirkarimi, M. Sigalas, and G. Girolami, "Ultracompact biochemical sensor built with two-dimensional photonic crystal microcavity," *Opt. Lett.*, vol. 29, pp. 1093-1095, May 2004.

[52] J. Topol'ancik, P. Bhattacharya, J. Sabarinathan, and P. –C. Yu, "Fluid detection with photonic crystal-based multichannel waveguides," *Appl. Phys. Lett.,* vol. 82, pp. 1143-1145, Feb. 2003.

[53] D. M. Pustai, A. Sharkawy, S. Shi, and D. W. Prather, "Tunable photonic crystal microcavities," *Appl. Opt*., vol. 41, pp. 5574-5579, Sept. 2002.

[54] P. Halevi and F. Ramos-Mendieta, "Tunable photonic crystals with semiconducting constituents," *Phys. Rev. Lett.,* vol. 85, pp. 1875–1878, Aug. 2000.

[55] S. S. M. Cheng, Lie-Ming Li, C. T. Chan, and Z. Q. Zhang, "Defect and transmission properties of two-dimensional quasiperiodic photonic band-gap systems," *Phys. Rev. B,* vol. 59, pp. 4091–4099, Feb.1999.

[56] M. A. Kaliteevski, J. Manzanares, D. Cassagne, J. P. Albert, S. Brand, and R. A. Abram, "Appearance of photonic minibands in disordered photonic crystals," *J. Pys.: Condens. Matter*, vol. 15, pp 785-790, Feb. 2003.

[57] K-C. Kwan, X. Zhang, Z-Q. Zhang, and C. T. Chan, "Effects due to disorder on photonic crystal-based waveguides," *Appl. Phys. Lett*., vol 82, pp. 4414-4416, June 2003.

[58] S. Fan, P. R. Vileneuve, and J. D. Joannopoulos, "Theoretical investigation of fabrication-related disorder on the properties of photonic crystals," *J. Appl. Phys*., vol. 78, pp. 1415-1418, Aug. 1995.

[59] S. Boscolo, C. Conti, M. Midrio, and C. G. Someda, "Numerical analysis of propagation and impedance matching in 2D photonic crystal waveguides with finite length," *J. Lightwave Tech.*, vol. 20, pp. 304–310, Feb 2002.

[60] G. Tayeb, B. Gralak, and S. Enoch, "Structural colors in nature and butterfly-wing modeling," *Opt. Photon. News*, vol. 14, pp. 38-43, Feb. 2003.

[61] P. Vukusic and J. R. Sambles, "Photonic structures in biology," *Nature,* vol. 424, pp. 852-855, Aug 2003.

[62] K. S. Yee, "Numerical solution of initial boundary value problems involving Maxwell's equations in isotropic media," *IEEE Trans. Antennas and Propagation,* vol. 14, pp. 302-307, Jan. 1966.

[63] J. P. Berenger, "A perfectly matched layer for the absorption of electromagnetic waves," *J. Comput. Phys.,* vol. 114, pp. 185-200, July 1994.

[64] C. Sirtori, "Bridge for the terahertz gap," *Nature,* vol. 417, pp. 132-133, May 2002.

[65] P. H. Bolivar, M. Brucherseifer, M. Nagel, H. Kurz, A. Bosserhoff, and R. Büttner, "Label-free probing of genes by time-domain terahertz sensing," *Phys. Med. Biol.,* vol. 47, pp. 3815-3821, Oct. 2002.

[66] B. M. Fischer, M. Walther, and P. Uhd Jepsen, "Far-infrared vibrational modes of DNA components studied by terahertz time-domain spectroscopy," *Phys. Med. Biol.,* vol. 47, pp. 3807-3814, Oct. 2002.

[67] M. Nagel, P. H. Bolivar, M. Bruscherseifer, H. Kurz, A. Bosserhoff, and R. Büttner, "Integrated planar terahertz resonators for femtomolar sensitivity label-free detection of DNA hybridization," *Appl. Opt.,* vol. 41, pp. 2074-2078, April 2002.

[68] A. Wittlin, L. Genzel, F. Kremer, S. Häseler, A. Poglitsch, and A. Rupprecht, "Far-infrared spectroscopy on oriented films of dry and hydrated DNA," *Phys. Rev. A*, vol. 34, pp. 493-500, July 1986.

[69] M. Nagel, P. H. Bolivar, M. Bruscherseifer, H. Kurz, A. Bosserhoff, and R. Büttner, "Integrated THz technology for label-free genetic diagnostics," *Appl. Phys. Lett*., vol. 80, pp. 154-156, Jan. 2002.

[70] J. B. Jensen, L H. Pedersen, P. E. Hoiby, L. B. Nielsen, T.P. Hansen, J. R. Folkenberg, J. Riishede, D. Noordegraaf, K. Nielsen, A. Carlse, and A. Bjarklev, "Photonic crystal fiber based evanescent-wave sensor for detection of biomolecules in aqueous solutions," *Opt. Lett*., vol. 29, pp. 1974-1976, Sep. 2004.

[71] Y. L. Hoo, W. Jin, C. Shi, H. L. Dong, N. Wang, and S. C. Ruan, "Design and modeling of a photonic crystal fiber gas sensor*," Appl. Opt.,* vol. 42, pp. 3509-3515, June 2003.

[72] D. Yin, Holger Schmidt, J. P. Barber, and A. R. Hawkins, "Integrated ARROW waveguides with hollow cores," *Opt. Exp.,* vol. 12, pp. 2710-2715, June 2004.

[73] H. Kurt and D. S. Citrin, "Photonic crystals for biochemical sensing in the terahertz region," *Appl. Phys. Lett.,* vol. 87, pp. 41108 (3 pages), July 2005.

[74] A. Yariv, Y. Xu, R. K. Lee, and A. Scherer, "Coupled-resonator optical waveguide: a proposal and analysis," *Opt. Lett.,* vol. 24, pp. 711-713, June 1999.

[75] M. Bayindir, B. Temelkuran, and E. Ozbay, "Tight-binding description of the coupled defect modes in three-dimensional photonic crystals," *Phys. Rev. Lett.,* vol. 84, pp. 2140-2143, March 2000.

[76] Z. L. Zhang, C. Crozaiter, M. Le Berre, and Y. Chen, "In situ bio-functionalization and cell adhesion in microfluidic devices," *Microelectronic Eng*., vol. 78-79, pp. 556-562, March 2005.

[77] Y. Xu, R. K. Lee, and A. Yariv, "Propagation and second-harmonic generation of electromagnetic waves in a coupled-resonator optical waveguide," *J. Opt. Soc. Am. B*, vol. 17, pp. 387-400, March 2000.

[78] C. M. Soukoulis (Ed.) *Photonic Crystals and Light Localization in the 21st Century* (Kluwer Academic Publishers, The Netherlands, 2001).

[79] S. John and M. Florescu, "Photonic bandgap materials: towards an all-optical micro-transistor," *J. Opt. A: Pure Appl. Opt*., vol. 3, pp. S103-S120, Sep. 2001.

[80] H. Y. D. Yang, N. G. Alexopoulos, and E. Yablonovitch, "Photonic band-gap materials for high-gain printed circuit antennas," *IEEE Trans. Antennas Propag*., vol. 45, pp. 185-187, Jan. 1997.

[81] R. Coccioli, W. R. Deal, and T. Itoh, "Radiation characteristics of a patch antenna on a thin PBGsubstrate," *IEEE Antennas and Propag. Society International Symposium*, vol. 2, pp. 656-659, June 1998.

[82] Z-Y. Li, B-Y Gu, and G-Z Yang, "Large Absolute Band Gap in 2D Anisotropic Photonic Crystals," *Phys. Rev. Lett*. vol. 81, pp. 2574-2577, Sep. 1998.

[83] C. M. Anderson and K. P. Giapis, "Larger Two-Dimensional Photonic Band Gaps," *Phys. Rev. Lett*., vol. 77, pp. 2949-2952, May 1996.

[84] X. Zhang and Z-Q Zhang, "Creating a gap without symmetry breaking in two-dimensional photonic crystals," *Phys. Rev. B*, vol. 61, pp. 9847-9850, April 2000.

[85] N. Susa, "Large absolute and polarization-independent photonic band gaps for various lattice structures and rod shapes," *J. Appl. Phys. Lett*., vol. 91, pp. 3501-3510, March 2002.

[86] M. Agio and L. C. Andreani, "Complete photonic band gap in a two-dimensional chessboard lattice," *Phys. Rev. B*, vol. 61, pp. 15519-15522, June 2000.

[87] S. Takayama, H. Kitagawa, Y. Tanaka, T. Asano, and S. Noda, "Experimental demonstration of complete photonic band gap in two-dimensional photonic crystal slabs," *Appl. Phys. Lett*., vol. 87, pp. 061107 (3 pages), Aug. 2005.

[88] S. Guo and S. Albin, "Simple plane wave implementation for photonic crystal calculations," *Opt. Express*, vol. 11, pp. 167-175, Jan. 2003.

[89] R. Zoli, M. Gnan, D. Castaldini, G. Bellanca, P. Bassi, "Reformulation of the plane wave method to model photonic crystals," *Opt. Express*, vol. 11, pp. 2905-2910, Nov. 2003.

[90] R. Wang, X-H. Wang, B-Y. Gu, and G-Z. Yang, "Effects of shapes and orientations of scatterers and lattice symmetries on the photonic band gap in two-dimensional photonic crystals," *J. Appl. Phys.*, Vol. 90, pp. 4307-4313, Nov. 2001.

[91] H. Benistry, D. Labilloy, C. Weisbuch, C. J. M. Smith, T. F. Krauss, D. Cassagne, A. Beraud, and C. Jouanin, "Radiation losses of waveguide-based two-dimensional photonic crystals: Positive role of the substrate," *Appl. Phys. Lett*., vol. 76, pp. 532-536, Jan. 2000.

[92] W. Bogaerts, P. Bienstman, D. Taillaert, R. Baets, and D. D. Zutter, "Out-of-plane scattering in Photonic Crystal Slabs," *IEEE Photon. Technol. Lett.*, vol. 13, pp. 565-567, June 2001.

[93] J. D. Joannoupoulos, P. R. Villeneuve, and S. Fan, "Photonic crystals: putting a new twist on light," *Nature*, vol. 386, pp. 143-149, March 1997.

[94] H. Kosaka, T. Kawashima, A. Tomita, M. Notomi, T. Tamamura, T. Sato, and S. Kawakami, " Self-collimating phenomena in photonic crystals," *Appl. Phys. Lett*. Vol. 74, pp. 1212-1214, March 1999.

[95] E. Chow, S. Y. Lin, J. R. Wendt, S. G. Johnson, and J. D. Joannoupoulos, "Quantitative analysis of bending efficiency in photonic-crystal waveguide bends at $\lambda = 1.55\,\mu$m wavelengths," *Opt. Lett*., vol. 26, pp. 286-288, March 2001.

[96] L. H. Fransen, A. Harpøth, P. Borel, M. Kristensen, J. Jensen, and O. Sigmund, "Broadband photonic crystal waveguide 60^0 bend obtained utilizing topology optimization," *Opt. Express*, vol. 12, pp. 5916-5921, April 2004.

[97] S. Oliver, H. Benisty, M. Rattier, C. Weisbuch, M. Qiu, A. Karlsson, C. J. M. Smith, R. Houdré, and U. Oesterle, "Resonant and nonresonant transmission through waveguide bends in a planar photonic crystal," *Appl. Phys. Lett*., vol. 79, pp. 2514-2516, Oct. 2001.

[98] I. Ntakis, P. Pottier, and R. M. De La Rue, "Optimization of two-dimensional photonic crystal channel waveguide bends through local lattice deformation," *J. Appl. Phys*., vol. 96, pp. 12-18, July 2004.

[99] A. Sharkawy, D. Pustai, S. Shi, and D. W. Prather, "High transmission through waveguide bends by use of polycrystalline photonic-crystal structures," *Opt. Lett*., vol. 28, pp. 1197-1199, July 2003.

[100] B. S. Song, S. Noda, and T. Asano, "Photonic devices based on in-plane hetero photonic crystals," *Science*, vol. 300, pp. 1537, June 2003.

[101] M. V. Kotlyar, L. O'Faolain, R. Wilson, and T. F. Krauss, "High-aspect-ratio chemically assisted ion beam etching for photonic crystals using a high beam voltage-current ratio," *J. Vac. Sci. Technol. B*, vol. 22, pp. 1788-1791, July 2004.